KJERSTI KLEVELAND

PREPARATION, MICROSTRUCTURE, AND MECHANICAL PROPERTIES OF $LaCoO_3$ AND $SrFeO_3$ BASED CERAMICS

INSTITUTT FOR KJEMI

NORGES TEKNISK-
NATURVITENSKAPELIGE UNIVERSITET
NTNU

AVHANDLING NR. 96 - NOVEMBER 2000

This thesis have been submitted to

Institutt for Kjemi

Norges Teknisk-Naturvitenskapelige Universitet

in partial fulfilment of the requirements for

the Norwegian academic degree

DOKTOR INGENIØR

October 2000

PREFACE

First of all, I want to thank my supervisor, professor Tor Grande, for excellent guidance and encouragement during my work. I especially appreciated his never-ending enthusiasm. It was a great motivation! Next, I want to thank my co-supervisor Mari-Ann Einarsrud for guidance, discussions, and for always being interested and positive.

I want to thank Kjell Wiik for collaboration, and the rest of the group when I started, Lisbeth Rørmark, Sonia Faaland, and Lise Sagdahl, for encouragement, discussions and valuable coffee breaks. All the nice people in "Blokk II" have made work very pleasant.

I also want to thank Kristin Breder for collaboration, and for inviting me to do the creep tests at Oak Ridge National Laboratory (ORNL). I am thankful to Andrew Werezczak for his help and guidance during my stay at ORNL. I also wish to thank the staff there, especially Laura Riester, for being so nice to me.

The collaboration with Nina Orlovskaya and Anne Marie Mardal Moe on mechanical properties is appreciated. I also want to thank John Walmsley and Asgeir Bardal for doing the TEM work.

This work has been part of a national collaboration project between Norsk Hydro, Statoil, The University of Oslo, and NTNU. The project meetings have been very inspiring and also gave valuable experience in oral presentation of my work. Financial support from The Research Council of Norway, Statoil and Norsk Hydro is appreciated.

At last, I wish to thank my family for encouragement, and all my friends in Trondheim for making these years fun.

TABLE OF CONTENTS

1 SUMMARY 9
1.1 Densification behavior (Paper I and II). 9
1.2 Mechanical properties (Paper III and IV) 11
1.3 Slip casting (Paper V) 12

2 INTRODUCTION 13
2.1 Background 13
2.2 Aim of the work 16
2.3 The perovskite structure 18
2.4 Functional properties of perovskites 22
2.5 Sintering of perovskites 27
2.6 Mechanical properties 33
2.7 Phase relations 37

3 REFERENCES 42

PAPERS

I. Sintering of $LaCoO_3$ based ceramics.
II. Sintering behavior, microstructure and phase composition of $Sr(Fe,Co)O_{3-\delta}$ ceramics.
III. Compressive creep performance of $SrFeO_{3-\delta}$.
IV. Non-elastic behavior of $LaCoO_3$ based ceramics.
V. Non-aqueous slip casting of $LaCoO_3$.

APPENDICES

I. Mechanical properties of $LaCoO_3$ based ceramics
II. Microstructure and the influence of spontaneous strain in $LaCoO_3$, $La_{0.8}Sr_{0.2}CoO_3$, and $La_{0.8}Ca_{0.2}CoO_3$

1 SUMMARY

Perovskite ceramics based on the first row transition metal oxides have recently received considerable attention due to the combination of high oxygen ionic conductivity and electronic conductivity. These materials have a potential application as dense oxygen permeable membranes for partial oxidation of natural gas or for separation of oxygen from air. The membrane must be gas tight in order to separate gases with high selectivity, and dense ceramics without open porosity are therefore required. The microstructure of the dense ceramics is detrimental for the mechanical properties and is also expected to influence the functional properties. The aim of the present work was to synthesize ceramic powders and prepare dense ceramics based on $LaCoO_{3-\delta}$ and $SrFeO_{3-\delta}$. Furthermore, mechanical characterization of $LaCoO_{3-\delta}$ materials and the creep performance of $SrFeO_{3-\delta}$ were explored.

1.1 Densification behavior (Paper I and II).

The sintering properties of $La_{1-x}M_xCoO_{3-\delta}$ (M=Ca, Sr; x=0, 0.2) and $SrFe_{1-x}Co_xO_{3-\delta}$ (x=0, 0.33) have been investigated by means of dilatometry and isothermal heat treatment, and microstructure and phase composition have been characterized by SEM and X-ray diffraction. Substitution of Ca or Sr in $LaCoO_{3-\delta}$ and Co in $SrFeO_{3-\delta}$ increased the sintering rate. Dense materials with small grain size were obtained in a narrow temperature interval in both material systems. Formation of secondary phases due to variations in the A/B-ratio proved to have a strong effect on the microstructure and sinterability of these materials.

For the $LaCoO_{3-\delta}$ system, dense materials with grain size in the order of 3-5 μm were obtained at 1200°C for near stoichiometric compositions. Considerable grain growth was observed at higher sintering temperatures. The presence of secondary crystalline phases due cation non-stoichiometry acts as grain growth inhibitors by grain boundary pinning. The volume fraction of secondary phases is particularly large in the case of Co-deficient $LaCoO_{3-\delta}$ due to the formation of $La_4Co_3O_{10}$. In non-stoichiometric $La_{0.8}Ca_{0.2}CoO_{3-\delta}$, a liquid phase consisting mainly of CaO and CoO was

observed at 1400°C causing exaggerated grain growth. Considerable pore coarsening was observed in Co-excess $La_{0.8}Ca_{0.2}CoO_{3-\delta}$ at 1350°C.

For $SrFeO_{3-\delta}$, the initiation temperature for sintering was lowered by Sr-deficiency, probably due to enhanced diffusion of Sr. However, for Sr-deficient samples $Sr_4Fe_6O_{13}$ is formed above ~775°C causing a significant decrease in the sintering rate. It is therefore necessary to avoid Sr-deficiency in order to obtain dense $SrFeO_{3-\delta}$ ceramics. The densification rate was significantly increased by Co-substitution. Dense ceramics (>95% of theoretical density) of Sr-excess and Co-substituted $SrFeO_{3-\delta}$ were obtained by sintering in the temperature region 1000-1200°C. The grain size increases by increasing temperature, decreasing partial pressure of oxygen and Co-substitution. Exaggerated grain growth in the Co-substituted material occured at high temperatures. Sintering above 1200°C caused all materials, apart from Co-substituted $SrFeO_{3-\delta}$ in oxygen, to swell and develop a porous microstructure. The swelling mechanism was related to heterogenous phase equilibria, which are reductive in nature and lead to evolution of oxygen gas. The phase equilibria are governed by the cation non-stoichiometry of the materials.

The present findings demonstrate the importance of controlling the A/B ratio of ternary transition metal perovskite oxides in order to achieve ceramics with the desired homogenous microstructure. The mixed valence state of the transition metal may lead to swelling at high temperatures due to redox phase equilibria involving secondary phases. Oxidation during cooling and reduction during heating may also introduce cracking due to the considerable volume change caused by the change in the valence state

1.2 Mechanical properties (Paper III and IV)

Compressive creep performance of Sr-deficient and Sr-excess $SrFeO_{3-\delta}$ materials have been investigated in the temperature range 800-1000°C and in the stress range 2.5-25 MPa. The density of the materials was 4.99 g/cm^3 and 5.25 g/cm^3, respectively, which correspond to a porosity of about 2 and 5%. Both materials contained secondary phases due to the cation non-stoichiometry. The creep rate was faster for the Sr-deficient material than the Sr-excess material. The stress exponent was close to unity and the activation energy was 260±30 kJ/mole for both materials. The results can be explained by a cation diffusion mechanism as the activation energy for oxygen diffusion is significantly lower.

The mechanical properties of phase pure $LaCoO_{3-\delta}$ and $La_{0.8}Ca_{0.2}CoO_{3-\delta}$ have been investigated in the temperature interval 25-800°C by 4-point bending and SENB/SEVNB methods. Both materials show a non-elastic stress-strain behavior during 4-point bending experiments, and during loading-unloading cycles hysteresis loops are observed. Residual strain is stored in the material after unloading, and a mechanism related to ferroelastic domain switching in the rombohedral perovskite is proposed. The bending strength for 98% dense $La_{0.8}Ca_{0.2}CoO_{3-\delta}$ is measured to be 111±18 MPa at RT and decreases with increasing temperature. Bending strength for 93% dense $LaCoO_3$ is in the range of 65 MPa at RT. Large pores/defects are decisive for the strength for both materials. Fracture toughness of $La_{0.8}Ca_{0.2}CoO_{3-\delta}$ measured by the SENB and SEVNB method coincide and are equal to 2.2 MPa·m$^{1/2}$ at RT and decreases to around 1 MPa·m$^{1/2}$ at 300-800°C. A decrease in fracture toughness is consistent with a ferroelastic behavior as the rhombohedral distortion decreases with increasing temperature. For $LaCoO_{3-\delta}$ the measured value at RT is 1.3 MPa·m$^{1/2}$.

1.3 Slip casting (Paper V)

Different non-aqueous solvents and dispersing agents have been investigated in order to prepare a stable dispersion of $LaCoO_{3-\delta}$ powder for slip casting. Initially, several dispersion agents were tested by observing the sedimentation rate in different organic solvents. 4-hydroxy benzoic acid (PHBA) in ethanol provided a stable suspension and the highest sediment density for $LaCoO_{3-\delta}$ powder, and this system was therefore further studied. The change in rheological properties with respect to dispersant level and solid loading was measured by a rotational viscometer consisting of two concentric cylinders. The suspension showed pseudo plastic behavior, and the deviation from Newtonian behavior was larger at high solid loading and low contents of PHBA. The viscosity of the suspension decreased by PHBA addition, but increasing the amount above 1 wt% had only a negligible effect. The relation between viscosity and solid loading was shown to be described by the Mooney equation. Greenbodies formed as end-closed tubes were prepared by slip casting of a suspension of 25 vol% $LaCoO_{3-\delta}$ in ethanol and 1 wt% PHBA (with respect to solid). The tube walls were 1 mm after a casting time of 10 min, and approximately 40% of theoretical density was obtained. A slow drying rate was required in order to minimize cracking. Coating of the plaster mould by alginate made the releasing of the dry greenbody easy. Sintering of the green tube resulted in a density of 98.7% of theoretical.

2 INTRODUCTION

2.1 Background

The natural mineral *Perovskite* ($CaTiO_3$) has given name to a large group of ternary compounds with closely related crystal structures. The various electrical and magnetic properties of ABO_3 perovskites make them interesting for several applications, and the functional properties are tailored by substitution at the A and/or B site. The first perovskite in commercial use was the ferroelectric $BaTiO_3$ for capacitor applications. In the development of solid oxide fuel cells (SOFC) perovskites are some of the most promising candidate materials [1, 2]. For instance, $(La,Sr)MnO_3$ has been intensively studied for the application as cathode in SOFC [3, 4], and $LaCrO_3$ for the use as an interconnect material [5, 6]. For these applications a high electronic conductivity is desired. Only pure ionic conductors are interesting for use as electrolyte. Traditionally YSZ has been the best choice as electrolyte in SOFC, but recently Sr and Mg substituted $LaGaO_3$ has been shown to have higher oxygen conductivity, and is therefore a candidate material for the electrolyte [7, 8].

Several perovskite oxides containing transition metals exhibit a high catalytic activity in various processes such as oxidation of CO and CH_4, and reduction of NO_x [9, 10]. For instance, $LaBO_3$ (B=V, Cr, Mn, Fe, Co, Ni) catalyzes the oxidation of CO, and $LaCoO_3$ has been shown to have the highest catalytic activity in this series [11, 12]. It was shown to be a strong relation between catalytic activity and the preparation process of the perovskite. This is related to thermal treatment affecting the oxygen non-stoichiometry and valence state of the transition metal which influence the adsorption and reaction at the surface. Structural phase transitions governed by substitution have also been shown to have an effect on the catalytic activity of perovskites. The catalytic activity is at maximum around the transition because of a high structural disorder and high density of surface defects. For $La_{0.7}Sr_{0.3}Co_{1-x}Fe_xO_{3-\delta}$, the maximum rate of CO oxidation is for x=0.05 due to the hexagonal to cubic phase transition [13].

Recently, perovskites exhibiting both high ionic and electronic conductivity (mixed conductivity) have been given much attention. One possible

application for mixed conductors are oxygen sensors [8, 14]. The change in oxygen stoichiometry governed by a change in oxygen partial pressure is associated with a change in physical properties such as electrical conductivity. If there is a linear dependency between conductivity and partial pressure of oxygen in a sufficient range of partial pressures, the partial pressure of oxygen can be decided based on conductivity measurement.

Mixed conductors are most interesting in relation to the development of oxygen permeable membranes (OPM) [15, 16, 17]. The advantage of mixed conductors compared to ionic conductors such as YSZ for this purpose is that there is no need for an external circuit or electrodes to allow transport of electrons. When the mixed conductor is placed in a gradient of oxygen partial pressure, oxygen will spontaneously be transported through the membrane from the high pressure to the low pressure side, as shown in Fig. 2.1. This kind of membranes have a future use for production of pure oxygen gas by separating it form air, and in conversion of natural gas to H_2(g) and CO(g). There will be a considerable cost reduction by using OPM in the production of syngas (CO/H_2). Apart from having high electronic and ionic conductivity, the membrane material must be stable under both oxidizing and reducing conditions. The material must of course be gas-tight which require a high density, usually more than 92% of theoretical density. The membrane needs to have a certain mechanical strength in order to avoid failure during operation and installation. The resistance to creep at the operation temperature is decisive for the lifetime of the membrane.

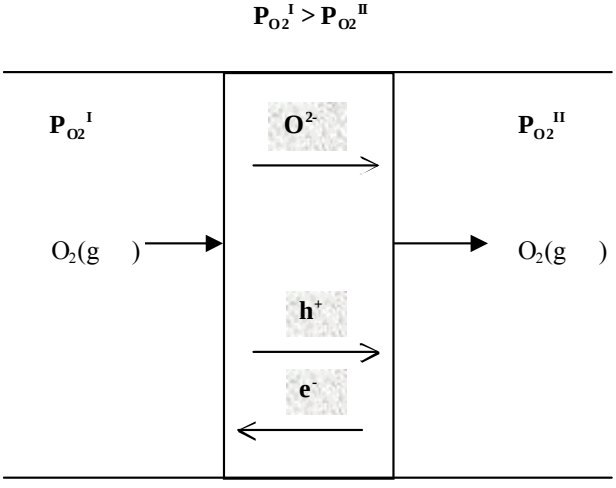

Figure 2.1: The mode of operation for an oxygen permeable membrane in a gradient of oxygen partial pressure ($P_{O2}^{I} > P_{O2}^{II}$) .

$(La,Sr)(Fe,Co)O_3$ based ceramics have been shown to have very high ionic and electronic conductivity in addition to having a wide stability range and they are therefore promising for OPM. The electrical and structural properties of these compositions have been studied thoroughly [18, 19, 20], but detailed studies of material preparation and mechanical properties are rare.

One of the main challenges in the development of SOFC and oxygen permeable membranes (OPM) is the ability to prepare materials with the desired density and microstructure. For OPM dense materials are required in order to selectively separate gas. High density is also required for the electrolyte and interconnect in SOFC while the cathode and anode must be porous to allow gas transport [1]. The control of density and microstructure of ceramic materials start with powder preparation. The sintering behavior is dependent on particle size, particle distribution and phase composition. Different powder preparation techniques exist. Traditionally the solid state method have been used, but lately several wet chemical methods have been introduced which allow mixing of the constituents at an atomic level. Smaller particle size and thereby lower sintering temperature is achieved by wet chemical routes [21]. Control of chemical composition by these methods is however demanding, especially when substitution at the A and/or B site is required. An A/B ratio deviating from unity can be difficult to avoid, and it strongly affects the phase composition, sinterability and final microstructure of the material. Often either an A-site excess or a B-site excess is more favorable, and it may be advantageous to consciously prepare non-stoichiometric materials in order to take advantage of some properties or to avoid formation of specific secondary phases.

The shape-forming process of the powder into a greenbody is the next step. A homogeneous density of the green body is essential because any defects or density gradients will affect the final microstructure [22]. A number of shaping techniques are available for ceramic powders. Examples are tape casting for films, slip casting for complex shapes, and uniaxial or isostatic pressing for simple shapes. Different additions such as stabilizers, plasticizers and binders are used depending on the forming technique [23].

The temperature program and atmosphere for sintering is then optimized to prepare a ceramic material with the desired microstructure. The phase equilibria in the material system must be considered in relation to the firing procedure. High density and small grain size increase the strength and fracture toughness, but a small grain size also decreases the resistance to creep to some extent. Secondary phases can affect the mechanical properties

depending on composition and morphology. Defects such as large pores or flaws are decisive for the strength of a ceramic material and should therefore be avoided [24]. Functional properties are mainly depending on chemical composition, and the microstructure such as grain size is expected to be of less influence. However, porosity, average grain size, and phase composition may be important parameters also for the functional properties. This work have concentrated on preparing homogeneous ceramic microstructures that have the best mechanical properties, and the effect on functional properties have not been investigated.

2.2 Aim of the work

The motivation for the present work was the recent interest to develop dense oxygen permeable ceramic membranes for partial oxidation of natural gas, or for separation of oxygen gas from air. The project has been carried out as a part of a collaboration between research groups at Department of Chemistry at NTNU and The University of Oslo and research groups from the two major Norwegian oil companies Statoil and Norsk Hydro. The research group at NTNU was given a particular responsibility to study the preparation of dense ceramic materials.

The first goal of the present work was to establish methods to prepare sub micron powders with the desired chemical composition. Wet chemical routes were chosen as both the particle size and the chemical composition of the powder is tailored by modifying the chemistry. Furthermore the ceramic powders obtained in these synthesis were applied in the investigations of the sintering properties of the materials. Unfortunately it was early experienced that the control of the chemical composition was demanding, particularly in chemically substituted materials. It turned out that the presence of secondary phases due to improper control of chemistry was one of the most important parameters regarding the sinterability and the development of the microstructure during heat treatment. The effect of cation non-stoichiometry on the sintering behavior was therefore systematically studied. $LaCoO_{3-\delta}$ and $SrFeO_{3-\delta}$ based materials were chosen as appropriate for the synthesis and sintering studies. $LaCoO_{3-\delta}$ was chosen as good model system as it is an important component in mixed oxide conductors. This material achieves considerable ionic conductivity by substitution of La by Sr or Ca. $SrFeO_{3-\delta}$ and Co substituted $SrFeO_{3-\delta}$ was chosen as the main material in the

collaboration project described above. Pure $SrFeO_{3-\delta}$ materials has a relatively high permeability for oxygen.

The knowledge of phase equilibria in oxide systems was pointed out to be important for the sintering behavior. A review of pseudo binary phase diagrams of the first row transition metal oxides in combination with La_2O_3, SrO or CaO was done to get a better knowledge of the phase relations and possible effects on sintering properties. The literature on sintering of selected perovskites was also reviewed. The aim of the work was to achieve a fundamental understanding of the sintering mechanisms of these perovskite materials and to prepare dense and homogeneous materials in order to optimize the mechanical properties. For several of the materials it was early discovered that dense ceramics expanded at high temperature. Special effort was given to understand the nature of this particular interesting phenomenon.

Proper mechanical properties of these mixed conductors are also necessary in order to realize the membrane applications. High strength and fracture toughness are essential to avoid cracking due to temperature fluctuations. Failure is particular critical in relation to thermomechanical stresses due to mismatch of thermal expansion with joining of the membrane material to the support. So far only a limited number of data have been published on the mechanical properties of perovskites. The research group at the Department aimed to obtain the first data on the bending strength and fracture toughness of $LaCoO_{3-\delta}$ ceramics. The work would benefit from the experience with the sintering studies of these materials. The initial work[App.1] discovered the unusual non-elastic behavior of these ceramic materials. In order to obtain more information on the non-elastic nature of the materials, further measurements by 4-point bending and x-ray diffraction were carried out.

The observation of the post sintering swelling and relative fast deformation at high temperatures indicated high creep rates of these materials. It was therefore initiated an investigation of the creep behavior of the $SrFeO_{3-\delta}$ based ceramics. The composition of the materials, which were tested, was chosen based on the previous sintering studies. Creep performance is also very important in relation to the geometrical stability and the lifetime of membranes operating at high temperature. Creep is very critical in cases there a pressure gradient is applied over the membrane in order to increase the driving force for oxygen transport.

The last goal of the project was related to the shape-forming process of ceramic membranes. The most probable design of an oxygen permeable membrane is a tube in which the gas feed on the inside and outside can easily

be controlled. Here, the possibility to prepare ceramic tubes of $LaCoO_{3-\delta}$ by slip casting was explored. Particular emphasis was given to the optimization of the rheological properties of the slip in order to achieve homogeneous green bodies and dense tubes.

2.3 The perovskite structure

Quite a few ternary oxides crystallize in the perovskite structure, ABO_3. A is a large cation, usually a rare earth metal, an alkali metal or an alkaline earth metal. B is a smaller cation, often a transition metal. Several combinations of oxidation states are possible, such as $A^{I}B^{V}O_3$, $A^{II}B^{IV}O_3$ and $A^{III}B^{III}O_3$, where the sum of valences of the A and B cation is six. A simple calculation based on ionic radii of the component ions may predict whether the ternary oxide will obtain the perovskite structure or not. The ratio is known as the Goldschmidt factor [25], and is given in Eq. 2.1.

$$t = \frac{r_A + r_O}{\sqrt{2}(r_B + r_O)} \qquad t \leq 1 \qquad (2.1)$$

where r_A, r_B and r_O are ionic radii of the A cation, B cation and oxygen ion, respectively. For the ideal perovskite t=1, but perovskite structures are formed for t values as low as 0.75. The ideal perovskite structure is shown in Fig. 2.2 a. The B-cation is octahedral coordinated by oxygen-ions, and the A-cation is 12-coordinated by oxygen-ions. The ideal perovskite has the cubic symmetry. However, in reality few perovskites obtain the ideal cubic crystal structure. In many cases either a tilting or a deformation of the oxygen octahedra results in lower crystal symmetries and thereby larger unit cells [26].

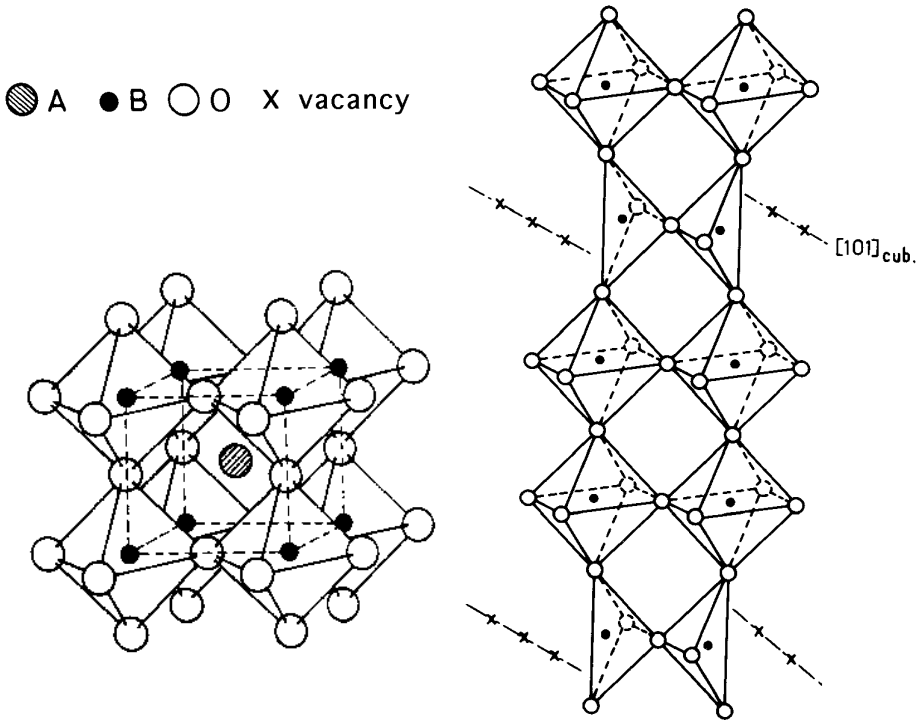

(a) (b)

Figure 2.2. a) The ideal perovskite structure [27] and b) the brownmillerite structure [28]. A-cations are not shown in b).

Another important parameter regarding the crystal symmetry is the oxygen content, or the oxygen stoichiometry. The sum of valences of the cations will determine the oxygen stoichiometry, and again affect the crystal structure. The oxygen non-stoichiometry is indicated by δ in $ABO_{3-\delta}$. Oxygen deficient perovskites are the far most common non-stoichiometric compounds, but oxygen excess materials like $LaMnO_{3.16}$ are also known. Often A and/or B cations are substituted by lower valent cations in order to increase δ and enhance oxygen ion conduction. When transition metals are involved, the valence state of the transition metal will depend on temperature and partial pressure of oxygen. A change in valence state of the transition metal will be followed by a change in oxygen stoichiometry. When δ=0.5 a new crystal structure called the brownmillerite structure named after the mineral $Ca_2Fe_2O_5$ can be formed, Fig. 2.2 b. The oxygen vacancies are ordered in

such a way that alternating layers of octahedral and tetrahedral coordinated B-cations are formed [28]. Other structures related to the brownmillerite structure where the oxygen vacancies are ordered in a different way giving square pyramidal coordinated B-cations also excist [29]. Structures with all these three different coordinations of the B-cation have been characterized [30]. Other ordered structures may also be formed between $\delta=0$ and $\delta=0.5$ depending on the chemical composition. One example of the complexity of different structures is $SrFeO_{3-\delta}$ shown in Fig 2.3. Below 400°C the crystal structure change from the cubic perovskite ($\delta\approx3.0$) via tetragonal ($\delta\approx0.125$) and orthorombic ($\delta\approx0.25$) perovskites to the orthorombic brownmillerite structure ($\delta\approx0.5$). Two-phase mixtures are formed between these δ-values. The oxygen stoichiometry of the ordered phases can be expressed by the formula $SrFeO_{3-(1/n)}$ where $n=\infty$, 8, 4, 2[18].

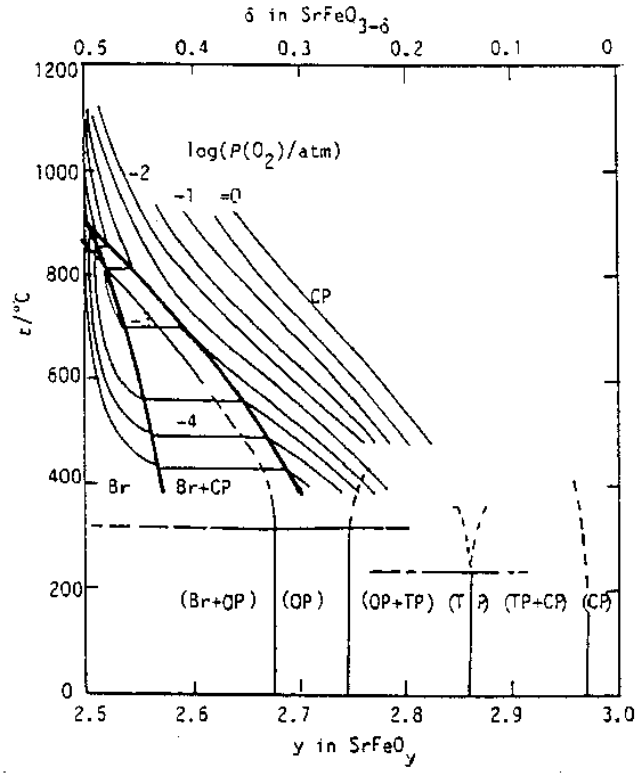

Figure. 2.3 : Phase diagram for $SrFeO_{3-x}$ as a function of x and temperature [18, 19].

Most of the non-cubic perovskites go through a phase transition to the cubic perovskite structure by increasing the temperature. The tilting or deformation of the oxygen octahedra becomes unstable because of lattice vibrations at high temperature resulting in a cubic structure. For instance, $LaCoO_3$ has a rhombohedral crystal structure ($R\bar{3}c$) at room temperature [31]. The rhombohedral distortion indicated by the rhombohedral angle (α_r) decreases with increasing temperature, and has a significant distortion from cubic structure at 1000°C. Extrapolating the data for the rhombohedral angle, $LaCoO_3$ becomes cubic at 1400°C when α_r=60° [32]. When La is substituted by Sr at room temperature the rhombohedral angle decreases linearly with increasing Sr content (x), and the structure becomes cubic at x=0.55 [33].

For $SrFeO_{3-\delta}$, the phase relations are much more complicated than for $LaCoO_3$. Different crystal structures are formed depending on the oxygen stoichiometry, and their transition temperature to cubic symmetry are different as shown in Fig. 2.3. For the brownmillerite structure $SrFeO_{2.5}$ the transition to a disordered cubic perovskite structure occurs at ~850°C [34]. This phase transition represents an order-disorder transition where the oxygen vacancies become randomly distributed at the oxygen sites. However, there has been indications of a partially ordered phase also above this temperature [34, 35]. The brownmillerite-perovskite transition temperature decreases with decreasing oxygen partial pressure [19]. By substituting Fe by Co the cubic perovskite structure is stabilized at lower temperatures [36].

There are several other structures related to the perovskite structure. By changing the cation ratio a variety of different phases can be formed. A well known series where A/B>1 is the Ruddlesden-Popper phases of the general formula $A_{n+1}B_nO_{3n+1}$ (n=1, 2, 3 ...) [37]. These phases consist of stacks of n two-dimensional perovskite layers of corner shearing BO_6-octahedra $[ABO_3)_n]$ separated by a single rock-salt AO-layer. Many of these phases are only stable at elevated temperatures or under reduced conditions. For instance in the La-Co-O system, La_2CoO_4 [38] and $La_4Co_3O_{10}$ [39] can be prepared at low oxygen partial pressures.

2.4 Functional properties of perovskites

The material properties that make perovskites such interesting materials are mainly the electrical and magnetic properties. Ferroelectric perovskites such as $BaTiO_3$ are well known, and superconducting perovskites have been characterized, however these properties have not been considered in the following discussion. By playing with the composition of ABO_3 perovskites one can design materials with almost any electrical or magnetic property. The magnetic properties vary between ferro-, antiferro-, and paramagetism, and the electronic properties between insulating, semi-conducting and metallic. For instance, $LaNiO_3$ is a metallic conductor and Pauli paramagnetic at room temperature [40]. $LaCoO_3$ is paramagnetic and semi-conducting at room temperature with a transition to metallic conduction at high temperature [41, 42]. $LaFeO_3$ is an antiferromagnetic insulator [43, 44]. The spin state of the d-electrons of the B-cation and the B-O distance are decisive for magnetic properties and electronic conduction [45]. This is because of the possibility of cation-anion-cation interaction between the *d*-orbitals of the B-atoms and the *p*-orbitals of oxygen atoms along the cube edge of the unit cell. When there is little or no overlap between oxygen *p*- and metal *d*-orbitals another mechanism related to the mixed valence state of the B-cation can occur. At low temperatures the electrons are localized at the B-cation favored by phonon-electron interactions. This means that the electron has to move along with a polarization which results in a low mobility and low electronic conductivity. The diffusion of electrons is termed polaron hopping, and it is a thermally activated process. Increasing temperature will increase the conductivity. This polaron hopping model is only valid in compounds with mixed valence cations [27].

Several perovskites are oxygen ion conductors. The ionic conductivity is due to the presence of oxygen vacancies in the structure. The oxygen vacancy concentration is dependent on the sum of valences of the A and B cations. By substituting A and/or B in ABO_3 by lower valent cations the oxygen vacancy concentration and the ionic conductivity can be increased. For instance, $La_{1-x}Sr_xGa_{1-y}Mg_yO_3$ is a pure ionic conductor with conductivity even higher than YSZ [7].

Both ionic and electronic conductivity (mixed conductivity) is common for perovskites, and substitution on A and/or B site is often necessary in order to increase the conductivity to the desired level. Both $LaCoO_{3-\delta}$ and $SrFeO_{3-\delta}$ are mixed conductors, and the conductivity is increased by substituting by lower valent cations. $La_{1-x}Sr_xCoO_3$ has a transition from semi conducting to metallic at x~0.25 as shown in Fig. 2.4 [32, 46].

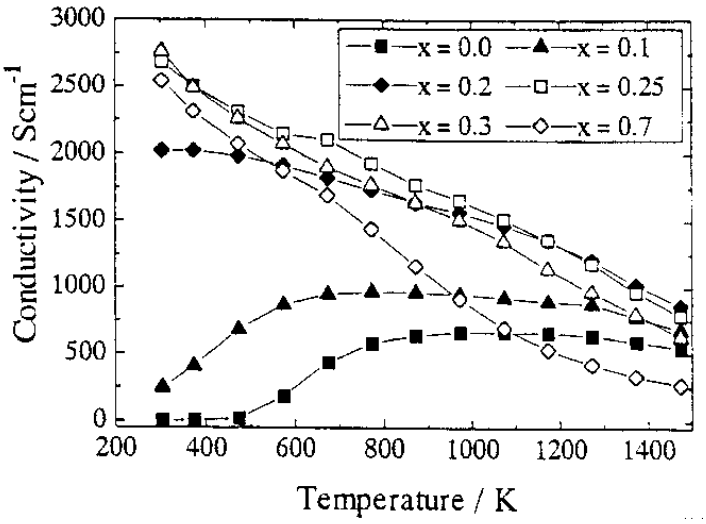

Figure 2.4: Electrical conductivity versus temperature for $La_{1-x}Sr_xCoO_3$ ($0.0 \leq x \leq 0.7$) in air [46].

The type of conductivity is changing with oxygen partial pressure as shown for $Sr_2Fe_2O_5$ in Fig. 2.5. At lower partial pressures of oxygen the conductivity is of *n*-type and at higher partial pressures of oxygen *p*-type conductivity is dominating [47]. If the oxygen vacancy concentration is independent of oxygen partial pressure the conductivity will be proportional to $P_{O2}^{+1/4}$ in the *p*-type region and $P_{O2}^{-1/4}$ in the *n*-type region due to the defect equilibria given in Eq. 2.2 and 2.3. The minima of the curves are flat because of the contribution from ionic conductivity shown in Fig. 2.6.

$$O_o = \tfrac{1}{2}O_2 + V_o^{\cdot\cdot} + 2e' \qquad (2.2\ a)$$

$$\left[V_o^{\cdot}\right]\cdot n^2 = K_n \cdot P_{O_2}^{\ -1/2} \qquad (2.2\ b)$$

$$V_o^{\cdot\cdot} + \tfrac{1}{2}O_2 = O_o + 2h^{\cdot} \qquad (2.3.a)$$

$$\frac{h^2}{\left[V_o^{\cdot}\right]} = K_h \cdot P_{O_2}^{\ 1/2} \qquad (2.3\ b)$$

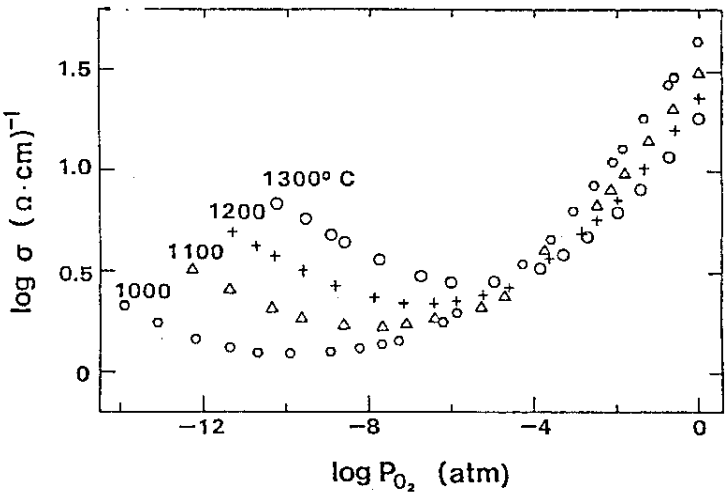

Figure 2.5: Electrical conductivity versus partial pressure of oxygen for $Sr_2Fe_2O_5$ [47].

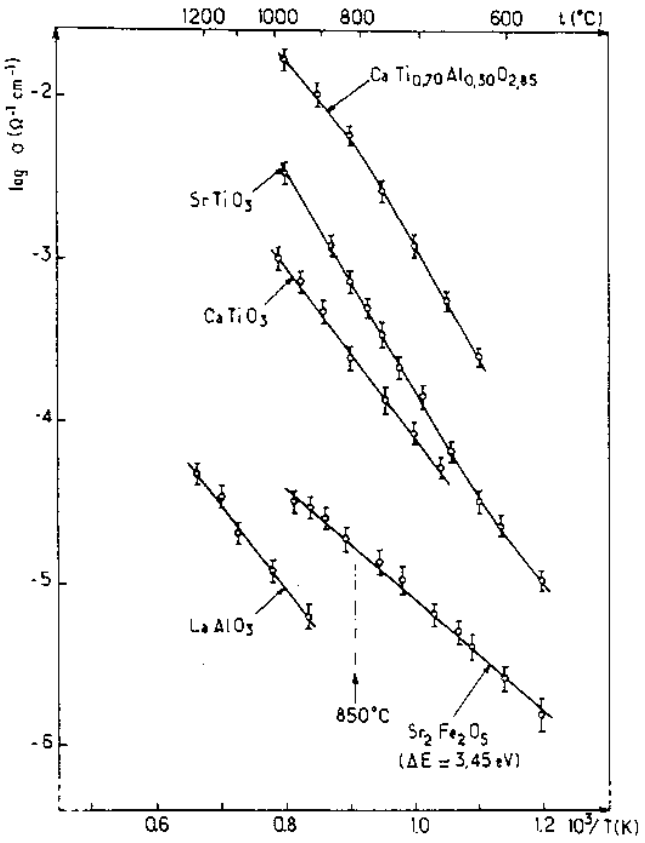

Figure 2.6: Ionic conductivity of $Sr_2Fe_2O_5$ compared to the conductivity of other oxygen conductors [34].

The ionic conductivity is strongly related to defect chemistry since it is depending on the concentration of oxygen vacancies. The variation in oxygen non-stoichiometry with oxygen partial pressure for $La_{1-x}Sr_xBO_{3-\delta}$ (B = Cr, Mn, Fe, Co) is shown in Fig. 2.7 [48]. A plateau at $\delta=0$ is observed for all compositions corresponding to stoichiometry where all oxygen sites are occupied. For $La_{1-x}Sr_xCrO_{3-\delta}$ and $La_{1-x}Sr_xFeO_{3-\delta}$ a plateau at $\delta=x/2$ is observed corresponding to electronic stoichiometry where the average valence of B is 3+. This means that the electrons are localized at the B atom. $La_{1-x}Sr_xCoO_{3-\delta}$ and $La_{1-x}Sr_xMnO_{3-\delta}$ are metallic and the $\delta=x/2$ plateau is not observed since electrons are delocalized. It is obvious from this figure that $La_{1-x}Sr_xCrO_{3-\delta}$ is a much poorer ionic conductor compared to $La_{1-x}Sr_xCoO_{3-\delta}$ at $P_{O2} \leq 1$ atm.

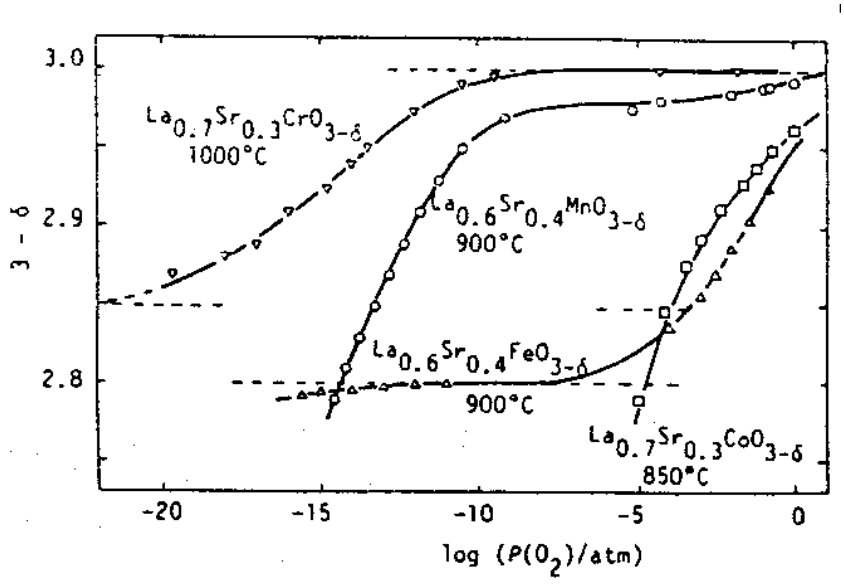

Figure 2.7: Oxygen non-stoichiometry versus oxygen partial pressure for $La_{1-x}Sr_xBO_{3-\delta}$ (B = Cr, Mn, Fe, Co) [48].

Ionic conductivity is closely related to the ordering of oxygen vacancies in the structure. This has been investigated by Kruidhof el al. [49]. They showed that there is a large increase in ionic conductivity at the order-disorder transition temperature for $SrCo_{0.8}B_{0.2}O_{3-\delta}$ (B=Cr, Fe, Co, Cu). The same has been observed in many other systems. Several materials obtaining the ordered brownmillerite structure at low temperature transform to a disordered structure at high temperature followed by a large increase in conductivity [50].

2.5 Sintering of perovskites

A literature study on the sintering of the lanthanum transition metal oxides is presented. The compositions have been restricted to the first row transition metals, $La_{1-x}(Ca, Sr)_xBO_3$ (B = Cr, Mn, Fe, Co). $SrTiO_3$ and $BaTiO_3$ have also been included.

Titanates

Sintering of $BaTiO_3$ ceramics added a number of different sintering aids have been investigated. Anderson [51] showed that the initial sintering rate of $BaTiO_3$ was very dependent on the Ba/Ti ratio. Exceeding the solid solubility limit on the TiO_2 rich side decreased the initial sintering rate due to precipitation of TiO_2. For BaO rich samples the sintering rate was highly dependent on the calcination temperature of the powder suggested to be due to secondary phases. The eutectic temperature at 1312°C in the TiO_2 rich region of the BaO-TiO_2 system [52] has been used to improve the densification by liquid phase sintering. Demartin et al. [53] observed two sintering steps, the first attributed to solid state sintering at 1240-1280°C and the second to liquid phase sintering at 1300-1310°C. 94-98% of theoretical density (%TD) was obtained in the temperature interval 1320-1350°C.

Abnormal grain growth has been a problem during preparation of dense $BaTiO_3$ ceramics, especially since the dielectric properties is very dependent on the microstructure. Demartin [53] found that the microstructure depended on the heating rate. Long time during heating in the temperature interval 1220-1300°C initiates solid state grain growth, and the liquid phase above 1300°C also enhance grain growth. Several different additions have been used to inhibit abnormal grain growth. Among others, Dy_2O_3, NiO, Sb_2O_3, ZrO_2. have been shown to work successfully by introducing secondary phases at the grain boundaries and thereby inhibit abnormal grain growth.

Also for $SrTiO_3$ ceramics, liquid phases are usually formed to enhance densification. Fujimoto et al. [54] prepared dense $SrTiO_3$ ceramics by adding excess TiO_2 in addition to Al_2O_3 and SiO_2. This lead to formation of a wetting liquid phase due to the eutectic in the SrO-TiO_2 system at 1440°C, and dense materials were obtained at 1450°C. In order to decrease the sintering temperature further Cheng et al. [55] added Li_2CO_3 to $SrTiO_3$. They

found an increasing density when up to 3 wt% Li_2CO_3 was added, and a decrease by further addition. Dense materials were achieved at temperatures as low as 960°C. The enhanced densification was due to a liquid phase. The effect of Li_2CO_3 addition was less at higher temperatures because of evaporation of excess liquid. The decrease in density above 3 wt% addition was attributed to evaporation.

Chen et al. [56] investigated sintering of $SrTiO_3$ added V_2O_5 as a sintering aid in the temperature interval 1100-1350°C. They obtained increased density with addition of V_2O_5, and 93%TD at 1250°C (4-6 wt% V_2O_5) was achieved due to formation of a liquid phase. However, precipitation of TiO_2 lead to formation of large pores. Higher sintering temperatures and lower V_2O_5 content lead to abnormal grain growth. Addition of excess SrO surpressed the precipitation of TiO_2, and a dense small grained microstructure could be formed at 1250°C when a small amount of V_2O_5 was added.

Chromites

Sintering of pure $LaCrO_3$ requires a very high sintering temperature, but at high temperatures the evaporation of Cr species makes it difficult to achieve a dense material. Yokokawa et al. [57] discuss a possible mechanism involving $CrO_3(g)$ to condense as a Cr_2O_3 layer at the interparticle neck during the initial stage of sintering in air and thereby inhibiting further densification. Mori [58] investigated the sintering of $LaCrO_3$ with variable La/Cr ratio, and found that Cr-deficient materials obtained a higher density than the Cr-excess materials, though not more than 67%TD. This difference was explained by a lower vapor pressure of Cr at Cr-deficiency. However, the Cr-deficient materials cracked due to formation of $La(OH)_3$.

Substitution of La by an alkali earth metal such as Sr or Ca has been shown by many authors to increase the sinterability of $LaCrO_3$. The increased sintering rates are mainly due to formation of transient liquid phases. Liquid phase sintering and phase transitions in Ca substituted $LaCrO_3$ have been investigated by Chick et al. [59]. The compositions were varied between A-site excess and A-site deficient compositions by changing the Ca content in $La_{0.7}Ca_xCrO_3$ ($0.25>x>0.35$). Higher densities were obtained for Ca-enriched materials (>90%TD) compared to Ca-deficient materials (<60%TD). For $x>0.3$ the sintering curve had two rapid shrinkage events. The first and second event were caused by melting of the transient secondary phases

$CaCrO_4$ and $Ca_3(CrO_4)_2$, respectively. The total Ca/Cr ratio in the secondary phases changes when the temperature increases as the solubility of Ca in the perovskite increases. The phase transitions during heating can be fairly well described by the binary CaO-Cr_2O_3 phase diagram [60]. A decreasing onset temperature for the sintering steps by increased Ca-content was explained by melting point depletion due to increased La content in the secondary phases. At $x<0.3$ the amount of liquid phase is much smaller as can be seen from the binary CaO-Cr_2O_3 phase diagram, and the second shrinkage event does not occur since the $Ca_3(CrO_4)_2$ phase never forms. These phase relations explain the lower density.

Also during sintering of Sr substituted $LaCrO_3$, evaporation of Cr containing species is a problem. In order to decrease the evaporation rate of Cr, Groupp et al. [61] decreased the partial pressure of oxygen and obtained high densities (>95%TD) at $P_{O2}<10^{-10}$ atm in the temperature interval 1720-1740°C. Bansal et al. [62] added $SrCO_3$ as a sintering aid and obtained ~92%TD at 1600°C. Bates et al. [63] investigated the sintering behavior at various degrees of substitution and found that sintering started at around 1100°C when $x\geq0.12$. Several sintering stages were observed, and a stage at around 1200°C was attributed to the melting of $SrCrO_4$. The reason for the other two stages, one around 1100°C and the other above 1400°C, was suggested to be due to formation and disappearance and unidentified secondary phases. The cation stoichiometry was also shown to have a large influence on the sintering behavior. Maximum densities were obtained at slight A-site excess and A-site deficiency with a minimum in between at A/B=1.0.

Substitution at the B-site in $LaCrO_3$ has also been investigated by many workers. Hayashi et al. [64] found that substitution of Cu or Zn at the B-site improved the sinterability and >95%TD was obtained at 1600°C. Jin et al. [65] tried to substitute on the B-site by Mg, Ni, Cu or Zn, and they found that Cu or Zn substitution improved the sintering properties, while Ni and Mg substitution had a small or no effect. Sintering of the Zn substituted $LaCrO_3$ was very dependent on temperature, and severe grain growth and inter granular fracture was observed in dense samples. This behavior indicates formation of a liquid phase during sintering. However, this was not discussed by the authors.

Substitution at both A- and B-site by Ca and Co, respectively, was investigated by Koc et al. [66]. They found that Ca and Co substitution lowered the sintering temperature, and dense materials (>94%TD) were

obtained at 1400°C. The improved sintering was attributed to a transient liquid phase due to melting of Ca and Co rich particles arising from a non-uniform composition of the starting powders.

Manganites

$LaMnO_{3+\delta}$ is an oxygen excess perovskite, which is rather unusual. This makes the sintering properties somewhat different from the oxygen deficient perovskites. The oxygen excess leads to formation of cation vacancies. By heating, δ decreases, and followed by this the cation vacancy concentration decreases. Cation vacancies can also be formed by varying the La/Mn ratio. The phase diagram of Mn_2O_3-La_2O_3 shows that there is a relatively large region for solid solution [67]. Van Roosmalen et al. [68] investigated the effect of cation ratio on the sintering behavior of $LaMnO_{3-\delta}$. Enhanced sintering by La-deficiency was observed, showing that increased concentration of La-vacancies increases the densification rate. The densification was much slower when Mn-vacancies were introduced. They concluded that diffusion of La is the rate-limiting step during sintering of $LaMnO_{3-\delta}$.

When La is substituted by Sr, the defect chemistry changes. The number of cation vacancies are determined by the oxygen content, and by substituting La^{3+} by Sr^{2+} the oxygen content is lowered, and thereby the A-vacancy concentration. The sintering temperature is therefore increased by Sr-substitution, which also is what have been observed. In the case of Sr-substitution the ionic radius does not play an important role since La^{3+} and Sr^{2+} is more or less equal in size. However, if La is substituted by Ca or Ba the ionic radius will be an important parameter. (La, Ba)$MnO_{3-\delta}$ sinters at higher temperature than (La, Sr)$MnO_{3-\delta}$, and (La, Ca)$MnO_{3-\delta}$ sinter at lower temperature. This is because $r(Ca^{2+}) < r(Sr^{2+}) < r(Ba^{2+})$, and a smaller ionic radius will enhance diffusion of A-cation, leading to faster sintering. This is more or less what Chacraborty et al. [69] did when Bi_2O_3 was added to (La, Sr)MnO_3 in order to improve the sintering properties. It was shown that the small Bi^{3+}-ions enter the La-lattice sites, and by that enhanced the diffusivity of A-cations. The sintering rate was thereby increased.

Stevenson et al. [70] investigated the sintering of A-site excess/deficient Sr and Ca substituted $LaMnO_{3+\delta}$. The same behavior as for non-substituted

$LaMnO_{3+\delta}$ was observed, and A-site deficient compositions obtained the highest density.

The effect of sintering atmosphere on the densification of (La, Sr)MnO_3 have been investigated by Poirson et al. [71]. Sintering was performed in nitrogen, air and oxygen. The sintering temperature was shifted towards lower temperature in nitrogen and towards higher temperature in oxygen. These observations shows that the picture is not as clear concerning the rate determining species during sintering. Increasing partial pressure of oxygen should increase the concentration of cation-vacancies and increase the sintering rate based on previous results, however the opposite is observed here.

Studies on the densification behavior of $La_{1-x}A_xMnO_{3\pm\delta}$ (A=Ca, Sr) have also been conducted by Evju [72] and Watterud [73]. It was confirmed that A site deficient manganites sintered at lower temperature ralative to stoichiometric materials. A site excess was observed to inhibit sintering. Cation non-stoichiometry was observed to cause swelling at high temperature.

Ferrites

Sagdahl et al. [74] investigated sintering of Fe-excess and Fe-deficient $LaFeO_3$ in the temperature interval 1100-1600°C. Secondary phases played an important role on the sinterability and microstructure. Fe-excess lead to formation of a liquid phase for T>1430°C, resulting in exaggerated grain growth and swelling. The swelling was explained by heterogeneous phase equilibria that were reductive in nature and lead to evolution of oxygen gas. For Fe-deficient $LaFeO_3$ the presence of La_2O_3 inhibited densification and grain growth. High density (~95%TD) and small grains (d<10 μm) were obtained for materials with a slight Fe-excess sintered at ~1200°C. Swelling of Sr substituted $LaFeO_3$ has also been observed by Sagdahl et al. [75]. Preliminary investigations suggest that this is related to non-stoichiometry and secondary phases observed in this work.

Tsai et al. [76] prepared ceramics of composition $La_{1-x}A_xFe_{0.8}Co_{0.2}O_3$ (A=Ca, Sr or Ba) and densities below 87%TD were reported for x=0.6 at 1200°C. By increasing the Ba content to x=0.8 the density increased to 98%TD.

The densification behavior of $SrFe_{1-x}(Co,Cu)_xO_{3-\delta}$ ceramics has previously been studied by several groups. Densities higher than 96% have not been obtained, and swelling at high temperature has been reported. Kokhanovski et al. [36] prepared gas-tight ceramics of the composition $SrFe_{1-x}Co_xO_{3-\delta}$ (x=0, 0.25, 0.5, 0.75) where a maximum density of 96% was obtained for x=0.25 in the temperature interval 1240-1300°C. The compositions x=0 and x=0.25 were found to swell at high temperature prior to melting, and this was explained by extensive oxygen evolution near the melting point. The evolution of gas is probably related to cation non-stoichiometry and decomposition of secondary phases as observed in this work.[Paper II] Some results on the density of $SrCo_{1-x-y}Fe_xCu_yO_{3-\delta}$ ceramics have also been reported by Kharton et al. [77, 78] They obtained a density of 75-95% when x, y=0-0.5, and a density of 89-91% for x=0.25 and y=0.15. The sintering temperature was reported to decrease when Co was substituted with Cu.

Cobaltites

Sintering of cobaltites has not been investigated thoroughly, however some results on density of $LaCoO_3$ based ceramics has been reported. Koc et al. [66] investigated the sintering behavior of $La_{1-x}Ca_xCr_{1-y}Co_yO_3$, and they obtained a maximum density of 95%TD for both $LaCoO_3$ and $La_{0.7}Ca_{0.3}CoO_3$ at 1400°C and 1200°C, respectively. Decreased sintering temperature by substitution of Ca, and increased sintering temperature by substitution of Cr were reported. Melting was observed between 1200-1300°C in $La_{0.7}Ca_{0.3}CoO_3$ which is considerably lower than for $LaCoO_3$ (1740°C) [79]. The low temperature melting phase is most probably related to the eutectic point at 1350°C at the Co-rich side of the CaO-CoO phase diagram [80]. Denos et al. [81] investigated the relationship between green and fired densities for $LaCoO_3$ and $La_{0.5}Sr_{0.5}CoO_3$. Higher fired densities were reported for $LaCoO_3$ than for the strontium substituted $LaCoO_3$, but the higher porosity was explained by residual unreacted products from the synthesis method. van Doorn et al. [82] reported decreased sintering temperature by increased Sr-substitution, and materials of $La_{0.7}Sr_{0.3}CoO_3$ with 96%TD and a uniform grain size of about 3μm at 1150°C was obtained. The diverging results reported shows that further investigations are needed to understand the sintering of cobaltites.

Concluding remark

The overview of results reported on sintering shows that further investigations are necessary in many of these systems in order to fully understand the sintering mechanisms. It is clear that secondary phases, either added as sintering aids or formed by deviations from cation stoichiometry play a very important role during sintering of perovskites. The secondary phases are often formed on purpose, but also improper control of composition have in many cases resulted in unwanted effects. Careful control of composition, sintering temperature and amount of sintering aids is necessary to avoid unwanted effects such as abnormal grain growth, evaporation and/or swelling.

2.6 Mechanical properties

Mechanical properties such as Young's modulus, bending strength and fracture toughness have only been studied for a few perovskite materials, even though many applications require knowledge of these properties. Several applications involve joining of different materials which have to sustain the stresses induced by mismatch in thermal expansion during heating and cooling. Also if any machining is needed the strength of the material will have to be considered. OPM and SOFC are high temperature devices, and the creep resistance at the operation temperature is decisive for the lifetime of the device. Also measurements of creep have been done in order to get information of defect chemistry and diffusion coefficients in the system.

Strength and fracture toughness

Blamey et al. [83] investigated strength and fracture toughness of $BaTiO_3$ ceramics containing different sintering aids. They reported a maximum strength of 93 MPa and fracture toughness of 0.8-0.95 $MPa \cdot m^{1/2}$ at atmospheric conditions for materials of ~3% porosity. Cheng et al. [84] measured Young's modulus of undopet $BaTiO_3$ (d~40 μm) by the vibrational resonace method. They reported a Young's modulus of 110 GPa at 25°C and an increased value of ~180 GPa above the tetragonal to cubic phase transition at 132°C. Smaller grain size (d~1 μm) decreased the values by ~ 30 GPa.

A few studies on strength and fracture toughness of $LaCrO_3$ based ceramics have been done. Sammes et al. [85] investigated the three point bending strength as a function of sintering temperature for $(La,Sr,Ca)CrO_3$. They reported a maximum RT strength of 234 MPa and 256 MPa for $La_{0.7}Sr_{0.3}CrO_3$ and $La_{0.7}Sr_{0.3}CrO_3$, respectively, both sintered at 1700°C. The same authors investigated high temperature strength in reducing environment of $La_{0.7}Sr_{0.3}Cr_{1-y}Co_yO_3$ (y=0-0.2) [86]. They observed degradation and loss of mechanical strength for the Co-substituted samples at 1000°C in H_2 or $H_2/3\%H_2O$ atmosphere. For y=0.05 the degradation time was 55-75 min, and the degradation was much faster at higher Co contents. The undoped material was stable and maintained the strength under reducing environments.

Paulik et al. [87] investigated the mechanical properties of $La_{1-x}(Ca, Sr)_xCrO_3$ (x=0.15-0.30) as a function of temperature and partial pressure of oxygen. The variation in strength was due to difference in density and microstructure. Increasing temperature decreased the 4-point bending strength for $La_{0.75}Ca_{0.25}CrO_3$ from ~120 MPa at room temperature to ~60 MPa above 600°C due to the orthorombic to rhombohedral phase transition at 250-300°C. For Sr substituted $LaCrO_3$, the strength was independent of temperature (50-80 MPa). By decreasing the partial pressure of oxygen below some critical value the strength decreased for all compositions. The diverging results from Sammes et al. [85] is probably because they reported 3-point bending strengths. The fracture toughness was measured to ~1.1 $MPa{\cdot}m^{1/2}$ and ~2.1 $MPa{\cdot}m^{1/2}$ for Ca and Sr substituted $LaCrO_3$, respectively. Decreasing the partial pressure of oxygen below $\sim10^{-10}$ atm decreased the fracture toughness. The decreased strength and fracture toughness at low partial pressure of oxygen was explained by structural changes in the lattice.

Montross et al. [88] measured strength of $LaCr_{0.9}Mg_{0.1}O_3$. The strength had a maximum value just below the orthorombic-rhombohedral phase transition temperature and decreased by further increase in temperature. Under reducing conditions, the RT strength was around 140 MPa and decreased to around 100 MPa at 600-1000°C. A maximum strength of 250 MPa was measured at 125°C. The fracture toughness showed the same temperature dependency, and a maximum value of 4 $MPa{\cdot}m^{1/2}$ that decreased to around 2 $MPa{\cdot}m^{1/2}$ at 1000°C was measured. The mechanism for toughening was hypothesized to be due to retained high-temperature rhombohedral phase below the transition temperature.

D'Souza and Sammes [89] investigated mechanical properties of $La_{0.875}Sr_{0.125}MnO_{3+\delta}$. They observed a decease in strength from 164 MPa at

RT to 109 MPa at 400°C, and attributed the decrease to the orthorombic-rhombohedral phase transition in the temperature range 150-250°C. Above 400°C the strength increased again to 150 MPa at 800°C and 222 MPa at 1000°C. The increase in strength was explained by change in oxygen stoichiometry and increased crystal symmetry with increasing temperature.

Mechanical properties of $La_{1-x}(Ca, Sr)_xCoO_3$ (x = 0, 0.2) was investigated in the temperature interval 25-850°C by Orlovskaya et al.[App.1] 4-point bending strength at 25°C of $LaCoO_3$ (83%TD), $La_{0.2}Sr_{0.2}CoO_3$ (90%TD), and $La_{0.2}Ca_{0.2}CoO_3$ (99%TD) was measured to 53 MPa, 76 MPa, and 150 MPa, respectively. The bending strength was relatively independent of temperature for the two first compositions, while $La_{0.2}Ca_{0.2}CoO_3$ decreased linearly to ~70 MPa at 850°C. The difference in strength was related to porosity. Fracture toughness of $La_{0.2}Sr_{0.2}CoO_3$ and $La_{0.2}Ca_{0.2}CoO_3$ was ~0.7 $MPam^{1/2}$ and ~1.0 $MPam^{1/2}$, respectively, and Young's modulus was reported to be ~112 GPa for $La_{0.2}Ca_{0.2}CoO_3$. Hardness in the range 7-11 GPa was also reported for $La_{0.8}(Ca, Sr)_{0.2}CoO_3$.

Mechanical properties of $(La,Sr)(Ga,Mg)O_3$ have been investigated because the possible application as electrode in SOFC requires a certain mechanical strength. A decreasing strength with increasing temperature from 162 MPa at RT to 55 MPa at 900°C has been observed for $La_{0.9}Sr_{0.1}Ga_{0.8}Mg_{0.2}O_3$ [90]. The same trend have been observed for $La_{0.8}Sr_{0.2}Ga_{0.8}Mg_{0.2}O_3$ where the strength decreased from ~150 MPa at RT to ~100 MPa in the range 600-1000°C. The fracture toughness showed the same decreasing trend with increasing temperature and 2.2-2 $MPa{\cdot}m^{1/2}$ was measured at RT and ~1 $MPa{\cdot}m^{1/2}$ in the temperature range 400-600°C. Young's modulus decreased from 190 GPa at RT to ~120 GPa at 500°C. The loss in mechanical properties was attributed to the phase transition from monoclinic to rhombohedral structure at ~500°C. Ca and Ba substituted materials were also investigated, but these compositions had poorer mechanical properties compared to the Sr substituted materials [91]. The change in mechanical properties by increasing Mg content for have been investigated for $La_{0.8}Sr_{0.2}Ga_{1-x}Mg_xO_3$ [92]. A decreasing strength with increasing Mg content was observed. By increasing x from 0.1 to 0.2 at RT the strength decreased from 139 MPa to 113 MPa and the fracture toughness from 1.6 $MPa{\cdot}m^{1/2}$ to 1.3 $MPa{\cdot}m^{1/2}$.

Creep

Studies on creep of perovskite ceramics have been restricted to a few material systems so far. The mechanism for creep have mostly been determined to be diffusion controlled by cations either through lattice or grain boundaries. Often the motivation for creep measurements have been to gain information on diffusion coefficients or defect chemistry within the system.

Creep of $CaTiO_3$ has been studied because it is an analog of $(Mg,Fe)SiO_3$ perovskite which makes up most of the Earth's lower mantle (670-2900 km), and therefore has been interesting for geological reasons. Karato and Li [93] investigated creep of $CaTiO_3$ in the temperature interval 1180-1300°C and found that deformation was controlled by diffusion. They also observed enhanced creep when the structure transforms from orthorombic to tetragonal around 1240°C.

Superplastic creep have been observed for fine-grained $BaTiO_3$ between 1150-1250°C[94]. The stress exponent was between 2 and 3 and the activation energy between 800-1200 kJ/mole. Larger grained $BaTiO_3$ deform by a diffusion mechanism with stress exponent close to unity and activation energy ~720 kJ/mole [95].

Creep was measured for $(La,Sr)MnO_3$ as a function of Sr content and oxygen partial pressure at 1300°C by Cook et al. [96]. They found that the rate controlling specie changed from oxygen to cation vacancies as the degree of substitution increased and the oxygen partial pressure decreased. The mechanism for creep was grain boundary sliding and lattice diffusion. Wolfestine et al. [97] studied creep of $La_{0.9}Sr_{0.1}MnO_3$ in the temperature range 1150-1300°C in air. They found a stress exponent close to unity and suggested a Nabarro-Herring diffusional creep mechanism where the creep rate is limited by cation lattice diffusion.

The creep behavior of $SrCo_{0.8}Fe_{0.2}O_{3-x}$ was studied by Majkic et al. [98] in the temperature interval 850-975°C. They concluded that creep was controlled by diffusion of cations, but they could not determine whether it was lattice or grain boundary diffusion. They found an activation energy of 268 kJ/mole below 925°C and 457 kJ/mole above 925°C. The change was attributed to a shift between A and B cation as the rate controlling specie. An alternative explanation could be that the shift in mechanism is related to phase transitions in the material similar to the decomposition of $SrCoO_3$ to $Sr_6Co_5O_{15}$ and Co_3O_4 below 800-900°C [99, 100].

Several studies have been done on the superconducting system $YBa_2Cu_3O_{7-x}$ since deformation can improve the electrical properties. Deformation maps were developed by Jimenez-Melendo et al. [101]. The mechanism for creep was dependent on temperature, stress, and grain size. Superplastic flow have been observed for small grain sizes. Intermediate grain size leads to a grain boundary diffusion controlled mechanism, and larger grains leads to a lattice diffusion controlled mechanism. By increasing the temperature the controlling mechanism changes from grain boundary to lattice diffusion. Y is most probably the rate controlling specie in this system [102].

Also for $BaCe_{1-x}Y_xO_3$, a diffusion controlled creep mechanism was proposed in the temperature range 1200-1450°C [103]. The rate controlling species were Ba or Ce interstitials. The activation energy was around 350 kJ/mole.

2.7 Phase relations

During sintering of ABO_3 perovskites, different secondary phases can appear if the A/B ratio is deviating from unity. It can be demanding to prepare compositions of exact 1:1 ratio between A and B, especially when more elements are introduced by substitution at the A and/or B site. By knowing the phase relations it can be favorable to consciously make compositions with a slight A or B site excess either to avoid formation of specific secondary phases or to take advantage of some properties. The temperature range for sintering might be goverened by the phase relations. With this in mind, an overview of the available pseudo binary phase diagrams of A_2O_3-B_2O_3 (A = La, Sr, Ca; B = transition metal) will give important knowledge of what effect A or B site excess will have on the phase composition.

If only binary oxides are formed a small deviation from A/B=1 will result in only small amounts of secondary phase. However, in many systems ternary oxides with A/B ratio different from unity are stable. A small deviation from stoichiometry in the overall composition can lead to formation of relatively large amounts of secondary phases. This will obviously have an effect on the sintering properties, the microstructure and the functional properties. The introduction of secondary phases can in many cases also be an aid for sintering. In most systems a eutectic melt can be formed giving liquid phase sintering. The liquid phase enhances diffusion and increases the sintering rate. However, the liquid phase may also cause exaggerated grain growth

because it increases the grain boundary mobility. Formation of solid secondary phases also have an effect on sintering. Often precipitation of a secondary phase during sintering decreases the densification rate. However, a small amount of solid secondary phase at the grain boundaries can be favorable because it inhibits grain growth due to decreased grain boundary mobility.

The formation of secondary phases, either solid or liquid, often involves reduction of the transition metal, and oxygen gas may be formed. The effect of oxygen gas evolution on sintering will depend on whether the porosity is open or closed when this process occurs. In the case of closed porosity the evolution of gas will create a pressure inside the pores, and this may lead to swelling. Especially if a liquid phase is present swelling will be fast because of enhanced diffusion and viscous flow. In the case of open porosity the gas evolution will have a smaller effect, but it still may retard densification.

Very few systems exhibit a large region for solid solubility of either A_2O_3 or B_2O_3 in ABO_3. Within the $LaBO_3$ (B = Ti, V, Cr, Mn, Fe, Co, Ni, Cu) series it is only in the $LaMnO_3$ system there has been reported a relatively large tolerance for cation nonstoichiometry without precipitation of secondary phases [67]. Around 900°C in air, the solid solubility limits are at a La/Mn ratio of 0.9 and 1.2. At higher temperatures the range become more symmetrical, and above 1100°C the La/Mn ratio range is between 0.9 and 1.1. Also in the $SrFeO_3$ system solid solubility has been observed.[Paper II] The solid solubility region becomes more narrow with increasing temperature, however the exact limits have not been investigated

On the B-rich side of the La_2O_3-B_2O_3 phase diagram, ternary phases are reported only in the La-Ti-O and La-Fe-O systems. $LaFe_{12}O_{19}$ is stable in the temperature range 1380-1420°C. Above 1420°C $LaFe_{12}O_{19}$ decomposes to Fe_3O_4 and the perovskite phase [108]. In the La-Ti-O system, $La_4Ti_9O_{24}$ is formed in air, but decompose at 1455°C to a liquid phase and the perovskite [112]. At reduced oxygen partial pressure, $La_2Ti_3O_{12}$ crystallizing in the cubic perovskite structure can be prepared.

It is mostly at the La-rich side of the La_2O_3-B_2O_3 phase diagram that phases differing from the binary oxides are formed. A large family of oxides termed the Ruddlesden–Popper (RP) type phases are possible compositions with structure closely related to the perovskite structure [37]. The general formula is $La_{n+1}B_nO_{3n+1}$ (n=1, 2, 3, ..., ∞). La_2BO_4, $La_3B_2O_7$ and $La_4B_3O_{10}$ respectively corresponding to n= 1, 2 and 3 are stable compounds in some of these systems. The stability of the Ruddleden-Popper phases are related to the

oxidation state of the B-cation. The valence state of the transition metal in the ternary oxides $La_{n+1}B_nO_{3n+1}$ increases by increasing value of n. In the ABO_3 perovskite (n=∞) the valence state is B^{3+}, for $La_4B_3O_{10}$ and $La_3B_2O_7$ (n=3, 2) there is a mixed valence of B^{2+} and B^{3+}, and in the last member of the series La_2BO_4 (n=1) the valence state is B^{2+}.

In the La-Cu-O system the only stable ternary phase below 1000°C is the RP type phase La_2CuO_4 (n=1). High pressure synthesis must be applied in order to stabilize the perovskite phase $LaCuO_3$. Two intermediate phases are formed above 1000°C. $La_2Cu_2O_5$ is stable in the temperature region 1002-1035°C, and $La_8Cu_7O_{19}$ is stable in the region 1012-1027°C. La_2CuO_4 is stable up to 1375°C where it decomposes to La_2O_3 and a liquid phase [104].

$LaNiO_3$ decomposes above 1094°C in air and form $La_4Ni_3O_{10}$ and NiO occurs. By further increasing the temperature to around 1196°C lead to decomposition of $La_4Ni_3O_{10}$ into La_2NiO_4 and NiO [105]. The decomposition temperature is higher in oxygen. The existence of the $La_3Ni_2O_7$ phase has also been reported by Seo et al.[106]. This proves the existence of RP type phases with n=1, 2 and 3 in the La-Ni-O system.

In the La-Co-O system $La_4Co_3O_{10}$ is formed around 1450°C in air.[Paper I] This phase is also formed at lower temperatures by reducing the partial pressure of oxygen. La_2CoO_4 is not coexistent with $LaCoO_3$. At low oxygen partial pressure $LaCoO_3$ decomposes to La_2CoO_4 and CoO [107]. Both of these compounds are RP type phases with n=1 and 3. The stability of the RP-type phases in the La-Co-O, La-Ni-O, and La-Cu-O systems reflects the relatively high stability of divalent Co, Ni, and Cu compared to the rest of the first row transition metals.

On the La-rich side of the La-Fe-O system only La_2O_3 is formed in air [108]. The absence of RP-type phases reflects the high stability of Fe^{3+} compared to Fe^{2+}. This is related to the d^5 electron configuration in Fe^{3+} which is energetically favorable. Like in the La-Fe-O system only La_2O_3 is stable in the La-Mn-O system at the La-rich side of the phase diagram [67]. However, by decreasing the partial pressure of oxygen $La_2MnO_{4.15}$ (n=1) is formed at high temperature (above 1380°C in argon).

Further to the left in the row of transition metals the La-rich side of the phase diagram consists of phases obtaining other structures than the RP-type phases. In the La-Cr-O system, three different La-rich phases can form depending on temperature and partial pressure of O_2. Berjoan [109]

investigated the system at 0.83 bar O_2(g) and found that La_2CrO_6 is stable up to 960°C. In the temperature range 870-1080°C $La_{16}Cr_7O_{44}$ is stable, and $La_7Cr_2O_{16}$ is stable in the range 980-1240°C. The stability of these phases is again related to the oxidation state of the transition metal. All three phases contain Cr^{6+} and /or Cr^{5+} which both are stable valence states for Cr. Especially, the Cr^{6+} state is stable due to the d^0 electron configuration. Above 1240°C, only the perovskite phase and La_2O_3 are stable. In argon atmosphere, the system only consists of La_2O_3 and the perovskite.

Below 1800°C in vacuum only V_2O_3 and La_2O_3 are stable phases in addition to the perovskite phase in the La-V-O system. At 1800°C a new phase, $La_4V_2O_9$, is formed which melts at 2190°C [110]. In the La-Ti-O system both La_2TiO_5 and $La_4Ti_3O_{12}$ are stable in air. La_2TiO_5 melts at 1760°C and $La_4Ti_3O_{12}$ decomposes to La_2TiO_5 and $LaTiO_3$ at 1450°C. None of these compounds are RP type phases. The structure of $La_4Ti_3O_{12}$ is related to the perovskite structure while the structure of La_2TiO_5 is not. The oxidation state of titanium is Ti^{4+} in both phases and the electron configuration is d^0 [111, 112].

In most systems, a eutectic melt is formed on both sides of the La/B ratio of unity. Generally, the eutectic temperatures are higher at the La-rich side than the B-rich side except for the La-Cr-O system. However, the eutectics are above 1400°C in all systems except for the La-Cu-O system where T=1025°C at the B-rich side. This implies that it should be possible to avoid formation of liquid phase by keeping the sintering temperature below 1400°C. To obtain high density materials below this temperature, a powder with small grain size is often demanded. By modern powder preparation techniques this is possible to achieve.

In most systems, substitution at the A and/or B site is required to obtain the desired functional properties. Often Sr or Ca is substituted on the A site for La. In case of a deviation from exact cation stoichiometry, the phase relations in the SrO/CaO-B_2O_3 systems will be important. Quite a few phases are formed in these systems, and only the cobalt and iron systems will be discussed here.

In the SrO-Fe_2O_3 system, $Sr_3Fe_2O_7$ is formed at the Sr-rich side of the phase diagram [113]. There is a eutectic point at ~1500°C. At the Fe-rich side, $Sr_4Fe_6O_{13}$ is stable from ~775°C up to ~1295°C where it decomposes to the perovskite $SrFeO_{3-\delta}$ and a liquid phase. $SrFe_{12}O_{19}$ is formed at higher Fe-contents and it is stable up to ~1435°C. A eutectic melt is formed between

these compositions at ~1195°C. Only CaO and $CaFeO_{3-\delta}$ are stable on the Ca-rich side of the CaO-Fe_2O_3 phase diagram. At the Fe-rich side, $CaFe_2O_4$ is stable up to 1216°C where it decomposes to a melt and $CaFeO_3$. $CaFe_4O_7$ is stable in the temperature interval 1155-1226°C. A eutectic melt is formed between these compositions at 1205°C [114].

The CaO-Co_2O_3 system is different [80]. The 1:1 perovskite phase is not stable in this system, and ternary oxides are only stable below 1026°C. $Ca_3Co_2O_6$ and $Ca_3Co_4O_9$ are stable up to 1026°C and 926°C, respectively. Above 1026°C only CaO and CoO are present. At 1350°C a eutectic melt is formed at ~70 wt% CoO. In the SrO-Co_2O_3 system the brownmillerite phase $SrCoO_{2.5\pm\delta}$ is stable above ~900°C while the perovskite structure is stabilized at higher oxygen partial pressures. Below 900°C $SrCoO_{2.5\pm\delta}$ decomposes to $Sr_5Co_6O_{15}$ and CoO [99, 100]. $Sr_3Co_2O_7$ is also a stable compound at the Sr-rich side of the system [115]. Melting temperatures have not been reported in this system.

Generally, when Sr or Ca are introduced into the iron or cobalt system melts can be formed at lower temperatures than in the corresponding La_2O_3-Co_2O_3 and La_2O_3-Fe_2O_3 systems. The lowest melting phase is formed at the Fe or Co-rich side of the phase diagrams as low as ~1195°C. Also in the SrO/CaO-B_2O_3 (B = Mn, Cr, Ti) eutectic melts are formed at lower temperatures compared to in the La_2O_3-B_2O_3 systems. If the perovskite is substituted both at the A and B site the phase relations become even more complicated, and melts may be formed at even lower temperatures due to melting point depletion.

3 REFERENCES

1 Minh, N.Q., "Ceramic fuel cells", *J. Am. Ceram. Soc.,* **76** [3] (1993) 563-88.

2 Anderson, H., "Review of p-type doped perovskite materials for SOFC and other applications", *Solid State Ionics*, **52** (1992) 33-41.

3 van Roosmalen, J.A.M., "Electrical conductivity in $La_{1-x}Sr_xMnO_{3+\delta}$", *Solid State Ionics*, **66** (1993) 279-84.

4 Petrov, A.N., Cherepanov, V.A., Kononchuk, O.F., and Gavrilova, L.YA, "Oxygen nonstoichiometry of $La_{1-x}Sr_xCoO_{3-\delta}$ ($0<x\leq0.6$)", *J. Solid State Chem.,* **87** (1990) 69-76.

5 Yasuda, Y. and Hishinuma, M., "Electrical conductivity and chemical diffusion coefficient of Sr-doped lanthanum chromites", *Solid State Iooics*, **80** (1995) 141-50.

6 Kawada, T., Horita, T., Sakai, N., Yokokawa, H., and Dokiya, M., "Experimental determination of oxygen permeation flux through bulk and grain boundary of $La_{0.7}Ca_{0.3}CrO_3$", *Solid State Ionics*, **79** (1995) 201-7.

7 Stevenson, J.W., Armstrong, T.R., Pederson, L.R., Li, J., Lewinsohn, C.A., and Baskaran, S., "Effect of A-site cation nonstoichiometry on the properties of doped lanthanum gallate", *Solid State Ionics*, **113-115** (1998) 571-83.

8 Goodenough, J.B., "Ceramic solid electrolytes", *Solid State Ionics*, **94** (1997) 17-25.

9 Tilset, B.G., Fjellvåg, H., Kjekshus, A., Slagtern, Å., and Dahl, I., "Properties of $LaCo_{1-t}Cr_tO$. III. Catalytic activity for CO oxidation", *Appl. Catal. A*, **147** (1996) 189-205.

10 Lindstedt, A., Strömberg, D., and Milh, M.A., "High-temperature catalytic

reduction of nitrogen monoxide by carbon monoxide and hydrogen over $La_{1-x}Sr_xMO_3$ perovskites (M=Fe, Co) during reducing and oxidising conditions", *Appl. Cat. A*, **116** (1994) 109-126.

11 Wachowski, L., "The activity of $LaMeO_3$ oxides obtaied by various methods for catalytic oxidation of CO and 1-butene", *Z. Phys. Chemie (Leipzig)*, **269** (1988) 743-52.

12 Tascón, J.M.D., and Teyuca, L.G., "Catalytic activity of perovskite-type oxides $LaMeO_3$", *React. Kinet. Catal. Lett.*, **15** [2] (1980) 185-91.

13 Isupova, L.A., Sadykov, V.A., Tsybulya, S.V., Kryukova, G.N., Ivanov, V.P., Petrov, A.N., and Kononchuk, O.F., "Effect of structural disorder on the catalytic activity of mixed La-Sr-Co-Fe-O perovskites", *React. Kinet. Catal. Lett.*, **62** [1] (1997) 129-35.

14 Post, M.L., Sanders, B.W., and Kennepohl, P., "Thin films of non-stoichiometric perovskites as potential oxygen sensors", *Sensors and Actuators B*, **13-14** (1993) 272-75.
15 Kharton, V.V., Naumovich, E.N., and Nicolaev, A.V., "Materials for high-temperature electrochamical oxygen membranes", *J. Membr. Sci*., **111** (1996) 149-57.

16 Li, S., Jin, W., Xu, N., Shi, J., and Lin, Y.S., "Tubular lanthanum cobaltite perovskite type membrane for oxygen permeation", *J. Membr. Sci.*, **166** (2000) 51-61.

17 Balachandran, U., Dusek, J.T., Mieville, R.L., Poeppel, R.B., Kleefisch, M.S., Pei, S., Kobylinski, T.P., Udovich, C.A., and Bose, A.C., "Dense cermaic membranes for partial oxidation of methane to syngas", *Appl. Catal. A*, **133** (1995) 19-29.

18 Takeda, Y., Kanno, K., Takada, T., Yamamoto, O., Takano, M., Nakayama, N. and Bando, Y., "Phase relation in the oxygen nonstoichiometric system $SrFeO_x$ ($2.5 \leq x \leq 3.0$)", *J. Solid State Chem*., **63** (1986) 237-49.

19 Mizusaki, J., Okayasu, M., Yamauchi, S., and Fueki, K., "Nonstoichiometry and phase relationship of the $SrFeO_{2.5}$-$SrFeO_3$ system at high temperature", *J. Solid State Chem*., **99** (1992) 166-72.

20 Vashuk, V.V., Kokhanovskii, L.V., and Yushevich, "Electrical conductivity and oxygen stoichiometry of $SrFeO_{3-\delta}$)", *Inorg. Mater.*, **36** [1] (2000) 79-83.

21 Richerson, D.W., "Modern ceramic engineering", 2. ed, Marcel Dekker, Inc., New York, 1992.
22 German, R.M., "Sintering theory and practice", John Wiley & Sons, Inc., New York, 1996.
23 McColm, I.J. and Clark, N.J., "Forming, shaping, and working of high.performance ceramics", Blackie, Glasgow, 1988.
24 Wachtman, J.B., "Mechanical properties of ceramics", John Wiley & Sons, Inc., New York, 1996.
25 Goldschmidt, V.M., *Skr. Nor. Vidensk.-Akad. [Kl] 1: Mat.-Naturvidensk. Kl No. 2* (1926).
26 Glazer, A.M., "Simple ways of determining perovskite structures", *Acta. Cryst.* **A 31** (1975) 756-62.
27 Rao, C.N.R. and Gopalakrishnan, J., "New directions in solid state chemistry", 2. ed., Cambridge University Press, Cambridge, 1997.
28 Grenier, J.C., Pouchard, M., and Hagenmuller P., "Vacancy ordering in oxygen-deficient perovskite related ferrites", *Structure and Bonding*, **47** (1981) 1-25.
29 Poppelmeier, K.R., Leonowicz, M.E., Scandlon, J.C., Longo, J.M., and Yelon, W.B., "Structure determination of $CaMnO_3$ and $CaMnO_{2.5}$ by X-ray and neutron methods", *J. Solid State Chem.*, **45** (1982) 71-79.
30 Vidyasagar, K., Ganapathi, L., Gopalakrisnan, J., and Rao, C.N.R., "Novel oxygen vacancy-ordered phases of $Ca_2Fe_{2-x}Mn_xO_5$ prepared by topotactic reduction of the perovskite oxides, $Ca_3Fe_{3-x}Mn_xO_{9-y}$ ($0<y<1.5$)", *J. Chem. Soc., Chem. Comm.* (1986) 449-51.
31 Thornton, G., Tofield, B.C., and Hewat, A.W., "A neutron diffraction study of $LaCoO_3$ in the temperature range $4.2<T<1248$ K", *J. Solid State Chem.*, **61** (1986) 301-7.

32 Mizusaki, J., Tabuchi, J., Matsuura, T., Yamauchi, S., and Fueki, K., "Electrical conductivity and seebeck coefficient of nonstoichiometric $La_{1-x}Sr_xCoO_{3-\delta}$", *J. Electrochem. Soc.*, **136** [7] (1989) 2082-88.

33 Mineshige, A., Inaba, M., Yao, T., Ogumi, Z., Kikuchi, K.,and Kawase, M., "Crystal structure and metal-insulator transition and of $La_{1-x}Sr_xCoO_3$", *J.*

Solid State Chem., **121** (1996) 423-29.

34 Grenier, J.-C, Ea, N., Pochard, M., and Hagenmuller, P., "Structual transitions at high temperature in $Sr_2Fe_2O_5$", *J. Solid State Chem.*, **58** (1985) 243-52.

35 Holt, A, Glenne, R., and Norby, T., "Defects and transport in $SrFe_{1-x}Co_xO_{3-\delta}$", *Ionics*, **5** (1999) 434-43.

36 Kokhanovskii, L.V., Vashuk, V.V., Villkotskaya, E.F., Vitushko, S.I., and Zinkevich, M.V., "Synthesis, structure and some physiochemical properties of $SrCo_{1-x}Fe_xO_{3-\delta}$," *Inorg. Mater.*, **35** (1999) 262-86.
37 Ruddlesden, S.N. and Popper, P., "The compound $Sr_3Ti_2O_7$ and its structure", *Acta Cryst.*. **11** (1958) 54.

38 Prasanna, T.R.S. and Navrotsky, A., "Energetics of $La_{2-x}Sr_xCoO_{4-y}$ ($0.5<y<1.5$)", *J. Solid State Chem.*, **112** (1994) 192-95.

39 Hansteen, O.H. and Fjellvåg, H., "Synthesis, crystal structure, and magnetic properties of $La_4Co_3O_{10}$ ($0.00<x<0.3$)", *J. Solid State Chem.*, **141** (1998) 212-20.

40 Sarma, D.D., Shanthi, N., and Mahadevan, P., "Electronic structure and the metal-insulator transition in $LnNiO_3$ (Ln = La, Pr, Nd, Sm, and Ho): band structure results", *J. Phys.:Condens. Matter*, **6** (1994) 10467-74
41 Petrov, A.N., Kononchuk, O.F., Andreev, A.V., Cherepanov, V.A., and Kofstad, P., "Crystal structure, electrical and magnetical properties of $La_{1-x}Sr_xCoO_{3-y}$", *Soilid State Ionics*, **80** (1995) 189-99.
42 Thornton, G., Tofield, B.C., and Williams, D.E., "Spin state equilibria and the semiconductor to metal transition of $LaCoO_3$", *Solid State Comm.*, **44** [8] (1982) 1213-16.
43 Mizusaki, J., Sasmoto, T., Cannon, W.R., and Bowen, H.K., "Electronic conductivity, Seebeck coefficient, and defect structure of $LaFeO_3$", *J. Amer. Ceram. Soc.*, **65** [8] (1982) 363-68.
44 Eibschütz, Shtrikman, S., and Treves, D., "Mössbauer studies of Fe^{57} in orthoferrites", *Phys. Rev.*, **156** [2] (1966) 562-77.
45 Goodenough, J.B., *Progr. Solid State Chem.*, **5** (1971) 149.
46 Mineshige, A., Kobune, M., Fujii, S., Ogumi, Z., Inaba, M., Yao, T., and Kikuchi, K., "Metal-insulator transition and crystal structure of $La_{1-x}Sr_xCoO_3$ as functions of Sr-content, temperature, and oxygen partial pressure", *J. Solid*

State Chem., **142** (1999) 374-81.

47 Smyth, D.M., Chang, E.K., nad Liu, D.H., "Travels through perovskite space", *Phase Transitions*, **58** [1-3] (1996) 57-73.
48 Mizusaki, J., Tagawa, H., Naraya, K., and Sasamoto, T., "Nonstoichiometry and thermochemical stability of the perovskite-type $La_{1-x}Sr_xMnO_{3-\delta}$", *Solid State Ionics*, **49** (1991) 111-18.
49 Kruidhof, H., Bouwmeester, H.J.M., v. Doorn, R.H.E., and Burgrgaaf, A.J., "Influence of order-disorder transitions on oxygen permeability through selected nonstoichiometric oxides", *Solid State Ionics*, **63-65** (1993) 816-22.

50 Kendall, K.R., Navas, C., Thomas, J.K., and zur Loye, H.-C., "Recent developments in perovskite-based oxide ion conductors", *Solid State Ionics*, **82** (1995) 215-23.

51 Anderson, H.U., "Influence of Ba/Ti ratio on the initial sintering kinetics of $BaTiO_3$", J. *Am. Ceram. Soc*., **56** (1973) 605-6.

52 O'Bryan, H.M.JR. and Thompson, J.JR., "Phase equilibria in the TiO_2-rich region of the system BaO-TiO_2", *J. Am. Ceram. Soc*., **57** (1974) 522-26.

53 Demartin, M., Hérard, C., Carry, C., and Lemaître, J., "Dedensification and anomalous grain growth during sintering of undoped barium titanate", *J. Am. Ceram. Soc*., **80** (1997) 1079-84.
54 Fujimoto, M. and Kingery, D., "Microstructures of $SrTiO_3$ internal boundary layer capacitors during and after processing and resultant electrical properties", *J. Am. Ceram. Soc*., **68** [4] (1985) 169-73.
55 Cheng, S.-Y., Fu, S.-L., and Wei, C.-C., "Sintering of $SrTiO_3$ with Li_2CO_3 addition", *Ceram. Int.*, **15** (1989) 231-36.
56 Chen, Y.-S., Young, R.-J., and Wu, T.-B., "Densification and microstructural development of $SrTiO_3$ sintered with V_2O_5", *J. Am. Ceram. Soc*., **70** [10] (1987) C-260-64.
57 Yokokava, H., Sakai, N., Kawada, T., and Dokiya, M., "Chemical thermodynamic considerations in sintering of $LaCrO_3$-based perovskites", *J. Electrochem. Soc*., **138** (1991) 1018-27.

58 Mori, M., Hiei, Y., and Sammes, N.M., "Sintering behavior and mechanism of Sr-doped lanthanum chromites with A site excess composition in air", *Solid State Ionics*, **123** (1999)103-11.

59 Chick, L.A., Liu, J., Stevenson, J.W., Armstrong, T.R., McReady, D.E., Maupin, G.D., Coffey, G.W., and Coyle, C.A., "Phase stability and transient liquid-phase sintering in calcium-substituted lanthanum chromite", *J. Am. Ceram. Soc.*, **80** [8] (1997) 2109-20.

60 Kaiser, A., Sommer, B., and Woermann, E., "The system CaO-"$CaCr_2O_4$"-$CaAl_2O_4$ in air under mildly reducing conditions", *J. Am. Ceram. Soc.*, **75** [6] (1992) 1463-71.

61 Groupp, L. and Anderson, H., "Desnification of $La_{1-x}Sr_xCrO_3$", *J. Am. Ceram. Soc.*, **59** [9-10] (1976) 449-50.

62. Bansal, K.P., Kumari, S., Das, B.K., and Jain, G.C., "On the sintering and dielectric properties of ceramic $La_{0.96}Sr_{0.04}CrO_3$", *Trans. J. Br. Ceram. Trans.*, **80** (1981) 215-19.

63 Bates, L.J., Chick, L.A., and Weber, W.J., "Synthesis, air sintering and properties of lanthanum and yttrium chromites and manganites", *Solid State Ionics*, **52** (1992) 235-42.

64 Hayashi, S., Fukaya, K., and Saito, H., "Sintering of lanthanum doped with zinc or copper", *J. Mater. Sci. Lett.*, **7** (1988) 457-58.

65 Jin, F., Endo, T., Takizawa, H., and Shimada, M., "Effects of divalent substitution on sinterability and electrical properties of $LaCrO_3$ ceramics", *J. Solid State Chem.*, **113** (1994) 138-44.

66 Koc, R. and Anderson, H.U., "Liquid phase sintering of $LaCrO_3$, *J. Eur. Ceram. Soc.*, **9** (1992) 285-92.66

67 van Roosmalen, J.A.M., van Vlaanderen, and P. Cordfunke, E.H.P., "Phases in the perovskite-type $LaMnO_{3+\delta}$ solid solution and the La_2O_3-Mn_2O_3 phase diagram", *J. Solid State Chem.*, **114** (1995) 516-23.

68 van Roosmalen, J.A.M., Cordfunke, E.H.P., and Huijsmans, J-P-P, "Sinter behavior of (La, Sr)MnO_3", *Solid State Ionics*, **66** (1993) 285-93.

69 Chakraborty, A. and Maiti, H.S., "Bi_2O_3 as an effective sintering aid for La(Sr)MnO_3 powder prepared by autoignition route", *Ceram. Int.* **25** (1995) 115-23.

70 Stevenson, J.W., Hallman, P.F., Armstrong, T.R., and Chick, L., "Sintering behavior of doped lanthanum and yttrium manganite", *J .Am.*

Ceram. Soc. **78** (1995) 507-12.

71 Poirson, A., Decorse, P., Caboche, G., and Dufour, L.C., "A dilatometric study of the $La_{0.8}Sr_{0.2}MnO_3$ sintering behaviour", *Solid State Ionics,* **99** (1997) 287-95.
72 Evju, C., "Sintring av kalsium og strontium dopet lantanmanganitt", Diploma thesis, Department of Inorganic Chemistry, NTNU, 1996.
73 Watterud, G., "Sintring av keramiske materialer aktuelle som oksygen permeable mebraner", Diploma thesis, Department of Inorganic Chemistry, NTNU, 1997.
74 Sagdahl, L., Einarsrud, M.-A., and Grande, T., "Sintering of *LaFeO3 cera*mics", J. Am. Ceram. Soc. Comm., Submitted.

75 Sagdahl, L., Einarsrud, M.-A., and Grande, T., Unpublished.
76 C.-J. Tsai, Dixon, A.G., Ma, Y.H., Moser, W.R., and Pascucci, M.R., "Dense perovskite, $La_{1-x}A'_xFe_{1-y}Co_yO_{3-\delta}$ (A'=Ba, Sr, Ca), membrane synthesis, applications, and characterization", *J. Am. Ceram. Soc.,* **81** (1998) 1437-44

77 Kharton, V.V, Tikhonovich, V.N., Shuangbao,L., Naumovich, E.N., Kovalevsky, A.V., and Viskup, A.P., "Ceramic microstructure and oxygen permeability of $SrCo(Fe,M)O_{3-\delta}$ (M = Cu or Cr) perovskite membranes," *J. Electrochem. Soc.*, **145** (1998) 1363-73.

78 Kharton, V.V., Naumovich, E.N., Nikolaev, A.V., Astashko, V.V., and Vecher, A.A., "Electrochemical properties of mixed $SrCo(Fe,Cu)O_{3-\delta}$ conductors," *Russ. J. Electrochem.*, **29** (1993) 1201-09.

79 Coutures, J.-P., Badie, J.M., Berjoan, R., Coutures, J., Flamend, R., and Rouanet, A., "Stability and thermodynamic properties of rare earth perovskites", *High Temp. Sci*., **13** (1980) 331-36.

80 Wuermann, E. and Muan, A., "Phase equilibria in the system CaO-cobalt oxide in air", *J. Inrg. Nucl. Chem.*, **32** (1970) 1455-59.
81 Denos, Y., Morin, F., and Trudel, G., "Characterisation of pure and strontium-substituted lathanum cobaltites synthesised by the glycine-nitrate process", *Proc.-Electrochem. Soc.,* **93/94** (1993) 231-40.

82 van Doorn, R.H.E., Kruidhof, H., Nijmeijer, A., Winnubst, L., and Burggraaf, A.J., "Preparation of $La_{0.3}Sr_{0.7}CoO_{3-\delta}$ perovskite by thermal

decomposition of metal-EDTA complexes", *J. Mater. Chem.*, **8** (1998) 2109-12.
83 Blamey, J.M. and Parry, T.V., "the effect of processing variables on the mechanical and electrical properties of barium titanate positive-temperature-coefficient-of-resistance ceramics", *J. Mater. Sci.*, **28** (1993) 4317-24.
84 Cheng, B.L., Gabbay, M., Duffy, W., and Fantozzy, G., "Mechanical loss and Youn's modulus associated with phase transitions in barium titanate based ceramics", ", *J. Mater. Sci.*, **31** (1996) 4951-55.
85 Sammes, N.M., Rataraj, R., "The effect of sintering on the mechanical properties of SOFC ceramic interconnect materials", *J. Mater. Sci.*, **29** (1994) 4319-24.
86 Sammes, N.M., Rataraj, R., "High-temperature mechanical properties of $La_{0.7}Sr_{0.3}Cr_{1-y}Co_yO_3$ in reducing environments", *J. Mater. Sci.*, **32** (1997) 687-92.
87 Paulik, S.W., Baskaran, S., and Armstrong, T.R., "Mechanical properties of calcium- and strontium-substituted lanthanum chromite", *J. Mater. Sci.*, **33** (1998) 2397-404.
88 Montross, C.S., Yokokawa, H., Dokiya, M., and Bekessy, L., "Mechanical properties of magnesia-doped lanthanum chromite versus temperature", *J. Am. Ceram. Soc.*, **78** [7] (1995) 1869-72.
89 D'Souza, C.M. and Sammes, N.M., "Mechanical properties of strontum doped lathanum manganite", *J. Am. Ceram. Soc.*, **83** [1] (2000) 47-52.
90 Drennan, J., Zelizko, V., Hay, D., Ciacchi, F.T., Rajendran, S., and Badwal, S.P.S, "Characterisation, conductivity and mechanical properties of the oxygen-ion conductor $La_{0.9}Sr_{0.1}Ga_{0.8}Mg_{0.2}O_{3-x}$", *J. Mater. Chem.*, **7** [1] (1997) 79-83.
91 Baskaran, S., Lewinsohn, C.A., Chou, Y-S., Quian, M., Stevenson, J.W., and Armstrong, T.R., "Mechanical properties of alkaline earth-doped lathanum gallate", *J. Mater. Sci.*, **34** (1999) 3913-22.
92 Sammes, N.M., Keppeler, F.M., Näfe, H., and Aldinger, F., "Mechanical properties of solid-state-synthesized strontium- and magnesium-doped lanthanum gallate", *J. Am. Ceram. Soc.*, **81** [12] (1998) 3104-108.
93 Karato, S.-I. and Li, P., "Diffusion creep in perovskite: Implications for the rheology of the lower mantle", *Science*, **255** (1992) 1238-40.
94 Carry, C. and Mocellin, A., "Superplastic creep of fine-grained $BaTiO_3$ in a reducing environment", *J. AM. Ceram. Soc.*, **69** [9] (1986) C-215-16.
95 Park. E.T., Nash, P., Wolfestine, J., Goretta, K.C., and Routbort, J.L., "High temperature creep of polycrystalline $BaTiO_3$", *J. Mater. Res.*, **14** [2] (1999) 523-28.
96 Cook, R.E., Goretta, K.C., Wolfestine, J., Nash, P., and Routbort, J.L.,

"High-temperature deformation and defect chemsitry of $(La_{1-x}Sr_x)_{1-y}MnO_{3+\delta}$", *Acta Mater.*, **47** [10] (1999) 2969-80.
97 Wolfestine, J., Armstrong, T.R., Weber, W.J., Boling-Risser, M.A., Goretta, K.C., and Routbort, J.L., "Elevated temperature deformation of fine-grained $La_{0.9}Sr_{0.1}MnO_3$", *J. Mater. Res.*, **11** [3] (1996) 657-62.
98 Majkic, G., Wheeler, L., and Salama, K., "Characterization of creep behavior of $SrCo_{0.8}Fe_{0.2}O_{3-x}$", *Mat. Res., Symp., Proc.*, **575** (2000) 349-54.
99 Takeda, Y., Kanno, R., Yamamoto, O., Takano, M., and Bando, Y., "Phase relation and oxygen-non-stoichiometry of perovskite-like compound $SrCoO_x$ (2.29<x<2.80)", *Z. Anorg. Allg. Chem.*, **540/541** (1986) 259-70
100 Harrison, W.T.A., Hegwood, S.L., and Jacobson, A.J., "A powder neutron diffraction determination of the structure of $Sr_6Co_5O_{15}$, formerly described as the low-temperature hexagonal form of $SrCoO_{3-x}$", *J. Chem. Soc. Chem. Comm.*, (1995) 1953-54
101 Jiménez-Melendo, M., Dominguez-Rodriguez, A., and Routbort, J.L., "Deformation maps of $YBa_2Cu_3O_{7-x}$ superconductors", *Scripta Metall.*, **32** [4] (1995) 621-26.
102 Routbort, J.L., Goretta, K.C., Cook, R.E., and Wolfestine, J., "Deformation of perovskite electronic ceramics – a review", *Solid State Ionics*, **129** (2000) 53-62.
103 Park, E.T., Goretta, K.C., de Arellano-López, A.R., Guan, J., Balachandran, U., Dorris, S.E., and Routbort, J.L., "High temperature deformation of $BaCe_{1-x}Y_xO_{3-y}$", *Solid State Ionics*, **117** (1999) 323-30.
104 Skakle, J.M.S. and West, A.R., "Subsolidus relations in the La_2O_3-CuO-CaO phase diagram and the La_2O_3-CuO binary join", *J. Am. Ceram. Soc.*, **77** [8] (1994) 2199-202.
105 Höfer, H.E. and Kock, W.F., "Crystal chemsitry and thermal behavior in the $La(Cr,Ni)O_3$ perovskite system", *J. Electrochem. Soc.*, **140** [10] (1993) 2889-94.
106 Seo, D.-K., Liang, W., Whanbo, M.-H., Zhang, Z., and Greenblatt, M., "Electronic band structure and madelung potential study of the nickelates La_2NiO_4, $La_3Ni_2O_7$, and $La_4Ni_3O_{10}$", *Inorg. Chem.*, **35** (1996) 6396-6400.
107 Seppänen, M., Kytö, M., and Taskinen, P., "Stability of the ternary phases in the La-Co-O system", *Scand. J. Met.*, **8** (1979) 199-204.
108 Moruzzi, V.L. and Shafer, M.W., "Phase equilibria in the system La_2O_3-iron oxide in air", *J. Am. Ceram. Soc.*, **43** [7] (1960) 367-72.
109 Berjoan, R., "Contribution a l'étude des réactions de l'oxygène avec les mélanges d'oxyde de lanthane et d'oxyde de chrome III ou de chromite de lanthane", *Rev. Int. Htes. Temp. et Réfract.*, **13** (1976) 119-35.
110 Molodkin, A.K., Belan, V.N., Bogatov, Y.E., and Moskalenko, V.I.,

"Phase diagram of the lanthanum oxide-vanadium(III) oxide system", *Russ. J. Iorg. Chem.*, **27** [4] (1982) 581-83.

111 Fedorov, N.F., Melnikova, O.V., Saltykova, V.A., and Chistyakova, M.V., "New perovskite compound (12H) $La_4Ti_3O_{12}$", *Russ. J. Inorg. Chem.*, **24** [5] (1979) 649-51.

112 MacChesney, J.B. and Sauer, J., "System La_2O_3-TiO_2; phase equilibriums and electrical properties", *J. Am. Ceram. Soc.*, **45** [9] (1962) 419.

113 Batti, P., "Diagramma d'equilibrio del sistema SrO-Fe_2O_3", *Ann. Chim. (Rome)*, **52** (1962) 941-61.

114 Phillips, B. and Muan, A., "Phase equilibria in the system CaO-iron oxide in air and 1 atm O_2 pressure", *J. Am. Ceram. Soc.*, **41** [11] (1958) 445-54.

115 Dann, S.E. and Weller, M.T., "Structure and oxygen stoichiometry in $Sr_3Co_2O_{7-y}$ ($0.94<y<1.22$)", *J. Solid State Chem.*, **115** (1995) 499-507.

Paper 1

Journal of the European Ceramic Society 20 (2000) 185–193

Sintering of $LaCoO_3$ based ceramics

K. Kleveland, M.-A. Einarsrud, T. Grande*

Department of Chemistry, Norwegian University of Science and Technology, 7491 Trondheim, Norway

Received 18 January 1999; received in revised form 22 April 1999; accepted 11 May 1999

Abstract

The densification, microstructure and phase evolution of near stoichiometric, Co-excess and Co-deficient perovskite $La_{1-x}M_xCoO_{3-\delta}$ (M = Ca, Sr; $x = 0$, 0.2) powders have been investigated by electron microscopy and powder X-ray diffraction. Sub-micron powders were prepared from nitrate precursors using the glycin-nitrate and the EDTA methods. The sintering temperature was observed to decrease with Ca or Sr substitution. Dense materials with grain size in the order of 3–5 μm have been obtained at 1200°C for near stoichiometric powders. Considerable grain growth was observed at higher sintering temperatures. The presence of other crystalline phases in addition to the perovskite due to Co-excess/-deficiency considerably affects the microstructure and acts as grain growth inhibitors by grain boundary pinning. The volume fraction of secondary phases is particularly large in the case of Co-deficient $LaCoO_3$ due to the formation of $La_4Co_3O_{10}$. In non-stoichiometric $La_{0.8}Ca_{0.2}CoO_3$, a liquid phase consisting mainly of CaO and CoO was observed at 1400°C causing exaggerated grain growth. Considerable pore coarsening was observed in Co-excess $La_{0.8}Ca_{0.2}CoO_3$ at 1350°C. The present investigation demonstrates the importance of controlling the stoichiometry of $LaCoO_3$ based ceramics in order to obtain dense materials with well defined microstructure.

Keywords: Grain growth; $LaCoO_3$; Microstructure-final; Perovskites; Sintering

1. Introduction

Mixed ionic and electronic conducting perovskites $La_{1-x}M_xCoO_{3-\delta}$ (M = Ca, Sr) have potential application as materials for oxygen permeable membranes, electrodes, oxidation catalysts and oxygen sensors.[1–6] In order to achieve the functional properties required for an oxygen permeable membrane, dense materials with well defined microstructure is desired. In most cases the presence of secondary phases will decline the functional properties of the membrane, and therefore single phase materials are preferred. The mechanical properties might also be critical if oxygen is produced by applying a pressure gradient over the membrane or if thin membranes are desired in order to achieve sufficient oxygen flux. The purpose of this study was to investigate the sintering behaviour of $LaCoO_3$ based ceramics. The effect of substitution and cation stoichiometry on the sintering properties has been investigated in the temperature interval 1050–1450°C.

Sintering of $LaCoO_3$ based ceramics has not been investigated thoroughly. Koc et al.[7] investigated the sintering behaviour of $La_{1-x}Ca_xCr_{1-y}Co_yO_3$, and they obtained a maximum density of 95% of theoretical density for both $LaCoO_3$ and $La_{0.7}Ca_{0.3}CoO_3$. Decreased sintering temperature by substitution of Ca was reported. Denos et al.[8] investigated the relationship between green and fired densities for $LaCoO_3$ and $La_{0.5}Sr_{0.5}CoO_3$. Higher densities were reported for $LaCoO_3$ than for the strontium substituted $LaCoO_3$.

Phase equilibrium in the La–Co–O system in the temperature interval 800–1200°C has been studied by several authors.[9–13] Stable ternary oxides observed in the system are $LaCoO_3$, La_2CoO_4 and $La_4Co_3O_{10}$. $LaCoO_3$ decomposes to CoO and $La_4Co_3O_{10}$ at low oxygen partial pressures. There are conflicting reports on the solid solution of La_2O_3 or CoO in $LaCoO_3$. Morin et al.[14] report the presence of secondary phases at more than 0.3% deviation from the A/B ratio in the ideal perovskite (ABO_3). Seppänen et al.[12] claim a stability range for $LaCoO_{3-\vartheta}$ within ±1%. Munakata et al.[15] have however reported preparation of single phase $La_{0.9}CoO_3$. Since a small tolerance in A/B ratio is

* Corresponding author.
E-mail addresses: tor.grande@chembio.ntnu.no (T. Grande).

0955-2219/00/$ - see front matter
PII: S0955-2219(99)00141-7

reported in most cases, secondary phases might be difficult to avoid in the preparation of $LaCoO_3$ based ceramics. In this paper the cation stoichiometry has been varied between Co-excess and Co-deficiency in order to investigate the effect of secondary phases on the sintering behaviour.

2. Experimental

Pure $LaCoO_3$ and Sr or Ca substituted $LaCoO_3$ powders, $La_{1-x}M_xCoO_{3-\partial}$ (M = Ca, Sr; $x = 0$, 0.2), were prepared by the glycine nitrate method (G/N) described by Chick et al.[16] and the EDTA-method described here. Samples prepared from the two methods are termed G/N-samples and EDTA-samples, respectively. In addition to the near stoichiometric powders, 5 mol% Co-excess and 10 mol% Co-deficient powders were prepared. For convenience, in the following the compositions $La_{0.8}Ca_{0.2}CoO_3$ and $La_{0.8}Sr_{0.2}CoO_3$ are termed 20%Ca and 20%Sr, respectively.

Approximately 1 M solutions of the nitrate salts were used and the concentration of the solutions was measured by an Atom Scan 16 1CP-AES Spectrometer (ICP) (Thermo Jarrell Ash Corp.). In case of the G/N-method approximately 25 ml of the glycine-nitrate solution was transferred to a quartz container and then heated on a hot plate until ignition. The EDTA-powders were prepared by mixing either 1 M nitrate solutions or weighted amounts of nitrate salts, EDTA and water to a total volume of about 400 ml. The stoichiometry of the nitrate salts was determined by thermogravimetrical analysis. pH was adjusted to 9–10 with NH_4OH solution to prevent precipitation. The solution was transferred to a beaker on a hot plate, and heated at 80°C until gel formation. The gel was dried in air at 200–240°C for 24 h, and organic residue was burnt off at 600°C for 24 h.

The powders were ball milled (Si_3N_4-balls) for 4 h in 100% ethanol. The milled powders were further calcined at 900–1000°C for 8–72 h in flowing synthetic air and further ball milled for 24 h. Powder pellets (0.7 g) were uniaxially pressed (double action) at 230 MPa for GLN-powders and 70–100 MPa for EDTA-powders. The relative green density obtained was 50–55% of theoretical density.

The chemical composition of the powders was measured by ICP and is given in Table 1. X-ray powder diffraction (XRD) of powders and crushed sintered samples was performed on a Siemens D5005 diffractometer (CuK_α radiation and a secondary monochromator) in the 2θ range 20–65° with step 0.040° and step time 9.0 s. Cell parameters and crystallographic densities were calculated using the programs Profile, WinIndex and Metric. Si (20 wt%) was added the powders as an internal standard.

Table 1
Cation stoichiometry (±2%) relative to Co of the different powders

Sample composition	La	Sr	Ca	Co
EDTA-samples				
Stoichiometric				
$LaCoO_3$	1.02			1.00
20%Sr	0.80	0.204		1.00
20%Ca	0.80		0.213	1.00
Co-deficient				
$LaCoO_3$	1.12			1.00
20%Sr	0.88	0.223		1.00
20%Ca	0.87		0.205	1.00
Co-excess				
$LaCoO_3$	0.95			1.00
G/N-samples				
Stoichiometric				
$LaCoO_3$	1.01			1.00
20%Sr	0.79	0.198		1.00
20%Ca	0.80		0.207	1.00

The surface area of the powders was measured by the BET method (ASAP 2000, Micromeritics). The surface area of the G/N-powders was in the range 1.6–2.2 m^2/g, and the corresponding calculated particle size is 0.4–0.5 μm assuming spherical particles. SEM analysis shows a particle size below 2 μm, where 20%Ca has slighty larger particles than the two other compositions. The particle size for the EDTA-powders was below 1 μm determined by SEM. Surface areas were 2.9–5.0 m^2/g, and the estimated particle size assuming spherical particles was 0.2–0.3 μm.

The uniaxially pressed pellets were sintered in air at 1050–1450°C for 2–96 h. The samples were heated at 300 K/h up to the maximum temperature and cooled down to 400°C at 1000 K/h.

Dilatometry (Netch Dilatometer 42OE) was performed on uniaxially pressed pellets (115 MPa). The green dimensions of the pellets were 1.0 cm diameter and height 0.7 cm. The dilatometry was performed in ambient air at a heating rate of 120 K/h.

Fractured, polished and etched cross-sections of sintered pellets were investigated by SEM (Zeiss DSM 940) and Energy Dispersive Spectroscopy (EDS) (Noran Instruments, Tracor Series 11). The polished surfaces were prepared by grinding with SiC-papers followed by polishing with diamond particles down to 1 μm. In order to visualize the grain boundaries, the polished samples were either etched in 6 M HCl for 1–4 min or thermally etched at 1050°C for 10 min. An estimate for the grain size was obtained by measuring the maximum 2-dimensional diameter of 20–50 grains on SEM images, and the mean values were reported as average grain size.

The density of G/N-samples was calculated from the weight and geometric volume of the sintered pellets while the density of EDTA-samples was measured by the "Archimedes" method in iso-propanol.

3. Results and discussion

3.1. Phase composition

Phases observed in addition to the perovskite phase in calcined powders and sintered ceramics are given in Table 2.

3.1.1. $LaCoO_3$

The phase compositions of near stoichiometric and non-stoichiometric $LaCoO_3$ powders were in accord with the equilibrium phase diagram of the La–Co–O system.[12] Co_3O_4 and $La(OH)_3$ were observed in, respectively, Co-excess and Co-deficient powders. Due to the high reactivity with moisture $La(OH)_3$ was probably formed from La_2O_3 during cooling or at ambient temperature. La_2O_3 in Co-deficient $LaCoO_3$ sintered at 1350°C is also clearly evident as lighter grains in Fig. 1a.

At Co-deficiency the phase composition during sintering was observed to change due to the redox-reaction:

$$1/2\ La_2O_3(s) + 3\ LaCoO_3(s) = La_4Co_3O_{10}(s) + 1/4\ O_2(g) \quad (1)$$

At 1450°C close to one third of the Co-deficient sample consists of rod-shaped grains of $La_4Co_3O_{10}$ as shown in Fig. 1b. However, equilibrium has not been reached and minor amounts of La_2O_3 are still present even after 2 h at 1450°C. 10 mol% Co-deficiency corresponds to 34 vol% $La_4Co_3O_{10}$ which is in good agreement with the observation. The coexistence of $La_4Co_3O_{10}$ and $LaCoO_3$ in air at 1450°C is in agreement with an extrapolation of the phase diagram reported by Petrov et al.[13] and Seppänen et al.[12]

In Co-excess $LaCoO_3$, Co_3O_4 was observed to decompose to CoO during sintering above 900°C in accordance with the Co–O phase diagram.[17] CoO was observed to oxidize in the powders during cooling to room temperature, but oxidation during cooling did not take place in dense $LaCoO_3$ ceramics.

3.1.2. 20%Sr

The phase composition of the calcined near stoichiometric and Co-deficient 20%Sr powders are also included in Table 2. The near stoichiometric powders contained only the perovskite phase according to the XRD analysis. At Co-deficiency minor amounts of $(La,Sr)_2CoO_4$ was observed in addition to the perovskite. The chemical composition of the K_2NiF_4 type phase was $(La_{0.6}Sr_{0.4})_2CoO_4$ according to the EDS analysis of sintered bodies. Hence, the Sr content in the $LaCoO_3$ phase is probably lower than 20 mol%. Pure La_2CoO_4 is not stable in air,[12] but the substitution of La by Sr probably results in replacement of Co(II) by Co(III), and the K_2NiF_4-type phase is therefore stabilized in air. The phase composition

Table 2
Phases observed in addition to the main perovskite phase in the calcined powders and sintered samples

Sample composition	Phases observed[a,b]				
	Calcined powder 900–1000°C	1200°C	1350°C	1400°C	1450°C
EDTA-samples					
Stoichiometric					
$LaCoO_3$	(none)	(*La_2O_3*, *La–Si–O*)	(*La_2O_3*, *La–Si–O*)	–	–
20%Sr	(none)	(*Sr–s*)	(*Sr–S*)	–	–
20%Ca	(none)	(*CoO*)	(*CoO*)	–	–
Co-deficient					
$LaCoO_3$	$La(OH)_3$	La_2O_3	La_2O_3	–	$La_4Co_3O_{10}$, La_2O_3
20%Sr	$(La,Sr)_2CoO_4$	$(La,Sr)_2CoO_4$	$(La,Sr)_2CoO_4$	–	$(La,Sr)_2CoO_4$
20%Ca	$(Ca_3Co_2O_6)$	CaO	$(La,Ca)_2CoO_4$	$(La,Ca)_2CoO_4$, '*liq. Ca–Co–O*'	–
Co-excess					
$LaCoO_3$	Co_3O_4	CoO, *La–Si–O*	CoO, *La–Si–O*	–	–
G/N-samples					
Stoichiometric					
$LaCoO_3$	(none)	(CoO, *La–Si–O*)	(CoO, *La–Si–O*)	–	–
20%Sr	(none)	(CoO)	(CoO)	–	–
20%Ca	(Co_3O_4)	(CoO)	(CoO, '*liq. Ca–Co–O*')	–	–

[a] Minor secondary phases are given in brackets.
[b] Phases written in italics are identified by EDS, and others are identified by XRD.

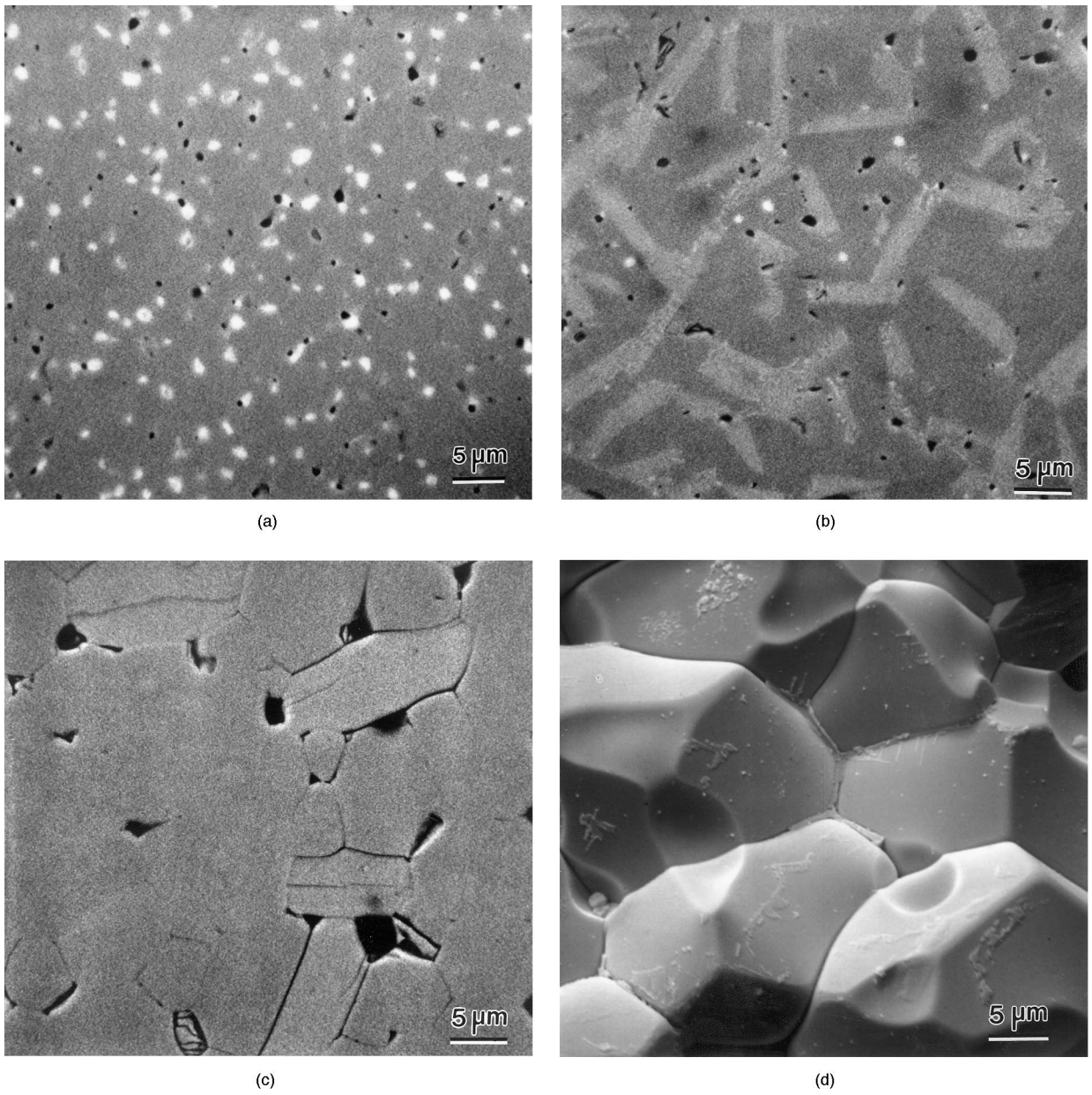

Fig. 1. SEM images of polished surfaces or fracture surface of Co-deficient samples sintered for 2 h. (a) $LaCoO_3$ at 1350°C, (b) $LaCoO_3$ at 1450°C, (c) 20%Ca at 1350°C and (d) 20%Ca at 1400°C.

of Co-deficient 20%Sr (Table 2) is not significantly altered during sintering of the calcined powders. CoO was observed in sintered 20%Sr G/N-samples indicating that this material is Co-excess relative to the perovskite stoichiometry.

3.1.3. 20%Ca

The Co-deficient 20%Ca powder contained the phase $Ca_3Co_2O_6$ in addition to the perovskite after calcination (Table 2). The Ca-content in the perovskite phase is lower than 20 mol% according to the chemical analysis and the presence of $Ca_3Co_2O_6$. The phase composition of Co-deficient 20%Ca was observed to change with increasing sintering temperature. After sintering at 1200°C, CaO with some solid solution of CoO was observed in addition to the major perovskite phase. This is probably due to the phase equilibrium:

$$yCa_3Co_2O_6(s) + LaCoO_3(s) = yCaO(s) + LaCa_{2y}Co_{1+2y}O_{3+5y}(s) \quad (2)$$

Only Co(III) is assumed in perovskite, and the initial content of Ca in $LaCoO_3$ and solid solution of CoO in CaO[18] are neglected here. The driving force of reaction (Eq. 2) is probably the decomposition of $Ca_3Co_2O_6$, reported at 1026°C in air.[18] A new phase with composition $(La_{0.6}Ca_{0.4})_2CoO_4$ (Table 2) with unknown structure

was observed after sintering at 1350°C, shown in Fig. 1(c). The observed XRD pattern cannot be interpreted to any known phase. However, the chemical composition found by EDS indicates that the phase is of K_2NiF_4 type. The chemical reaction taking place during heating to 1350°C is proposed to be

$$CaO(s) + LaCoO_3(s) = LaCaCoO_4(s) \quad (3)$$

Here, the solid solution of CoO in CaO and the Ca-content in $LaCoO_3$ are neglected. The change in the phase composition is probably due to a reduction of the mean valance state of Co with increasing temperature, which is neglected in reaction (Eq. 3).

A liquid phase has probably been formed in Co-deficient 20%Ca during sintering at 1400°C as shown in Fig. 1(d). The only relevant stable liquid reported in the literature is the eutectic at 1350°C and 65 mol% CoO in the pseudo binary phase diagram CaO-CoO.[18] A melt with approximate composition $Co_{0.65}Ca_{0.35}O$ is therefore proposed formed by a reaction between the perovskite and the K_2NiF_4-type phase. This is a reasonable explanation of the observed liquid phase in the sintered Co-deficient 20%Ca sample at 1400°C [see Fig. 1(d)].

In the Co-excess 20%Ca G/N-sample CoO was observed at 1200°C (see Table 2) and a liquid phase was observed after sintering at 1350°C. The precursor for the liquid phase is probably CoO(ss), which melts incongruently at a temperature near 1350°C depending on the Ca content.[18] The formation of a melt with approximate composition $Co_{0.65}Ca_{0.35}O$[18] would result in evolution of oxygen gas due to the reduction of the valance state of cobalt. This may explain the formation of the large pores observed after sintering at 1350°C.

Impurities of sulfur and silicon were observed in some of the sintered samples (Table 2). Sulfur originates from the EDTA used in the preparation of the powders. Silicon was mostly observed in pure $LaCoO_3$ and in larger amounts in the Co-excess composition.

The composition of the silicon containing phase measured by EDS was $La_{3.7}Si_{2.4}Co_{1.0}O_x$, but the observed XRD pattern could not be interpreted to any known phase. The silicon is most probably pollution from the mullite-tube in the furnace used during calcination of the powders. A reducing atmosphere may occur during calcination due to residual carbon from the synthesis, and this will result in formation of SiO(g) which may react with the perovskite powders.

3.2. Densification behaviour

Linear shrinkage and differential linear shrinkage during sintering at a constant heating rate of the three near stoichiometric G/N-samples are shown in Fig. 2. The densities after sintering were 79.4, 99.7 and 89.5% for $LaCoO_3$, 20%Sr and 20%Ca, respectively. $LaCoO_3$ sinters in a broader temperature interval than the Ca/Sr-substituted $LaCoO_3$. $LaCoO_3$ has only a single broad shrinkage event, while two sintering mechanisms are evident for the two other compositions (Fig. 2). The event observed at about 900°C for 20%Sr might be due to a solid state phase transition, while the second event observed at 1300–1350°C for 20%Ca is probably due to formation of the liquid CoO–CaO phase leading to liquid phase sintering.

The densification of $LaCoO_3$ based ceramics is shifted to lower temperatures when $LaCoO_3$ is substituted by Sr or Ca. It is unlikely that diffusion of oxygen is rate

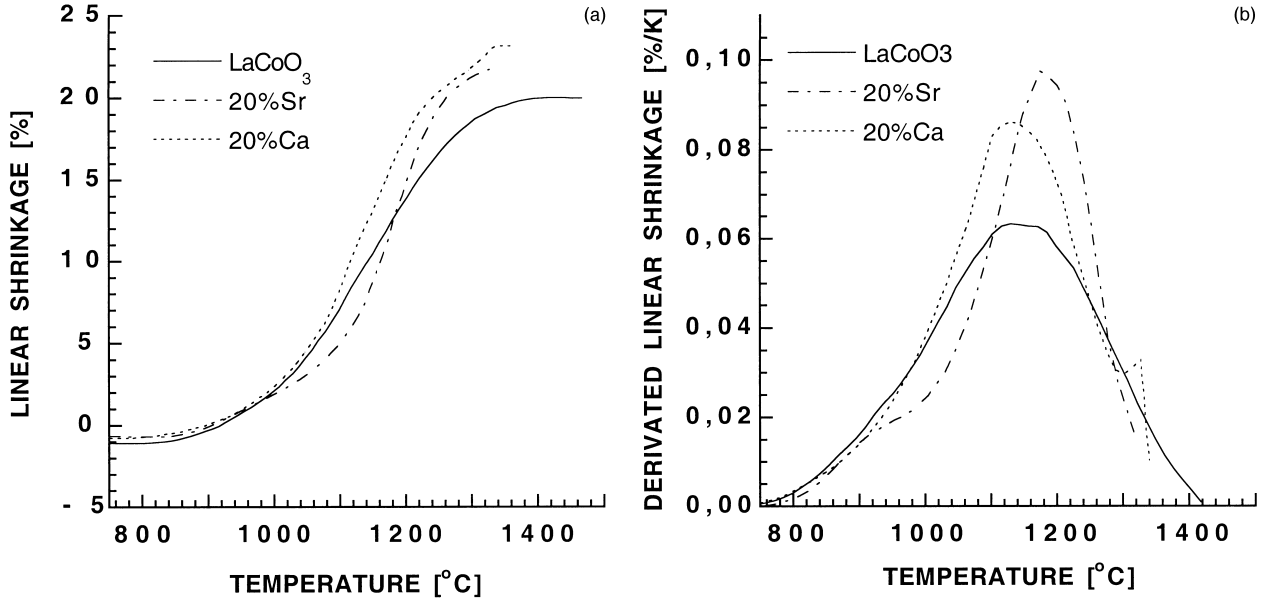

Fig. 2. (a) Linear shrinkage and (b) differential linear shrinkage during sintering of near stoichiometric G/N-powders; $LaCoO_3$, 20%Ca and 20%Sr. The heating rate is 120 K/h.

limiting during sintering since the materials are oxygen conductors even though the oxygen vacancy concentration increases with Ca/Sr-substitution. It is more probable that diffusion of the large A-cations are rate determining. By substitution of Sr and Ca the symmetry changes from hexagonal towards a more cubic structure shown by the decreasing rhombohedral angle (Rhombohedral angles obtained from the X-ray diffraction patterns are 60.79°, 60.55° and 60.68° for $LaCoO_3$, 20%Sr and 20%Ca, respectively). One could speculate that diffusion of cations increases with increasing symmetry since the average coordination number of the A-cations is highest in the cubic perovskite structure.

The densification of the G/N-powders was further investigated at isothermal conditions at 1050, 1200 and 1350°C based on the results in Fig. 2. Densification of EDTA-powders was investigated in the temperature interval 1200–1450°C. The density as a function of temperature for near stoichiometric, Co-excess and Co-deficient EDTA-samples is given in Fig. 3. The corresponding density of G/N-samples is given in Fig. 4. The crystallographic densities for stoichiometric samples, indicated by broken lines, were calculated from lattice parameters refined from XRD patterns of stoichiometric samples sintered at 1200°C.

Near 100% of theoretical density was obtained for near stoichiometric $LaCoO_3$ after sintering at 1350°C (Fig. 3), while lower densities are obtained for the non-stoichiometric samples. The theoretical density of the Co-deficient material is lower due to the lower low crystallographic density of the secondary phases La_2O_3 and $La_4Co_3O_{10}$. The evolution of $O_2(g)$ in Eq. (1) does not lead to increased porosity, probably due to slow reaction or due to enhanced grain boundary diffusion of oxygen. At Co-excess a higher porosity is observed. The presence of CoO inhibits sintering of the material. The melting point for CoO is considerably higher than for $LaCoO_3$, and the sintering temperature will be higher for the two-phase mixture than for single phase $LaCoO_3$. The corresponding explanation holds for Co-deficient $LaCoO_3$ at 1200°C where La_2O_3 is present. The $LaCoO_3$ G/N sample also

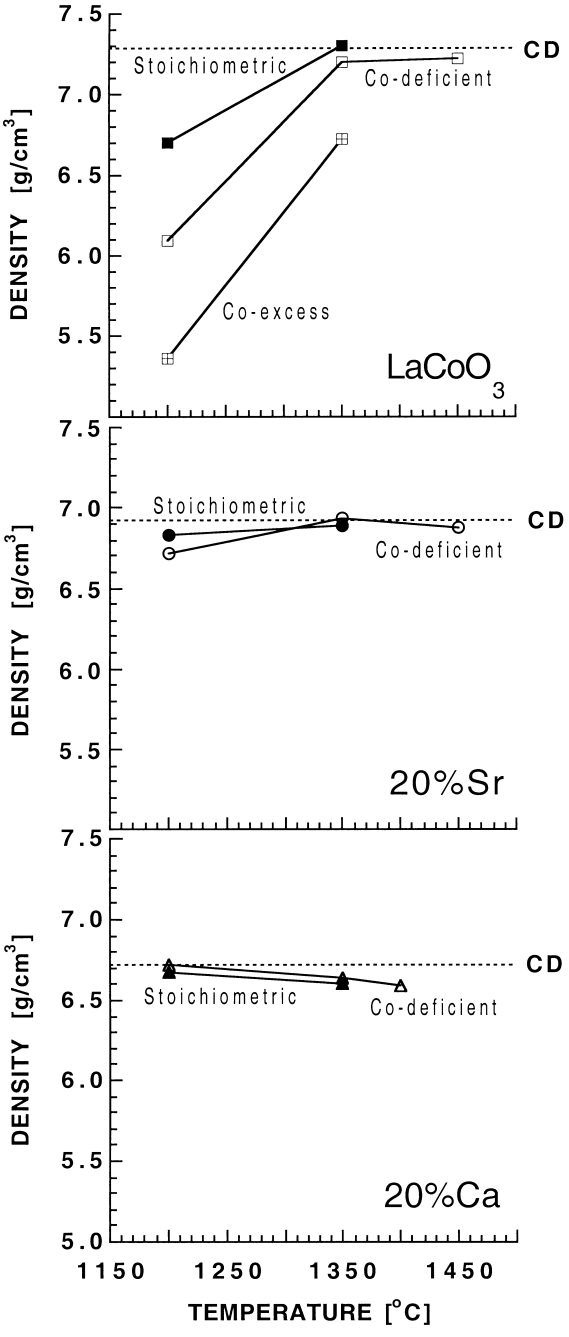

Fig. 3. Density after 2 h sintering at different temperatures for near stoichiometric (filled symbols), Co-deficient (open symbols) and Co-excess (crossed symbols) $LaCoO_3$, 20%Ca and 20%Sr. The powders were prepared by the EDTA-method. Crystallographic density is indicated by broken lines ($LaCoO_3 > 20\%Sr > 20\%Ca$). Crystallographic density was calculated from the hexagonal unit cell parameters a and c (Å) ($LaCoO_3$: 5.444 and 13.097, 20%Sr: 5.448 and 13.179 and 20%Ca: 5.432 and 13.101).

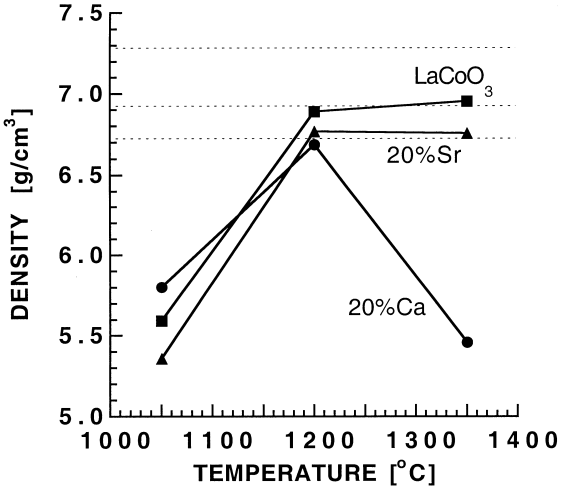

Fig. 4. Density after 2 h sintering at different temperatures for $LaCoO_3$, 20%Ca and 20%Sr. The powders were prepared by the G/N-method. Crystallographic densities are indicated by broken lines ($LaCoO3) > 20\%Sr > 20\%Ca$).

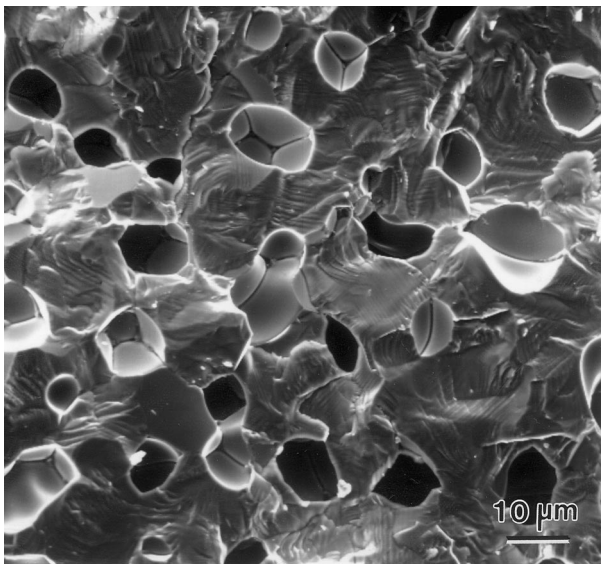

Fig. 5. Fracture surface of 20%Ca ceramic sintered at 1350°C for 2 h. The powder used was prepared by the G/N-method.

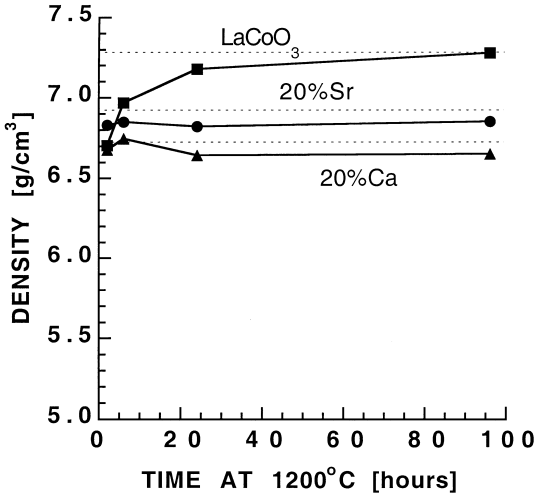

Fig. 6. Density after isothermal sintering for 2–96 h at 1200°C for near stoichiometric $LaCoO_3$, 20%Ca and 20%Sr. Powders were prepared by the EDTA-method. Crystallographic densities are indicated by broken lines ($LaCoO_3$ > 20%Sr > 20%Ca).

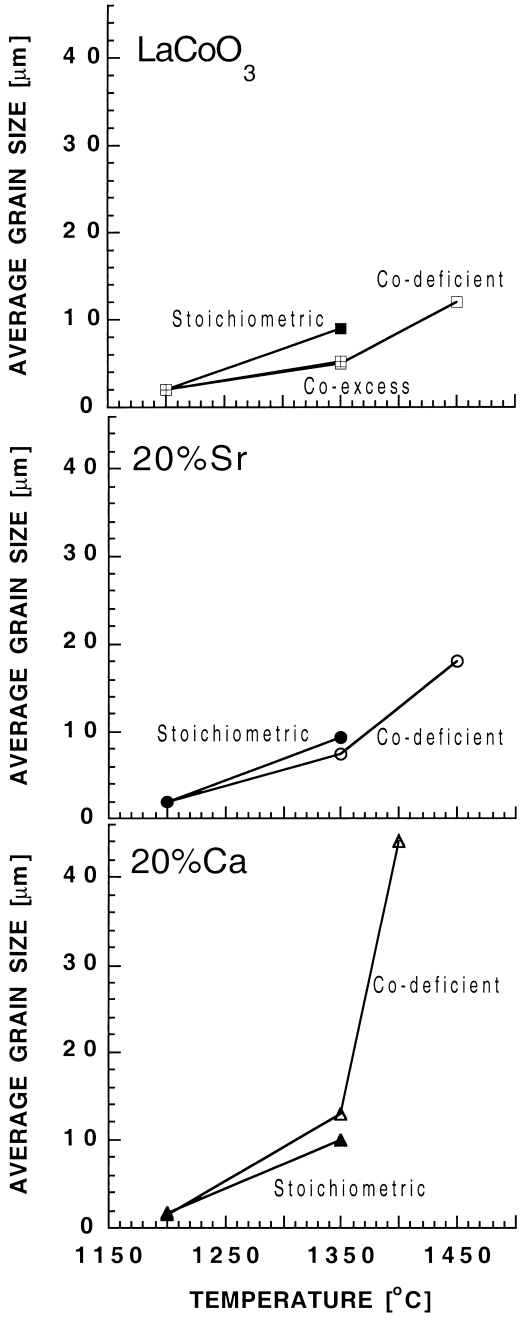

Fig. 7. Average grain size after sintering for 2 h at 1200–1450°C for near stoichiometric (filled symbols), Co-deficient (open symbols) and Co-excess (crossed symbols) $LaCoO_3$, 20%Ca and 20%Sr. Powders were prepared by the EDTA-method.

obtains a lower density than the near stoichiometric EDTA-sample. This is either due to a small Co-excess or larger initial particle size in the G/N-powder.

Both near stoichiometric and Co-deficient 20%Sr obtain high density in the whole temperature interval 1200–1450°C as can be seen from Figs. 3 and 4. The G/N-sample has slightly lower density, which is due to the small Co-excess or larger initial particle size.

Near stoichiometric and Co-deficient 20%Ca samples are nearly 100% dense after sintering at 1200°C, but the density slightly decreases with increasing sintering temperature (Fig. 3). The G/N-sample shows a more distinct trend (Fig. 4), and obtains a high porosity after sintering at 1350°C as shown in Fig. 5. The difference in porosity might be due to Co-excess indicated by the presence of Co_3O_4 in the calcined G/N powder. A reduction of cobalt takes place during the formation of the CaO–CoO eutectic melt and O_2(g) is formed. The evolution of the gas after pore closure might explain the high porosity observed at 1350°C. Evolution of gas due to volatile contaminates cannot be excluded as an alternative explanation of the high porosity.

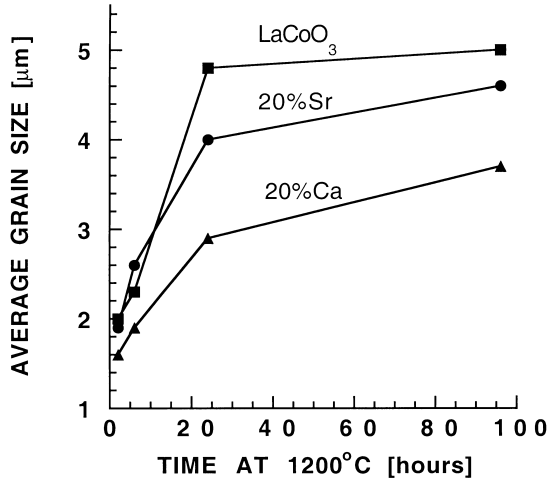

Fig. 8. Average grain size after isothermal sintering for 2–96 h at 1200°C for near stoichiometric $LaCoO_3$, 20%Sr and 20%Ca. The powders were prepared by the EDTA-method.

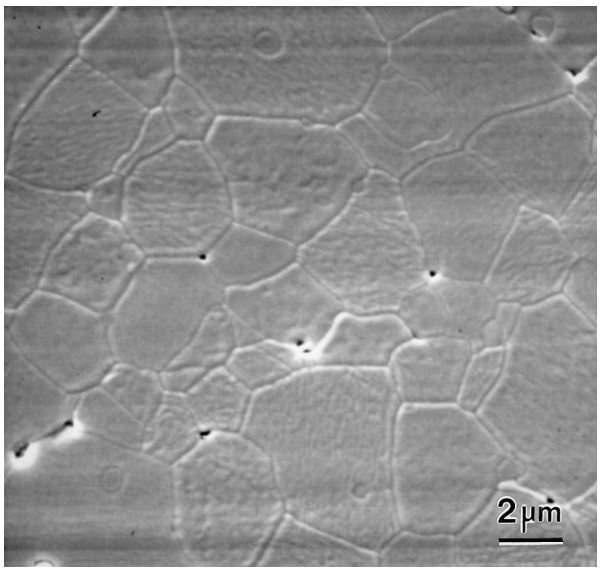

Fig. 9. SEM image of a thermally etched polished section of near stoichiometric $LaCoO_3$ sintered at 1200°C for 96 h. The powder was prepared by the EDTA-method.

Prolonged isothermal sintering at 1200°C for near stoichiometric materials increase the density for $LaCoO_3$ as shown in Fig. 6. 20%Sr and 20%Ca are already dense after 2 h.

3.3. Microstructure

The average grain size for EDTA-samples after sintering for 2 h in the temperature range 1200–1450°C is presented in Fig. 7. A larger extent of grain growth above 1200°C is observed in the substituted materials compared to $LaCoO_3$.

Smaller average grain size is observed in Co-excess and Co-deficient $LaCoO_3$ compared to near stoichiometric samples. The smaller grain size at non-stoichiometry is due to the presence of La_2O_3 or CoO acting as grain growth inhibitors by pinning the grain boundaries. At Co-excess micro cracking is observed, probably due to differences in thermal expansion of the two phases during cooling.

In 20%Sr samples the phase $(La,Sr)_2CoO_4$ is pinning the grain boundaries at Co deficiency, and therefore smaller grains are observed at Co-deficiency compared to the near stoichiometric samples (Fig. 7).

20%Ca shows the opposite behavior, and larger extent of grain growth has occurred at Co-deficiency compared to at near stoichiometry (Fig. 7). A change in sintering temperature and stoichiometry also has a stronger effect on the microstructure for 20%Ca than for the other compositions. This difference can be explained by the changes in phase composition during heating. The abrupt increase in grain size between 1350 and 1400°C at Co-deficiency is due to the presence of the liquid $Ca_{1-x}Co_xO$ phase described earlier. The liquid phase located at the grain boundaries can be seen in Fig. 1(d). Presence of a liquid phase enhances the mass transport leading to exaggerated grain growth in this case. The larger grains in the Co-deficient sample compared to the near stoichiometric sample sintered at 1350°C might be due to the reaction taking place between 1200 and 1350°C at Co-deficiency [Eq. (3)] leading to formation of relatively large amounts of $(La,Ca)_2CoO_4$ (Fig. 1c). This chemical reaction during sintering explains the opposite trends observed between Co-deficiency and near stoichiometry at 1350°C in Sr and Ca substituted compositions.

The microstructure of near stoichiometric $LaCoO_3$ and 20%Sr is qualitatively equal for the G/N-samples and EDTA-samples, however for 20%Ca at 1350°C the G/N-sample has twice as large grains (20 μm) compared to the near stoichiometric EDTA-sample. Additionally large pores are formed as was shown in Fig. 5. As discussed earlier this might be due to evolution of gas during the formation of a molten phase.

Fig. 8 shows how the grain size develops with time at 1200°C for near stoichiometric EDTA-samples. After approximately 24 h the grain growth has ceased, and the resulting grain size after 96 h is in the range 3–5 μm. Pores are mainly located at the grain boundaries, (Fig. 9). A qualitatively similar microstructure was observed for the three G/N samples sintered at 1200°C.

4. Conclusions

Substitution of La with Sr or Ca in $LaCoO_3$ decreases the sintering temperature. Near 100% dense materials are obtained for all compositions apart from the Co-excess $LaCoO_3$, though at different temperatures. The phase relations in the La–Co–O and Ca-Co-O systems

make it important to control the cation stoichiometry in order to avoid formation of secondary phases. In Ca substituted samples a small deviation from stoichiometry leads to formation of a liquid phase and exaggerated grain growth at high temperature. Presence of secondary phases may lead to cracking of the material and decline the functional properties. Preparation of dense and phase pure $LaCoO_3$ based ceramics is a demanding task, and dense single phased materials with small grains are obtained in a narrow temperature interval and a highly controlled cation stoichiometry is required.

Acknowledgement

Financial support from the Research Council of Norway is appreciated.

References

1. Ohno, Y., Nagata, S. and Sato, H., Properties of oxides for high temperature solid electrolyte fuel cells. *Solid State Ionics*, 1983, **9/10**, 1001–1008.
2. Muller, S., Striebel, K. and Haas, O., $La_{0.6}Ca_{0.4}CoO_3$: a stable and powerful catalyst for bifunctional air electrodes. *Electrochim. Acta*, 1994, **39**, 1661–1668.
3. Lindstedt, A., Strømberg, D. and Milh, M. A., High-temperature catalythic reduction of nitrogen monoxide by carbon monoxide and hydrogen over $La_{(1-x)}Sr_{(x)}MO_3$ perovskites (M = Fe, Co) during reducing and oxidising conditions. *Appl. Cat. A: General*, 1994, **116**, 109–126.
4. Balachandran, U., Dusek, J. T., Mieville, R. L., Poeppel, R. P., Kleefish, M. S. and Pei, S., Dense ceramic membranes for partial oxidation of methane to syngas. *J. Appl. Catalysis*, 1995, **133**, 19–29.
5. Gödickemeier, M., Sasaki, K. and Riess, L., Perovskite cathodes for solid oxide fuel cells based on ceria electrolytes. *Solid State Ionics*, 1996, **86/88**, 691–701.
6. Chen, C. H., Bouwmeester, H. J. M., van Doorn, R. H. E., Kruidhof, H. and Burggraaf, A. J., Oxygen permeation of $La_{0.3}Sr_{0.7}CoO_{(3-\delta)}$. *Solid State Ionics*, 1997, **98**, 7–13.
7. Koc, R. and Anderson, H. U., Liquid phase sintering of $LaCrO_3$. *J. Euro. Ceram. Soc.*, 1992, **9**, 285–292.
8. Denos, Y., Morin, F. and Trudel, G., Characterisation of pure and strontium substituted lathanum cobaltites synthesised by the glycine–nitrate process. *Proc. Electrochem. Soc.*, 1993, **93/94**, 231–240.
9. Janecek, J. J. and Wirtz, G. P., Ternary compounds in the system La–Co–O. *J. Am. Chem. Soc.*, 1978, **61**, 242–244.
10. Kitayama, K., Thermogravimetric study of the Ln_2O_3–Co–Co_2O_3 system. IV: Ln = La at 1100 and 1150°C. *J. Solid State Chem.*, 1997, **131**, 18–23.
11. Kitayama, K., Thermogravimetric study of the Ln_2O_3–Co–Co_2O_3 system. I: Ln = La. *J. Solid State Chem.*, 1988, **73**, 381–387.
12. Seppädnen, M., Kyto, M. and Taskinen, R., Stability of the ternary phases in the LaCo–O system. *Scan. J. Met.*, 1979, **8**, 199–204.
13. Petrov, A. N., Cherpanov, V. A., Zuyev, A. Y. and Zhukovsky, V. M., Thermodynamic stability of ternary oxides in Ln–M–O (Ln = La, Pr, Nd; M = Co, Ni, Cu) systems. *J. Solid State Chem.*, 1988, **77**, 1–14.
14. Morin, F., Trudel, G. and Denos, Y., The phase stability of $La_{0.5}Sr_{0.5}CoO_{3-\partial}$. *Solid State Ionics*, 1997, **96**, 129–139.
15. Munakata, F., Takahashi, H., Akimune, Y., Shichi, Y., Tanimura, M., Inoue, Y., Rittaporn, I. and Koyama, Y., Electronic state and valence control of $LaCoO_3$: difference between La-deficient and Sr-substituting effects. *Phys. Rev. B*, 1997, **56**, 979–982.
16. Chick, L. A., Pederson, L. R., Maupin, G. D., Bates, J. L., Thomas, L. E. and Exarhos, G. J., Glycine-nitrate combustion synthesis of oxide ceramic powders. *Mater. Lett.*, 1990, **10**, 6–12.
17. Aukrust, M. and Muan, A., Thermodynamic properties of solid solutions with spinel-type structure. I, The system Co_3O_4–Mn_3O_4. *Trans. AIME*, 1964, **230**, 378–382.
18. Woermann, E. and Muan, A., Phase equlibria in the system CaO–Cobalt oxide in air. *J. Inorg. Nucl. Chem.*, 1970, **32**, 1455–1459.

Paper II

Journal of the American Ceramic Society - *Accepted*

Sintering behaviour, microstructure and phase composition of $Sr(Fe,Co)O_{3-\delta}$ ceramics

Kjersti Kleveland, Mari-Ann Einarsrud and Tor Grande*

Department of Chemistry, Norwegian University of Science and Technology, 7491 Trondheim, Norway

*To whom correspondence should be addressed.

Abstract

$SrFe_{1-x}Co_xO_{3-\delta}$ (x=0, 0.33) ceramics have been prepared in the temperature interval 900-1350°C in air, nitrogen and oxygen atmosphere. The effect of cation non-stoichiometry on densification behaviour, microstructure and phase composition has been investigated. Densification of Sr-deficient $SrFeO_{3-\delta}$ initiates at a lower temperature than near stoichiometric $SrFeO_{3-\delta}$ probably due to enhanced diffusion of Sr. However, for Sr-deficient samples $Sr_4Fe_6O_{13}$ is formed above ~775°C causing a significant decrease in the sintering rate. It is therefore necessary to avoid Sr-deficiency in order to obtain dense $SrFeO_{3-\delta}$ ceramics. The densification rate was significantly increased by Co-substitution. Dense ceramics (>95% of theoretical density) of Sr-excess and Co-substituted $SrFeO_{3-\delta}$ were obtained by sintering in the temperature region 1000-1200°C. The grain size increases by increasing temperature, decreasing partial pressure of oxygen and Co-substitution. Exaggerated grain growth in the Co-substituted material occured at high temperatures. Sintering above 1200°C caused all materials, apart from Co-substituted $SrFeO_{3-\delta}$ in oxygen, to swell and develop a porous microstructure. The swelling mechanism was related to heterogenous phase equilibria, which is reductive in nature and leads to evolution of oxygen gas. The

phase equilibria are governed by the cation non-stoichiometry of the materials. The present findings demonstrate the importance of controlling the cation stoichiometry of ternary transition metal oxides in order to achieve ceramics with the desired homogenous microstructure. The mixed valence state of the transition metal may lead to both swelling during sintering and cracking during cooling due to reduction/oxidation during heating/cooling.

I. Introduction

$SrFe_{1-x}Co_xO_{3-\delta}$ ceramics are technologically interesting materials because of their high electronic and ionic conductivity at high temperature.[1] Possible applications are as oxygen sensors, batteries and electrodes in solid-oxide fuel cells. Of particular interest is the application as oxygen permeable membranes, which either can be used for oxygen production from air, or in the production of syngas ($CO+H_2$) by direct conversion of methane.[2] Oxygen permeable membranes require that the ceramic is stable in a wide oxygen partial pressure gradient, and mechanical properties (strength and creep rate) are important, especially if a pressure gradient is applied in addition to the chemical gradient. The objective of this study was to obtain dense $SrFeO_{3-\delta}$ based ceramics with the desired material properties for an oxygen permeable membrane. The effect of cation (Sr/Fe) stoichiometry, Co substitution and atmosphere on the sintering behaviour, microstructure and phase composition is considered.

The densification behaviour of $SrFe_{1-x}(Co,Cu)_xO_{3-\delta}$ ceramics has previously been studied by several groups. Densities higher than 96% have not been obtained, and swelling at high temperature has been reported. Kokhanovski et al.[3] prepared gas-tight ceramics of the composition $SrFe_{1-x}Co_xO_{3-\delta}$ (x=0, 0.25, 0.5, 0.75) where a maximum density of 96% was obtained for x=0.25 in the temperature interval 1240-1300°C. The compositions x=0 and x=0.25 were found to swell at high temperature prior to melting, and this was explained by extensive oxygen evolution near the melting point. Some results on the density of $SrCo_{1-x-y}Fe_xCu_yO_{3-\delta}$ ceramics have also been reported by Kharton et al.[1, 4] They obtained a density of 75-95% when x, y=0-0.5, and a density of 89-91% for x=0.25 and y=0.15. The sintering temperature was reported to decrease when Co was substituted with Cu.

High oxygen permeability of these materials is caused by the high oxygen deficiency at elevated temperatures.[2] The oxygen stoichiometry of $SrFeO_{3-\delta}$ has been studied by several authors.[5-8] For $SrFeO_{3-\delta}$ the oxygen non-stoichiometry (δ) can vary from 0 - 0.5 as the valence state of iron varies from Fe^{4+} to Fe^{3+} from partial pressure of oxygen of several hundred bars down to 10^{-5} bar. The crystal structure of $SrFeO_{3-\delta}$ changes with the oxygen non-stoichiometry and varies from cubic, tetragonal, orthorombic perovskite to orthorombic brownmillerite as δ goes from 0 to 0.5.[5] At high temperature a cubic phase is stable for all δ.[8, 9] These transformations will have an impact on the mechanical properties of dense membranes. $SrCoO_{3-\delta}$ has a wide range of oxygen stoichiometry since the valence state of cobalt can vary from Co^{4+} to Co^{2+} depending on oxygen partial pressure.[9] The structure corresponds either to a cubic perovskite or an orthorombic brownmillerite. However, $SrCoO_{3-\delta}$ is entropy stabilized and decomposes to the low temperature form, $Sr_6Co_5O_{15}$, and Co_3O_4, around 800-900°C depending on oxygen partial pressure.[11-14] Substitution of Fe with Co in $SrFeO_{3-\delta}$ stabilizes the cubic perovskite structure at low temperature. The oxygen stoichiometry of $SrFe_{1-x}Co_xO_{3-\delta}$ (x=0, 0.25, 0.5, 0.75) has been measured by Kokhanovski et al.[3] and they showed that at constant temperature δ increases with increasing Co content.

The phase equilibria in the Sr-Fe-O system in oxygen have been studied by Batti et al.[15] in the temperature interval 1000-1600°C. Ternary oxides in the system were $Sr_3Fe_2O_{7-\delta}$, $SrFe_{12}O_{19}$ and $Sr_7Fe_{10}O_{22}$ in addition to $SrFeO_{3-\delta}$, but the stoichiometry of the $Sr_7Fe_{10}O_{22}$ phase was later shown to be $Sr_4Fe_6O_{13}$.[16] $Sr_4Fe_6O_{13}$ has been shown to decompose to $SrFeO_{3-\delta}$ and $SrFe_{12}O_{19}$ below 775°C in air.[17]

II. Experimental

$SrFeO_{3-\delta}$ powders with variable cation stoichiometry and $SrFe_{2/3}Co_{1/3}O_{3-\delta}$ powders were prepared by spray pyrolysis from nitrate solutions (Norsk Hydro, Research Centre, Porsgrunn) and spray drying (Mini Spray Dryer B-191, Büchi) of a solution of nitrates and acetates. The concentration of the solutions was approximately 0.5 M. The spray dried powders were slowly heated to 250°C, kept there for 24 h and further heated to around 600°C where organic residues were burnt off during 24 h. The powders were ball milled (Si_3N_4-balls) for 24 h

in iso-propanol. The milled powders were calcined at 750-800°C for 8-80 h in flowing synthetic air and further ball milled for 24-48 h. Powder pellets (0.5 g) were uniaxially pressed (double action) at 40 MPa. The relative green density obtained was 40-45% of theoretical. The chemical composition of the spray pyrolysed powders was confirmed by atomic absorption spectroscopy (± 1 at%). The chemical composition (± 1 at%) of the spray dried powders was determined by thermogravimetrical analysis of the chemicals used. The chemical compositions of the powders are given in Table 1.

Table 1: Chemical composition, surface area and the corresponding estimated particle size assuming spherical particles. The estimated accuracy of chemical composition is ±1%.

Sample	Preparation method	Chemical composition	Surface area [m^2/g]	Particle diameter [μm]
SF-0.95	Spray drying	$Sr_{0.95}FeO_{3-\delta}$	7.11	0.15
SF-1.00	Spray drying	$SrFeO_{3-\delta}$	5.87	0.19
SF-1.05	Spray pyrolysis	$Sr_{1.05}FeO_{3-\delta}$	5.33	0.21
SFC	Spray pyrolysis	$Sr_{1.01}Fe_{0.63}Co_{0.37}O_{3-\delta}$	6.81	0.16

X-ray powder diffraction (XRD) of powders and crushed sintered samples was performed on a Siemens D5005 diffractometer (CuKα radiation and a secondary monochromator) in the 2θ range 10-90° with step 0.040° and step time 9.0 s.

The surface area of the powders was measured by nitrogen adsorption (ASAP 2000, Micromeritics) and was in the range 5.3 – 7.1 m^2/g corresponding to a particle size of ~ 0.2 μm assuming spherical particles.

Uniaxially pressed pellets were sintered in air, nitrogen ($P_{O2}<10^{-5}$atm) and oxygen at 900-1350°C for 6 h. The samples were heated at 200 K/h up to the maximum temperature and cooled down to room temperature at 50 K/h in air and in oxygen, and at 200 K/h in nitrogen. The density of the sintered pellets was measured by Archimedes' method in iso-propanol.

Dilatometry (Netch Dilatometer 420E) was performed on cold isostatically pressed pellets (200 MPa). The green dimensions of the pellets were 9 mm diameter and height 5 mm and the green density was 55% of theoretical.

Dilatometry was performed in air and nitrogen at a heating and cooling rate of 120 K/h. Thermal expansion of the dense materials was measured in air and nitrogen.

Fractured, polished and thermally etched cross-sections of the sintered pellets were investigated by SEM (Zeiss DSM 940) and Energy Dispersive Spectroscopy (EDS) (Noran Instruments, Tracor Series II). The polished surfaces were prepared by grinding with SiC-papers followed by polishing with diamond particles down to 1 μm. In order to reveal the grain boundaries, the polished samples were thermally etched at 950°C for 10 min. An estimate for the grain size was obtained by measuring the maximum 2-dimensional diameter of 20-50 grains on SEM images, and the mean values were reported as average grain size.

Thermal gravimetrical analysis was performed by a Perkin Elmer TGS-2 up to 700°C (accuracy ±1°C, ±0.2 μg) and a thermobalance in a tube furnace up to 1280°C (accuracy ±1°C, ±0.1 mg).

III. Results and discussion

(1) Densification

Linear shrinkage during sintering in air at a constant heating rate of near stoichiometric, Sr-excess and Sr-deficient SF is shown in Fig. 1. In this section, the densification behaviour prior to swelling (evident in Fig. 1 by the decreasing density with increasing temperature or time) will be discussed. The small difference in average grain size for the different powder compositions were assumed to play minor roles on the densification kinetics shown in Fig. 1. The near stoichiometric composition SF-1.00 is slightly Sr-deficient (table 2) and the densification of Sr-deficient (SF-0.95) and near stoichiometric (SF-1.00) materials initiates at a significantly lower temperature (700°C) than the Sr-excess material (750°C). SF-1.05 was also calcined at higher temperature (800°C) in order to achieve the same particle size as the Sr-deficient compositions (calcined at 750°C). The shift in initiation of the densification is more easily seen in Fig. 2 where the differential linear shrinkage with respect to temperature is shown. In these materials, cation diffusion is expected to be rate limiting due to the

extended anion deficiency. Thermogravimetry shows that SF-1.05 easily oxidizes down to around 350°C, which demonstrates a high diffusion rate of oxygen in the material. Diffusion of Sr or Fe must then be rate limiting, and the possible densification mechanisms are grain boundary and bulk diffusion.[19] Sr-deficiency is expected to form Sr-vacancies in the perovskite structure, and this will enhance diffusion of Sr. We therefore believe that the lower initiation temperature for sintering in SF-0.95 and SF-1.00 is due to enhanced diffusion of Sr because of Sr-deficiency in these materials. Based on ionic size of Sr (1.44 Å) and Fe (0.645 Å)[18] we would also expect diffusion of Sr to be rate limiting which is in agreement with the experimental data.

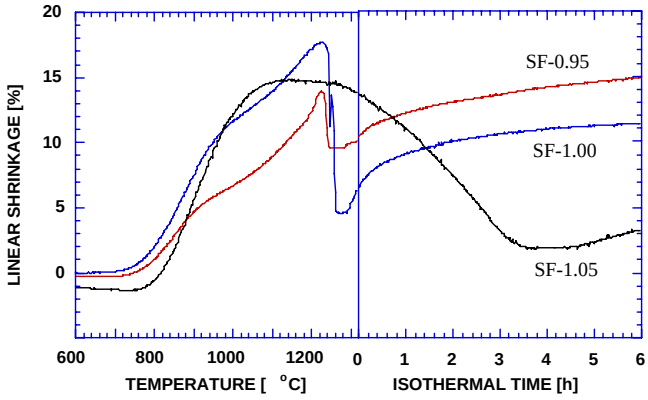

Figure 1: Linear shrinkage of SF-0.95, SF-1.00 and SF-1.05 during sintering at constant heating rate 120 K/h up to 1320°C and further at isothermal conditions at 1320°C. Note that the materials did not swell isotropically and the linear swelling is not reflecting the true change in density during swelling.

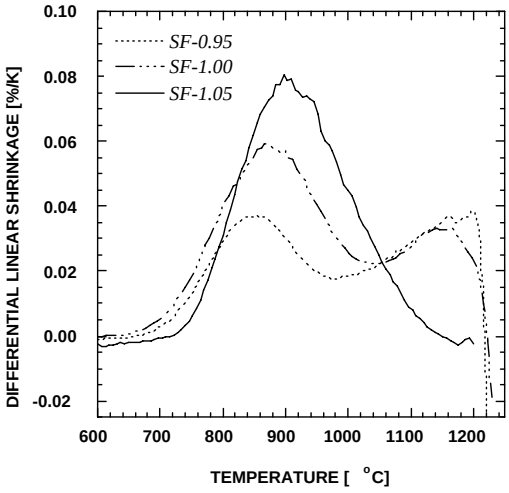

Figure 2: Differential linear shrinkage of SF-0.95, SF-1.00 and SF-1.05 in air. The heating rate was 120 K/h.

The differential linear shrinkage of SF-1.05 demonstrates only one peak, which indicates a single dominant sintering mechanism. Only the perovskite phase was observed for this composition up to 1200°C (table 2). For the two other compositions the densification rate is observed to decrease above 850°C before the rate increases again above 1000-1050°C. Due to the Sr-deficiency of SF-1.00 and SF-0.95, $Sr_4Fe_6O_{13}$[15] is formed during heating above ~775°C. The presence of $Sr_4Fe_6O_{13}$ was confirmed by XRD and/or SEM in sintered samples (table 2). It is therefore reasonable that the densification rate for these two compositions are suppressed. The effect of the secondary phase on sintering is reduced at high temperatures where the sintering rate is observed to increase again (Fig. 2). The formation of $Sr_4Fe_6O_{13}$ is described by the solid state reaction

$$SrFe_{1+x}O_{3-\delta} = x/2\ Sr_4Fe_6O_{13} + (1-2x)\ SrFeO_{3-\delta'} \qquad (1)$$

For simplicity the perovskite is assumed to become stoichiometric, and the reduction of the valence state of Fe due to the reaction is neglected. $Sr_4Fe_6O_{13}$ has been shown to be entropy stabilized and is only stable above 775 ± 25°C in accordance with the present observations.[17] At Sr-deficiency relative to

stoichiometric $SrFeO_{3-\delta}$, the single phase region becomes more narrow with increasing temperature, and $Sr_4Fe_6O_{13}$ will appear at a given temperature dependent on the overall composition of the perovskite and the kinetics of the nucleation and growth of the new phase. $Sr_4Fe_6O_{13}$ will therefore appear at a lower temperature and in a larger amount in SF-0.95 compared to SF-1.00. This explains that SF-0.95 has the slowest sintering rate and that the first maximum in sintering rate is reached at a lower temperature than SF-1.00.

Table 2: Secondary phases observed by XRD in samples sintered/heated in air and nitrogen. Phases observed by SEM are given in brackets.

Temperature [°C]	SF-0.95	SF-1.00	SF-1.05		SFC	
	Air	*Air*	*Air*	*N_2*	*Air*	*N_2*
750-800	none	none	none	-	none	-
1000	none	none	-	-	-	-
1100	[$Sr_4Fe_6O_{13+\delta}$]	none	-	none	none	[CoO]
1200	$Sr_4Fe_6O_{13+\delta}$	none	none	none	none	[CoO]
1300	-	[$Sr_4Fe_6O_{13+\delta}$]	$Sr_3Fe_2O_{7-\delta}$	-	[CoO (liq)]	[CoO (liq)]
1320	$Sr_4Fe_6O_{13+\delta}$	[$Sr_4Fe_6O_{13+\delta}$]	none	-	-	-

The density of the three SF materials after isothermal sintering in air for 6 h in the temperature range 1000-1300°C is presented in Fig. 3. The theoretical density of these materials, which is not known accurately, is expected to depend on both the cation stoichiometry and oxygen content, and we have therefore given the absolute density. The only theoretical densities known in the literature are the density of the compositions $SrFeO_{2.86}$ (5.46 g/cm^3)[5], $SrFeO_{2.73}$ (5.38 g/cm^3)[5] and $SrFeO_{2.50}$ (4.99 g/cm^3)[20] corresponding to crystals with ordered anion vacancies. The density of the non-stoichimetric materials is expected to be close to the density of the stoichiometric materials. The oxygen content of the

dense SF-1.05 was determined by thermal gravimetrical analysis to be $SrFe_{0.95}O_{2.79}$ assuming that only three valent Fe was present in N_2(g) at high temperature.

SF-1.05 obtained a high density (> 95%) already at 1000°C, while the two other compositions were only partly densified at 1000°C. This is in agreement with the densification rate obtained from Fig. 2. The density of SF-1.00 increases with the sintering temperature up to 1200°C, while the density of SF-0.95 increases from 1000 to 1100°C. The densification of SF-1.00 and SF.0.95 is suppressed due to the formation of $Sr_4Fe_6O_{13}$ as discussed above. We can therefore conclude that Sr-excess is a necessary prerequisite in order to avoid formation of $Sr_4Fe_6O_{13}$ and to obtain dense materials.

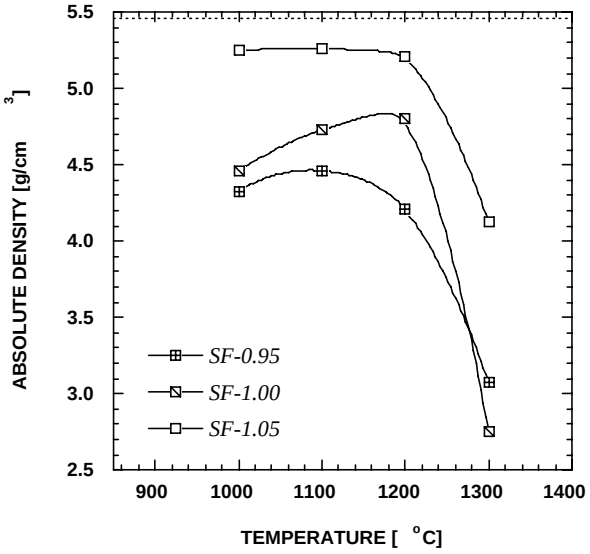

Figure 3: Density of SF ceramics after sintering in air for 6 h at different temperatures. Theoretical density of $SrFeO_{2.86}$ is shown by the broken line.

Substitution of Fe with Co increases the sintering rate as can be seen in Fig. 4, where the differential linear shrinkage of SF-1.05 and SFC at constant heating rate is shown. The densification is initiated in the same temperature region for both materials, but the sintering rate is significantly higher with Co substitution. When Fe is substituted by Co, it has been shown that the anion vacancy concentration is increasing.[3] It is also known that the molar volume of the perovskite unit cell is increasing with decreasing average valance state of the transition metal (increasing oxygen vacancy concentration).[1] We propose that the increased molar volume by Co substitution enhance diffusion of cations (possibly due to change from cation vacancy to cation interstitial mechanism) and thereby increasing the sintering rate.

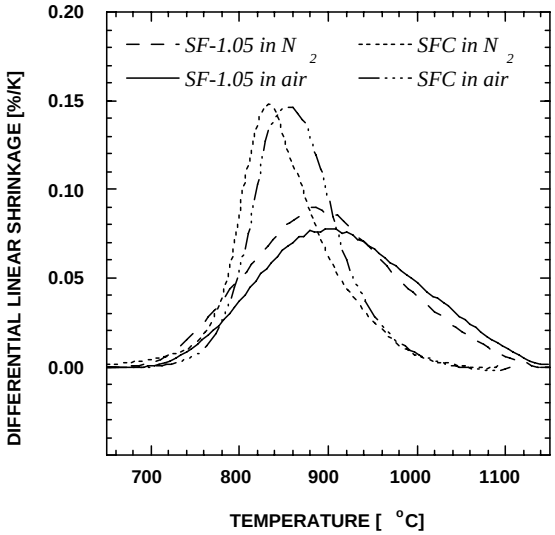

Figure 4: Differential linear shrinkage of SF-1.05 and SFC in air and nitrogen. The heating rate was 120 K/h.

The effect of the anion vacancy concentration on the densification properties of SF-1.05 and SFC was further studied by sintering of the materials in nitrogen where the anion vacancy concentration is significantly higher compared to in air. The differential linear shrinkage in nitrogen is qualitatively the same as in air (see Fig 4), but the sintering is initiated at a lower temperature and the sintering event is more narrow. We therefore propose that the solid state sintering is enhanced with increasing oxygen vacancy concentration due to a lower valence state of the transition metal and thereby a higher molar volume of the unit cell.

The densities of SF-1.05 and SFC obtained after isothermal sintering for 6 h in the temperature range 1000-1350°C in air, nitrogen and oxygen are given in Fig. 5. Note that the theoretical density of the materials is very dependent on the oxygen partial pressure. The higher absolute densities obtained in pure oxygen, relative to the density obtained in air, are mainly due to higher valence state of the transition metal and thereby a higher theoretical density (the samples oxidize during cooling, and the oxygen content depends on the partial pressure of oxygen). The density of $SrFeO_{2.86}$ (5.46 g/cm^3)[5] and $Sr_2Fe_2O_5$ (4.99 g/cm^3)[20] are the most appropriate theoretical densities in respectively air and nitrogen. The crystallographic density at constant oxygen content is expected to increase somewhat by Co-substitution. The relative densities of SF-1.05 and SFC between 1000-1200°C are therefore > 95 % independent of the sintering atmosphere.

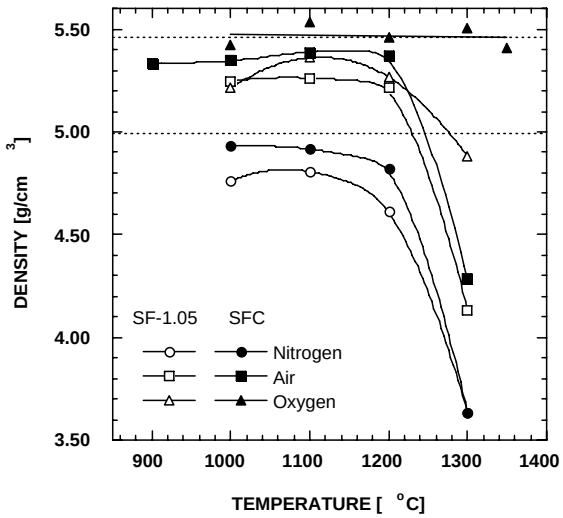

Figure 5: Density of SF-1.05 and SFC ceramics after sintering in nitrogen, air and oxygen for 6 h at different temperatures. Theoretical densities of $SrFeO_{2.86}$ and $SrFeO_{2.50}$ is shown by the broken lines.

The average grain size of the samples discussed in Fig. 5, is presented in Fig. 6. The microstructure of the SFC sintered at 1000°C and 1100°C in air are shown in Fig. 7. At 1000°C the microstructure is homogeneous, and the average grain size is ~3 μm. Sintering at 1100-1200°C leads to exaggerated grain growth, Fig. 7b. The microstructure is inhomogeneous with large grains up to 100 μm and small grains in the order of 5-10 μm. Mean values are plotted in Fig. 6. Pores are small relative to the grain size and they are distributed evenly inside the grains and at the grain boundaries. The exaggerated grain growth is shifted towards higher temperature (above 1100°C) in oxygen, where the largest grains are in the order of 60 and 90 μm at respectively 1200 and 1300°C. Exaggerated grain growth is not observed in SFC sintered in nitrogen at 1000-1200°C. A secondary solid phase rich in cobalt was observed in the SFC ceramics sintered at 1100°C and 1200°C in nitrogen (table 2). Secondary phases have previously been observed to act as grain growth inhibitors in perovskites[21] and this might explain the difference between the grain boundary mobility in nitrogen compared to in air and oxygen where secondary phases could not be detected below 1300°C.

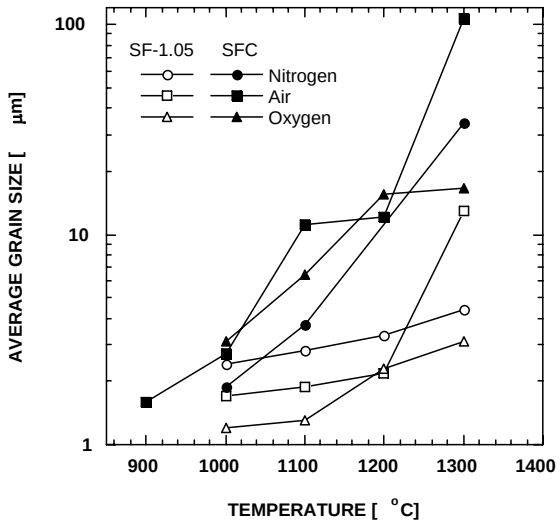

Figure 6: Average grain size of SF-1.05 and SFC ceramics after sintering in nitrogen, air and oxygen for 6 h at different temperatures.

The grain growth in SF-1.05 is less pronounced, and the average grain size of all the SF-1.05 samples sintered between 900-1200°C is small (1-5 μm) relative to the grain size in SFC. The grain size seems to increase with decreasing oxygen partial pressure. Generally, increased oxygen vacancy concentration, either as a result of decreased oxygen partial pressure or by substitution of Fe by Co, seems to increase the grain boundary mobility and the sintering rate in single phase materials.

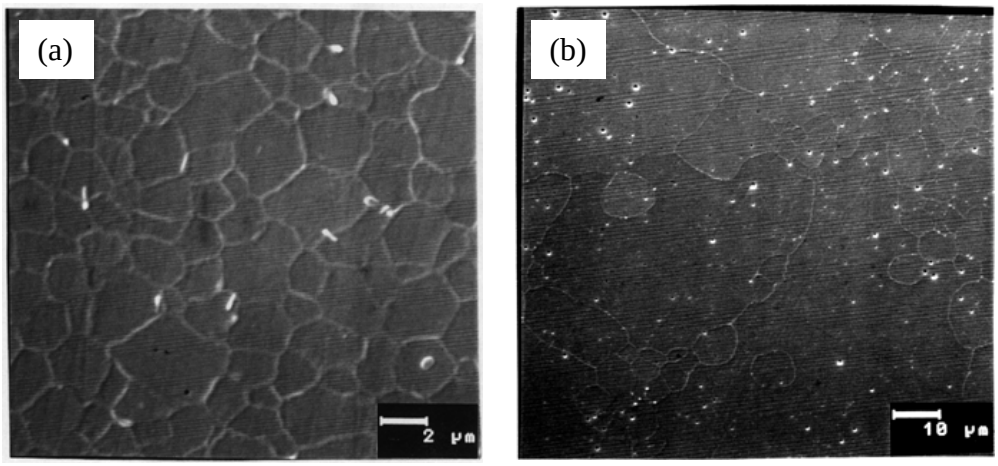

Figure 7: SEM image of a polished and thermally etched cross section of SFC sintered in air for 6 h at a)1000°C and b)1100°C.

(2) Swelling

All the three SF materials were observed to swell considerably above 1200°C (Fig. 1 and 5). The microstructure of the three materials after heating and isothermal holding at 1320°C for 6 h in the dilatometer is shown in Fig. 8. All three microstructures are porous, and density measurements by Archimedes´ method showed that the majority of the final porosity is open. The porosity has probably transformed from closed to open when the total porosity has approached large values (30-50%). Note the significant difference of the pore size of SF-1.05 (5-10 μm) relative to the two other materials with pores in the order of 100 μm (SF-0.95) and 20-60 μm (SF-1.00).

Initially, we were afraid that the swelling was due to decomposition of small amounts of $SrCO_3$ or $SrSO_4$ resulting in evolution of gas. We observed traces of these impurities in the raw powders from spray pyrolysis and EDTA synthesis. However, IR-spectroscopy of the materials below and above the temperature of the swelling gave no evidence for IR-absorption due to carbonates or sulfates. We therefore concluded that the swelling is indeed an intrinsic property of these materials.

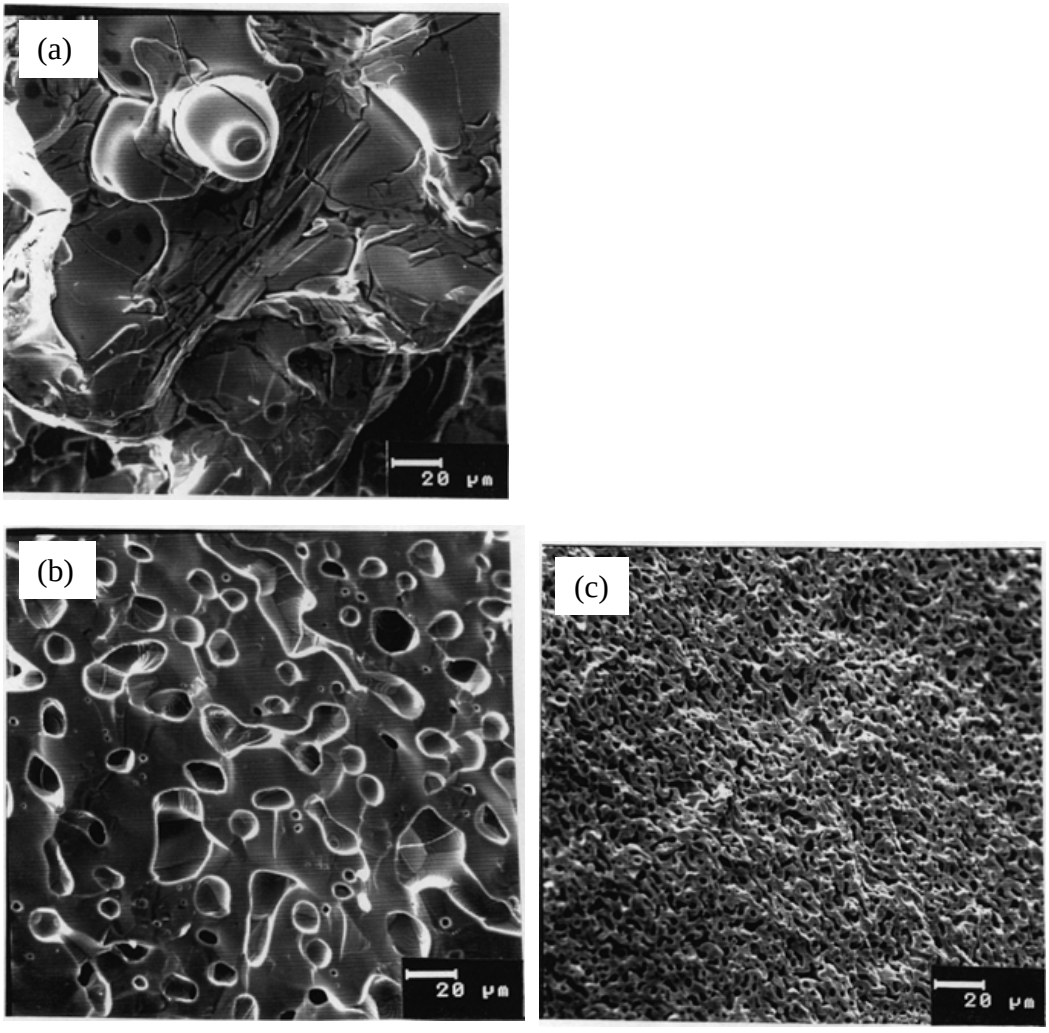

Figure 8: SEM fractographs of a) SF-0.95 b) SF-1.00 and c) SF-1.05 after dilatometry at 1320°C in air.

Grain growth and pore coalescence will contribute to the observed swelling. When two closed pores on neighboring grain boundaries intersect each other by grain growth, they will form one larger pore with a larger volume at equilibrium compared to the volume of the two initial pores at equilibrium. However, this mechanism can only account for a few percent volume expansion[22] and it can not

explain the amount of swelling observed here. This suggest that the swelling observed in these systems will have to be explained by an additional mechanism.

The swelling of both SF-0.95 and SF-1.00 initiates at 1220°C as shown in Fig. 1. The swelling is already terminated at about 1260°C or after 15 min. The temperature of the swelling coincides with a peritectic point at 1243±10°C (in $O_2(g)$) reported by Batti et al.[15] where $Sr_4Fe_6O_{13}$ decomposes to $SrFeO_{3-\delta}$ and a liquid phase. The swelling observed indicates gas evolution, and a tentative reaction is:

$$Sr_4Fe_6O_{13} = Sr_2Fe_2O_5 + 2\ SrFe_2O_3\ (liq) + O_2(g) \qquad (2)$$

The oxidation state of iron is assumed to be Fe^{3+} in the solid phases and Fe^{2+} in the liquid phase. The Sr/Fe ratio in the liquid phase is based on the peritectic composition reported by Batti et al.[15] Even small amounts of $Sr_4Fe_6O_{13}$ will produce a relatively large volume of oxygen gas relative to the sample volume. The rapid expansion of these two materials is driven by the evolution of gas, and the mass transport mechanism for the swelling is most probably viscous flow due to the formation of the liquid phase. Thermal gravimetric analysis of SF-0.95 was performed during sintering in air in order to confirm the oxygen evolution in Eq. 2. During 30 min at isothermal conditions at 1240°C a weight loss of about 0.13 wt% was observed. The two materials continue to sinter after the driving force for swelling has diminished either because the gas evolution due to Eq. 2 has ceased or all the pores have been opened.

During cooling, $Sr_4Fe_6O_{13}$ will reappear when the melt solidify, which was observed in SF-0.95 by XRD (Table 2). The $Sr_4Fe_6O_{13}$ phase is also clearly observed by microscopy in SF-0.95 (Fig. 8a) because the morphology of $Sr_4Fe_6O_{13}$ is different from the main perovskite phase. The grains which are elongated are mainly located at the grain boundaries of the perovskite. Also in SF-1.00 small amounts of elongated grains are observed on the inner surface of the pores (Fig. 8b), but the amount is not detectable by XRD. However, the sintering and swelling behaviour demonstrate that $Sr_4Fe_6O_{13}$ is also formed in this sample.

The nature of the swelling of SF-1.05 is different from the two other SF-materials. SF-1.05 starts to swell slowly at about 1250°C and continues to swell

at isothermal conditions at 1320°C for about 4 h. Only solid phases are present below 1500°C when Sr/Fe > 1.[15] The mechanism of the swelling is therefore different as inferred from the microstructure (Fig. 8c). We propose that the swelling is related to the temperature dependence of the solid solubility of SrO in $SrFeO_{3-\delta}$. If the solid solution of SrO in $SrFeO_{3-\delta}$ becomes narrower with increasing temperature, $Sr_3Fe_2O_{7-\delta}$ will precipitate at some temperature during heating. A tentative reaction is:

$$Sr_{2+x}Fe_2O_{5+\delta} = (1-x)\ Sr_2Fe_2O_5 + x\ Sr_3Fe_2O_6 + (\delta-x)/2\ O_2(g) \qquad (3)$$

where the oxidation state of iron in the product phases is assumed to be Fe^{3+}. We expect that this reaction also is reductive in nature with increasing temperature implying that oxygen is evolved ($\delta>x$). This is the case if the excess SrO in $Sr_2Fe_2O_5$ stabilizes a higher oxidation state of iron (Fe^{4+}). Generally a basic oxide as SrO will stabilize higher oxidation states of iron as shown by the presence of Fe^{4+} in $SrFeO_{3-\delta}$ at lower temperatures. The microstructure of this material is homogeneous with grains and pores in the order of 5-10 μm (Fig. 8c). The proposed secondary phase $Sr_3Fe_2O_6$ could not be detected by XRD or SEM in the sample after dilatometry, but a secondary phase was observed by microscopy in a sample sintered at 1300°C. The secondary phase is visible in Fig. 9a as elongated grains in the pores. XRD on the corresponding sample indicates that the phase is $Sr_3Fe_2O_{7-\delta}$ as expected from the phase diagram (Table 2).[15] Thermal gravimetrical analysis during heat treatment in air was performed in order to detect any weight loss due to oxygen evolution as proposed from Eq. 3. A 0.02 wt% weight loss was observed during 6 h at 1280°C. The density was 84% of theoretical but most of the porosity was still closed which might explain the low weight loss. Unfortunately, we were not able to perform thermogravimetry above 1280°C due to experimental limitations. We would expect the weight loss to be more pronounced at higher temperature.

The reaction in Eq. 3 is expected to be slower than the peritectic decomposition at Sr-deficiency (Eq. 2) because only solid phases are involved at Sr-excess. A slow reaction might explain the slow swelling observed (Fig. 1). However, it is a question why the oxygen produced in the reaction does not diffuse out of the material instead of increasing the porosity, since anion diffusion is expected to be faster than cation diffusion. The swelling due to Eq. 3 ceases after 3.5 h at 1350°C (Fig. 1). This is probably due to an increasing amount of open porosity

and termination of Eq. 3. The material continues to slowly densify after the swelling period.

A porous microstructure was also observed for the SF-1.05 sample sintered at 1300°C in air (Fig. 6). The microstructure was however less homogenous and pores up to 30 μm and and grains sized around 10 μm was evident in the majority of the sample (Fig. 9a). Regions with smaller pores in the range 3-5 μm were also present. It is important to note that the dilatometer sample was formed by CIP, while the other was uniaxially pressed. In addition the heating rate was 120°C/h for the first and 200°C/h for the second. The evolution of the porosity of SF-1.05 ceramics sintered at 1300°C was observed to depend on the oxygen partial pressure as predicted from Eq. 3 (Fig. 5).

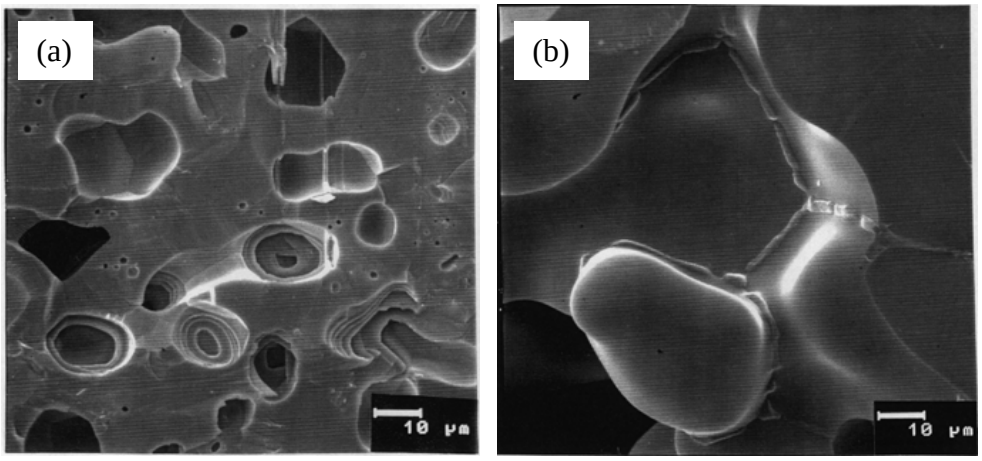

Figure 9: SEM fractographs of a) SF-1.05 and b) SFC after sintering in air for 6 h at 1300°C.

Swelling above 1200°C was also observed for the Co-substituted material when heated in air or nitrogen. However, materials with high density was obtained up to 1350°C in oxygen. The microstructure of desintered SFC in both air and nitrogen revealed the presence of a secondary phase at the grain boundaries as shown in Fig. 9b. The morphology is typical for liquid phase sintered materials, and the secondary phase was probably molten at the sintering temperature. The molten phase is rich in Co according to EDS analysis. The phase relations in the

Sr-Co-Fe-O system is not known to our knowledge. We propose that the formation of the liquid phase is related to cation non-stoichiometry relative to the ideal perovskite stoichiometry. Since the secondary phase is rich in Co, it is likely to believe that the total composition is slightly Sr-deficient. The cobolt rich liquid phase contains mainly divalent Co according to the Co-O phase diagram.[23] The formation of CoO is therefore reductive in nature and oxygen gas will be involved. The absence of swelling and secondary phases in pure oxygen, and the presence of the Co-rich secondary phase above 1000°C in nitrogen (table 2) shows that the solid solubility of excess CoO in the perovskite is clearly dependent on the partial pressure of oxygen.

The formation of the liquid phase enhances grain growth as shown in Fig. 6. SFC sintered at 1300°C in air consists of grains in the order of 100 μm and very large pores, some with diameter larger than 300 μm. A large share of the porosity is open. The corresponding swelling and grain growth is also observed in SFC sintered in nitrogen at 1300°C. The grains are about 30-40 μm, and pores are up to 100 μm. A large share of the porosity is open also for this sample.

(3) Cracking

We observed that several of the samples that were prepared had developed cracks during sintering or cooling. The cracks typically were initiated at the surface and had propagated towards the center of the discs, parallel to the cylindrical axis. This kind of cracking is probably not caused by pressing defects during green body preparation because pressing defects are normally end-capping, ring-capping or lamination. The cracking was most evident in oxygen, and almost no cracking was observed after sintering in nitrogen. Microscopy of the fracture surface revealed considerable etching of the grain boundaries. Mass transport is initiated around 750°C according to the dilatometry (Fig. 1 and 2). The cracks have therefore developed during cooling down to about 750°C.

We propose that cracking is due to oxidation of the perovskite during cooling. The oxidation of Fe^{3+} to Fe^{4+} leads to a significant contraction of the unit cell (density of $SrFeO_{2.5}$ and $SrFeO_{2.86}$ are respectively 4.99 and 5.46 g/cm^3). In the following we will use the term chemical contraction/expansion to describe the effect of oxidation/reduction of the transition metal.

Thermal expansion of SF-1.05 in air and in nitrogen is shown in Fig. 10. Below 600°C the thermal expansion coefficient is around $10 \cdot 10^{-6}$ K^{-1}. There is a large increase in thermal expansion coefficient in air around 600°C, and a maximum value of around $50 \cdot 10^{-6}$ K^{-1} is reached around 800°C. This is due to the chemical expansion described previously. In nitrogen the thermal expansion coefficient is constant up to 750°C because the oxygen stoichiometry is constant (δ=0.5) during heating. There is a shift around 750°C due to the transition from the orthorombic brownmillerite to the cubic perovskite.[5] The value is around $15 \cdot 10^{-6}$ K^{-1} below 750°C, and around $10 \cdot 10^{-6}$ K^{-1} above 750°C. The thermal expansion of SFC is qualitatively the same as for SF-1.05. Kharton et al.[1] reported a thermal expansion coefficient of $18 \cdot 10^{-6}$ K^{-1} for $SrFe_{0.5}Co_{0.5}O_{3-\delta}$ in the temperature interval 300-750 K, and $33 \cdot 10^{-6}$ K^{-1} in the temperature interval 800-1100 K which is in fairly good agreement with what we have observed.

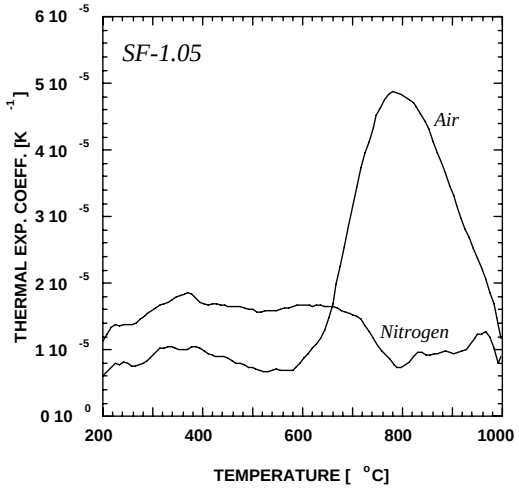

Figure 10: Thermal expansion coefficient of SF-1.05 in air and nitrogen. The heating rate was 120 K/h.

The bulk diffusivity of oxygen in these perovskites is decreasing with decreasing temperature. The decreasing temperature also gives a rise in the equilibrium oxygen content (δ in $SrFeO_{3-\delta}$ decreases). At a particular temperature during cooling the diffusivity of oxygen is too low to maintain the equilibrium oxygen content, and a chemical gradient in the oxygen vacancy concentration will build

up. The surface will then be more oxidized relative to the bulk and tensile stresses will appear at the surface. The cracking would therefore be less pronounced at lower partial pressure of oxygen in accordance with the results obtained in nitrogen. This would also imply that the specimen size will affect the probability of cracking.

A simple calculation can be done on a model system of two parallel plates stuck to each other. If one assumes Young's modulus of 100 GPa and a thermal/chemical expansion coefficient of $50 \cdot 10^{-6}$ K^{-1} at 800°C a temperature difference of 10°C between the plates will cause a stress of 50 MPa. This is near the strength of the material at this temperature, and cracks will form. Surface defects will seriously decrease the strength of the material because cracks initiate more easily on defects.

IV. Conclusions

The sintering behaviour of $SrFeO_{3-\delta}$ based ceramics is shown to be very dependent on the Sr/Fe stoichiometry. The initiation temperature for sintering is decreased by Sr-deficiency probably due to enhanced diffusion of Sr. However, at Sr-deficency $Sr_4Fe_6O_{13}$ is formed at temperatures above ~775°C causing the sintering rate to decrease. It is therefore necessary to avoid Sr-deficiency in order to obtain dense $SrFeO_{3-\delta}$ ceramics. The densification rate of $SrFeO_{3-\delta}$ is significantly increased by Co-substitution.

Exaggerated grain growth of Co-substituted $SrFeO_{3-\delta}$ occur at high temperatures in air and oxygen. At intermediate temperatures the grain growth was inhibited in nitrogen due to formation of a solid secondary phase. Generally in single phase $SrFe_{1-x}Co_xO_{3-\delta}$, the grain size increases by decreased oxygen partial pressure and by Co-substitution.

Heating at higher temperatures resulted in significant swelling of the ceramics. The expansion mechanism was related to heterogenous phase equilibria which leads to the evolution of oxygen gas. The secondary phases involved in these phase equilibria are determined by the cation stoichiometry of the materials. In the case of Sr-deficiency molten secondary phases are formed and the materials expands rapidly probably due to viscous flow.

The present findings illustrate the importance of controlling the cation stoichiometry of ternary transition metal oxides in order to achieve the desired homogenous microstructure with grains in the range of microns.

V. Acknowledgements

Financial support from the Research Council of Norway, Statoil, and Norsk Hydro ASA is acknowledged. We also thank Rita Glenne at Norsk Hydro for preparing some of the powders.

VI. Literature

1. V.V. Kharton, E.N. Naumovich, A.V. Nikolaev, V.V Astashko, and A.A. Vecher, "Elctrochemical properties of mixed $SrCo(Fe,Cu)O_{3-\delta}$ conductors," *Russ. J. Electrochem.*, **29**, 1201-09 (1993).
2. V.V Kharton, E.N. Naumovich, and A.V. Nikolaev, "Materials for high-temperature oxygen membranes," *J. Membrane Science.*, **111**, 149-57 (1996).
3. L.V. Kokhanovskii, V.V Vashuk, E.F. Villkotskaya, S.I. Vitushko, and M.V. Zinkevich, "Synthesis, structure and some physiochemical properties of $SrCo_{1-x}Fe_xO_{3-\delta}$," *Inorg. Mater.*, **35**, 262-86 (1999).
4. V.V. Kharton, V.N. Tikhonovich, L. Shuangbao, E.N. Naumovich, A.V. Kovalevsky, and A.P. Viskup, "Ceramic microstructure and oxygen permeability of $SrCo(Fe,M)O_{3-\delta}$ (M = Cu or Cr) perovskite membranes," *J. Electrochem. Soc.*, **145**, 1363-73 (1998).
5. Y. Takeda, K. Kanno, T. Takeda, O. Yamamoto, M. Takano, and N. Nakayama, "Phase relation in the nonstoichiometric system $SrFeO_x$ ($2.5 < x < 3.0$)," *J. Solid State Chem.*, **63**, 237-49 (1986).
6. B. C. Tofield, C. Greaves, and B.E.F. Fender, "The $SrFeO_{2.5} – SrFeO_{3.0}$ system. Evidence of a new fase $Sr_4Fe_4O_{11}$ ($SrFeO_{2.75}$)," *Mat. Res. Bull.*, **10**, 737-46 (1975).
7. M. Takano, T. Okita, N. Nakamaya, Y. Bando, Y. Takeda, O. Yamamoto, and J.B Goodenough, "Dependence of the structure and electronic state of $SrFeO_x$ ($2.5 < x < 3.0$) on composition and temperature," *J. Solid State Chem.*, **73**, 140-50 (1988).
8. J. Mizusaki, M. Okayasa, S. Yamauchi, and K. Fueki, "Nonstoichiometry and phase relationship of the $SrFeO_{2.5} – SrFeO_{3.0}$ system at high temperature," *J. Solid State Chem.*, **99**, 166-72 (1992).
9. J-C. Grenier, N. Ea, M. Pouchard, and P. Hagenmüller, "Structural transitions at high temperature in $Sr_2Fe_2O_5$," *J. Solid State Chem.*, **58**, 243-52 (1985).
10. V.V. Vashuk, S.A. Prodan, M.V. Zinkevich, and O.P. Ol'shevskaya, "Oxygen nonstoichiometry in double strontium-cobalt oxide," *Inorg. Mater.*, **29**, 550-53 (1993).
11. W.T.A. Harrison, S.L. Hegwood, and A.J. Jacobsen, "A powder neutron diffraction determination of the structure $Sr_6Co_5O_{15}$, formerly described as the low-temperature hexagonal form of $SrCoO_{3-x}$," *J. Chem. Soc. Chem. Commun.*, 1953-54 (1995).

12. V.V Vashook, M.V. Zinkevich, and Yu.G. Zonov, "Phase relations in oxygen-deficient $SrCoO_{2.5-\delta}$," *Solid State Ionics*, **116**, 129-38 (1999).
13. Y. Takeda, R. Kanno, T. Takada, O. Yamamoto, M. Takano, and Y. Bando, "Phase relation and oxygen nonstoichiomtry of perovskite-like compound $SrCoO_x$ ($2.29 < x < 2.80$)," *Z. Anorg. Allg. Chem.*, **540/541**, 259-70 (1986).
14. V.V. Vashook, M.V. Zinkevich, H. Ullmann, J. Paulsen, N. Trofimenko, and K. Teske, "Oxygen non-stoichiometry and electrical conductivity of the binary strontium cobalt oxide $SrCoO_x$," *Solid State Ionics*, **99**, 23-32 (1997).
15. P. Batti, "Diagramma d'equilibrio del sistema $SrO\text{-}Fe_2O_3$," *Ann. Chim. (Rome)*, **52**, 941-61 (1962).
16. F. Kanamaru, M. Shimada, and M. Koizumi, "Crystallographic properties of and Mössbauer effect in $Sr_4Fe_6O_{13}$," *J. Phys. Chem. Solids*, **33**, 1169-71 (1972).
17. A. Fossdal, L. Sagdahl, M.-A. Einarsrud, and T. Grande, *In preparation.*
18. R.D. Shannon and C.T. Prewitt, "Effective ionic radii in oxides and fluorides", *Acta Cryst.*, **B25**, 925-46 (1969).
19. R.M. German, "Sintering theory and practice," John Wiley & Sons, New York, 1996.
20. C. Greaves, A.J. Jacobsen, B.C. Tofield, and B.E.F. Fender, "A powder neutron diffraction investigation of nuclear and magnetic structure of $Sr_2Fe_2O_5$," *Acta Cryst.* **B31**, 641-46 (1975).
21. K. Kleveland, M.-A. Einarsrud, and T. Grande, "Sintering of $LaCoO_3$ based ceramics," *J. Eur. Ceram. Soc.*, **20**, 185-193 (1999).
22. R.M. German and K.S. Churn, "Sintering atmosphere effects on the ductility of W-Ni-Fe heavy metals", *Met. Trans. A*, **15A**, 747-54 (1984).
23. M. Aukrust and A. Muan, "Thermodynamic properties of solid solutions with spinel-type structure. I," *Trans. AIME*, **230**, 378-82 (1964).

Paper III

Journal of the American Ceramic Society Communications –*Submitted*

Compressive creep performance of $SrFeO_3$

Kjersti Kleveland, [a,b]Andrew Wereszczak, [a]Timothy P. Kirkland, Mari-Ann Einarsrud, and [c]Tor Grande

Department of Chemistry, Norwegian University of Science and Technology, 7491 Trondheim, Norway

[a]High Temperature Materials Laboratory, Oak Ridge National Laboratory, Oak Ridge TN 37831-6069, USA

[b]Present address: US Army Research Laboratory, Aberdeen Proving Ground, MD 21005, USA

[c]To whom correspondence should be addressed.

Abstract

Compressive creep performance of Sr-deficient and Sr-excess $SrFeO_{3-\delta}$ materials has been investigated in the temperature range of 800-1000°C and in the stress range of 2.5-25 MPa in air. The absolute density of the materials was 4.99 g/cm^3 and 5.25 g/cm^3, respectively, which corresponds to a porosity of about 2 and 5%. Both materials contained secondary phases due to the cation non-stoichiometry. It was found that the creep rate is faster for the Sr-deficient material than the Sr-excess material. The stress exponent is close to unity and the activation energy is 260±30 kJ/mole for both materials. The results can be explained by a cation diffusion mechanism. These results are discussed in relation to previous sintering data and the possible application of these materials as oxygen permeable membranes.

Introduction

Perovskite materials (ABO_3), like $SrFeO_{3-\delta}$ based ceramics, are promising materials for oxygen permeable membranes because of high electronic and ionic conductivity at high temperature.[1] Such membranes can either be used for oxygen production from air, or in the production of syngas ($CO+H_2$) by direct conversion of methane.[2] When a gradient in oxygen partial pressure is applied across the membrane, oxygen will spontaneously flow from the high partial pressure to the low partial pressure side. In order to increase the driving force, a pressure gradient can also be applied in addition to the chemical gradient. A self supported membrane, operating at high temperatures for long periods of time, must have a high resistance to creep in order to be interesting for industrial applications. An earlier study on sintering of $SrFeO_{3-\delta}$ based ceramics has indicated high creep rates at high temperature (T>1200°C).[3] After densification large expansion of the materials was observed. The expansion was due to chemical equilibria producing oxygen gas building up a gas pressure inside the pores. These observations were the motivation for investigating creep behavior of $SrFeO_{3-\delta}$ based ceramics. Sr-deficient and a Sr-excess $SrFeO_{3-\delta}$ materials were chosen for this study in order to relate the results to the observations in the previous sintering experiments.

Few studies on creep behavior on related perovskites have been reported. Majkic et al.[4] investigated the compressive creep behavior of $SrCo_{0.8}Fe_{0.2}O_{3-\delta}$ in the temperature range 850-975°C and found that the creep mechanism was dependent on both stress and temperature. In the low stress range they reported a stress exponent of 1.1-1.3, while at higher stresses the exponents were higher (2.2-2.9) and temperature dependent. The activation energy was 457 kJ/mole below 925°C and 268 kJ/mole above 925°C. The difference in activation energy was attributed to a shift between diffusion of A and B cations as the rate controlling specie. An alternative explanation could be that the shift in mechanism is related to phase transitions in the material similar to the decomposition of $SrCoO_{3-\delta}$ to $Sr_6Co_5O_{15}$ and Co_3O_4 below 800-900°C.[5,6]

Cook et al.[7] measured creep of $(La_{1-x}Sr_x)_{1-y}MnO_{3+\delta}$ as a function of oxygen partial pressure and Sr-concentration at 1250°C. They found that the material deformed by grain boundary sliding and lattice diffusion. Depending on oxygen partial pressure and Sr concentration either diffusion of oxygen ions or cations was rate controlling for creep. Only for A-site deficiency and high oxygen partial pressure did the oxygen vacancies control creep, otherwise the cations were rate controlling.

Experimental

Materials

Two $SrFeO_{3-\delta}$ materials with two different Sr/Fe ratios were tested, a Sr-excess material (Sr/Fe=1.05) and a Sr-deficient material (Sr/Fe=0.95). In the following the two compositions are referred to as SF-1.05 and SF-0.95, respectively.

The materials tested in this study were prepared by sintering of submicron powders of $SrFeO_{3-\delta}$. The powders were prepared by spray drying (Mini Spray Dryer B-191, Büchi) of a solution of nitrates and acetates. The chemical composition (±1 at%) of the powders was determined by thermogravimetrical analysis of the chemicals used. The total cation concentration of the solutions was approximately 0.5 M. The spray dried powders were slowly heated to 250°C, kept there for 24 h and further heated to around 600°C where organic residues were burnt off during 24 h. The powders were further ball milled (Si_3N_4-balls) for 24 h in iso-propanol. The milled powders were calcined at 750-800°C for 8 h in flowing synthetic air and further ball milled for 24 h. In order to improve the flow properties the powders were sieved (150 μm) before pressing. The powders were single phase according to X-ray diffraction, consistent with the considerable solid solubility reported for $SrFeO_{3-\delta}$.

Cylinders (4 g) were first uniaxially pressed (double action) at ~10 MPa and canned in latex membranes subjected to vacuum before they were cold isostatically pressed at 200 MPa. The relative green density obtained was ~55% of theoretical. The cylinders were sintered at 1100°C in air for 6 h (SF-1.05) or 24 h (SF-0.95) with a heating rate of 200 °C/h and a cooling rate of 50 °C/h.

X-ray powder diffraction (XRD) of powders and crushed sintered samples were performed on a Siemens D5005 diffractometer (CuKα radiation) in the 2θ range 20-90° with a 0.040° step and step time 6.0 s. Microstructural analysis was performed using an optical microscope (Reichert-Jung, MeF3-metallograph) coupled to a digital camera (Sony DKC-5000).

Prior to the creep measurements the specimens were adjusted by grinding the end surfaces of the cylinders to obtain parallel ends. Specimen dimensions were 16 mm in length and 7.5 mm in diameter. A length/diameter ratio of around 2 was chosen as a compromise in order to minimize the likelihood of buckling and barreling during creep tests.[8]

Mechanical testing

The setup for the compression creep tests is shown in Fig. 1. The load train consisted of two fully dense high purity alumina push-rods attached to water cooled grips in a servo-hydraulic test machine (Instron 1380). The cylindrical test specimen was compressed between the free, axially-aligned, flat and parallel ends of the alumina push-rods. The specimen and the alumina push-rods were heated to the set point temperature with a short resistance-heated furnace (50 mm vertical hot zone). Two thermocouples positioned close to the specimen controlled the temperature to ±3°C. A high temperature capacitive extensometer (25 mm gage length) was used to measure the displacement of the push-rods to a resolution of ±0.2 μm during static loading creep tests. Test temperatures were 800, 850, 900, and 1000°C, and static compressive stresses varied from 2.5 to 25 MPa. The stress was increased in steps of 2.5 or 5.0 MPa up to 20-25 MPa, or until the strain reached 10%. At each step the specimens were kept at constant stress for 25-40 h depending on the creep rate. The creep rate was calculated from data points between 30 and 40 h (T≤900°C) or between 15 to 25 h (T=1000°C) for every stress level. True stresses and strains were used in calculations because the strain exceeded 5% in several experiments, and then the true and engineering strain/stress are no longer equivalent.

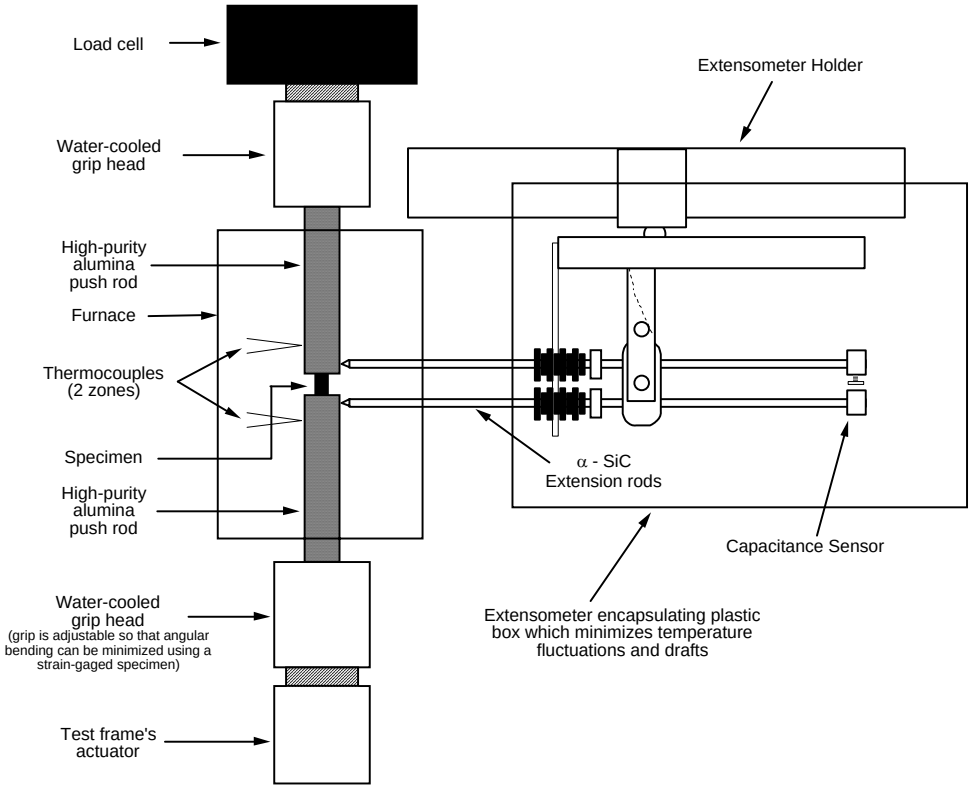

Figure 1: Schematic drawing of compression creep test. A cylindrical specimen geometry was used.

Results

XRD analysis showed that the SF-0.95 material, as expected, contained considerable amounts of the secondary phase $Sr_4Fe_6O_{13}$ due to the Sr-deficiency. The morphology of the secondary phase is plate-like grains as shown in Fig. 2a. The SF-1.05 samples contained a smaller amount of secondary phase, which could not be detected by XRD. However, optical microscopy revealed thin plates of a secondary phase assumed to be $Sr_3Fe_2O_7$ due to the Sr-excess[9], Fig. 2b. The densities of the cylinders, calculated from geometrical dimensions, were 5.25 g/cm^3 (SF-1.05) and 4.99 g/cm^3 (SF-0.95). The porosity calculated by computer image analysis of optical microscope images was 2% for SF-1.05 and 5% for SF-0.95. The apparent grain size estimated from Fig.2 was in the order of 5 μm. We could not observe any significant change in microstructure after the creep tests.

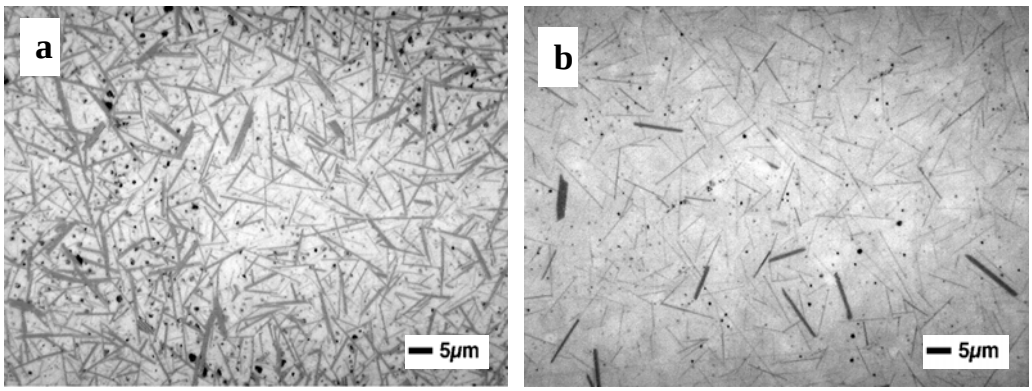

Figure 2: Optical microscope image of a) SF-1.05 and b) SF-0.95 before testing. The darker areas are secondary phase and the black spots are pores.

Typical creep curves are shown in Fig. 3, where the engineering strain versus time at 5-10 MPa is plotted for SF-1.05 at 900°C. During the initial loading the specimen deforms faster than for the following steps. The minimum creep rate was calculated from the linear region between 30 and 40 h. The power-law

Norton-Baley-Arrhenius[10] (NBA) model was used for calculating the stress exponent and the activation energy:

$$\frac{d\varepsilon}{dt} = A_{nb} \cdot \sigma^{n} \cdot \exp\left(\frac{Q}{RT}\right) \qquad (1)$$

where A_{nb} is a constant, σ is stress, n is stress exponent, Q is activation energy, R is the gas constant and T is absolute temperature. This model assumes that the rate limiting mechanism for creep is independent of temperature.

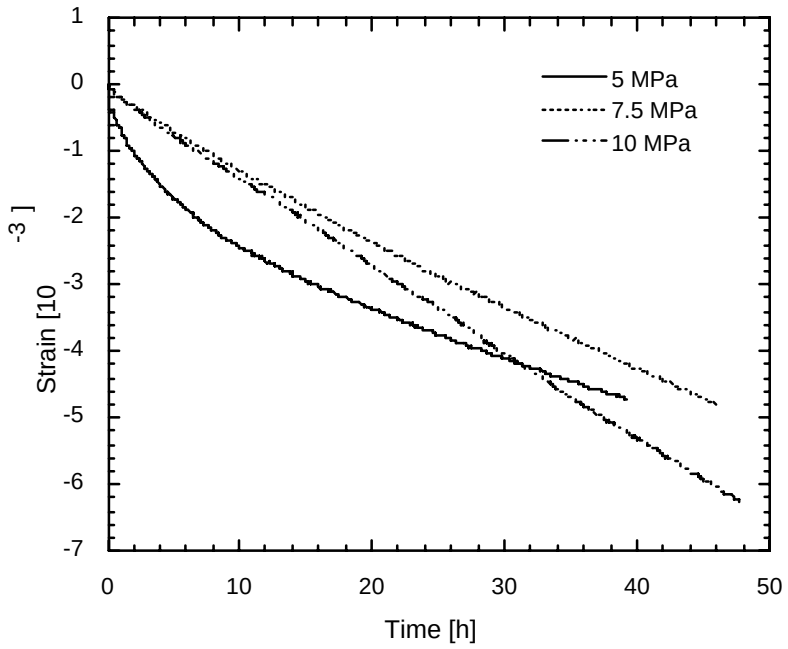

Figure 3: Engineering strain versus time for SF-1.05 at 900°C.

Table 1: Minimum creep rate as a function of temperature and true stress.

Composition	Temperature [°C]	n	Stress [MPa]	Minimum creep rate [$\times 10^{-10}$ s^{-1}]
$Sr_{1.05}FeO_3$ (SF-1.05)	800	0.6	5.2	26
			10.0	36
			15.0	50
			19.9	56
	900	1.2	5.1	185
			7.5	256
			9.9	354
			12.2	456
			14.6	582
			17.0	727
			19.2	875
	1000	0.9	2.6	1150
			3.6	1270
			4.6	1670
			5.6	1990
			6.6	2470
$Sr_{0.95}FeO_3$ (SF-0.95)	800	0.8	5.1	42
			10.2	76
			15.2	89
			20.1	112
			24.8	150
	850	1.3	5.0	77
			7.5	118
			9.9	160
			12.3	213
			14.7	264
			17.0	334
			19.3	409
	900	1.4	5.2	359
			7.6	515
			9.9	756
			12.1	983
			14.2	1360
			15.9	1710

A summary of the minimum creep rate as a function of temperature and stress, and the stress exponent for each temperature, is given in Table 1. The results show that the SF-0.95 material creeps about twice as fast as the SF-1.05 material at the same temperature. A log-log representation of minimum creep rate versus stress is shown for SF-1.05 and SF-0.95 in Fig. 4. The linear fit gives the stress exponent, n, in Eq. 1. The n-values are close to unity for all series. The activation energy was calculated by multi-linear regression of Eq. 1. The calculated activation energy is 255±15 kJ/mole for SF-1.05 and 266±32 kJ/mole for SF-0.95. (95% confidence interval).

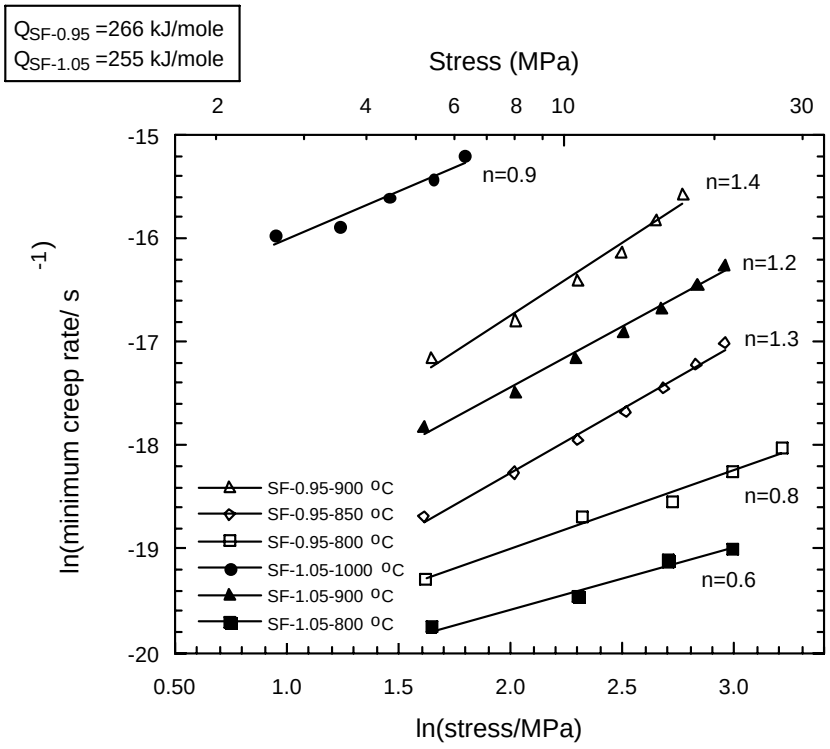

Figure 4: Log-log representation of minimum creep rate versus stress of SF-1.05 and SF-0.95 in the temperature range 800-1000°C. The slope of the linear fit gives the stress exponent, n.

The temperature compensated creep rate (TCCR) is plotted as a function of stress in Fig. 5. The TCCR was calculated by dividing both sides of Eq. 1 by the exponential temperature term {exp(-Q/RT)}. The slope of the linear fit gives the mean n-value for each composition over the whole temperature and stress range. For SF-1.05 the n-value is 0.9±0.2, and for SF-0.95 the value is 1.1±0.3 (95% confidence interval). The A_{nb}-value was 1292 and 1487 for SF-1.05 and SF-0.95, respectively.

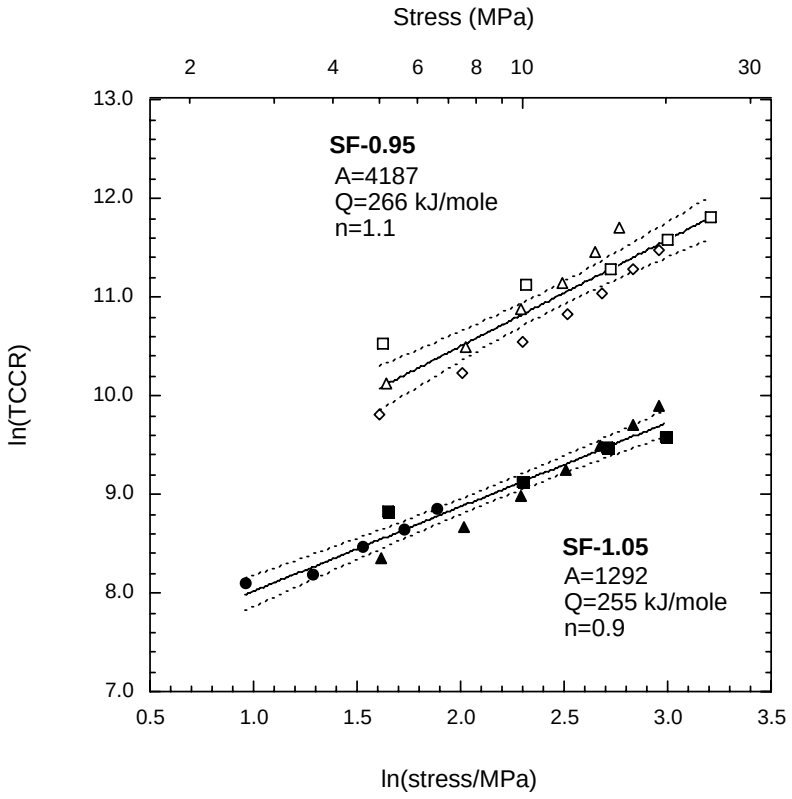

Figure 5: Temperature compensated creep rate as a function of stress for SF-1.05 and SF-0.95. The broken lines show the 95% confidence interval.

Discussion

The amount of secondary phase in the materials can be calculated from the overall cation stoichiometry. Assuming no solid solution of SrO or Fe_2O_3 in $SrFeO_{3-\delta}$, the amount of secondary phase is around 13 vol% for both SF-0.95 and SF-1.05. However, it is clear from Fig. 2 that the amount of secondary phase is larger in SF-0.95 than in SF-1.05. The difference might be related to the phase boundary for solid solution. Earlier experiments indicates that the solid solubility region for $SrFeO_{3-\delta}$ is wider at the Sr-rich side than at the Sr-deficient side of the phase diagram.[3] Since $Sr_4Fe_6O_{13}$ and $Sr_3Fe_2O_7$ have perovskite related structures, intergrowth between the $SrFeO_3$ and the secondary phase is probable. For instance, intergrowth has been reported in the SrO-TiO_2 system between different members of the $Sr_{n+1}Ti_nO_{3n+1}$ family.[11] Intergrowth has also been observed between $Sr_4Fe_6O_{13}$ and $SrFeO_3$.[12] This effect might give an improper image of the amounts of secondary phase through the optical microscope. The secondary phases are also expected to affect the creep behavior of the material. The complex microstructure of the materials makes it more difficult to interpret the creep behavior, and single phase materials with varying grain size would have been better for the determination of mechanism. It should be noted that the materials were chosen for comparison with previous sintering studies.

The theoretical densities of the materials are unknown because of the secondary phases, solid solution, and an unknown oxygen stoichiometry. The oxygen content in both the primary and secondary phases is dependent on both temperature and diffusion of oxygen, and thereby on the cooling rate. The perovskite phase $SrFeO_{2.73}$ has a density of 5.38 g/cm^3, and the secondary phases $Sr_3Fe_2O_{6.75}$ and $Sr_4Fe_6O_{13}$ have densities of 5.32 and 5.07 g/cm^3, respectively. Assuming 13 vol% of secondary phase present in both compositions an estimate for the density is 97.8% for SF-1.05 and 93.4% for SF-0.95. This is in fairly good agreement with a porosity of 2% for SF-1.05 and 5% for SF-0.95 calculated by computer image analysis.

Sintering experiments show that the sintering rate for SF-0.95 is slower than for SF-1.05,[3] and based on these results the expected creep rate would also be slower for SF-0.95 than for SF-1.05. However, the opposite is observed in Fig. 4. The slower sintering rate of SF-0.95 is related to formation of the secondary phase during sintering, but when a dense two-phase material is achieved the mass transport is faster. The faster creep rate for SF-0.95 material is probably related

to the large amount of $Sr_4Fe_6O_{13}$ in this material. The secondary phase has a melting point ~350°C lower than the perovskite phase, and it is therefore expected to have a higher creep rate compared to $SrFeO_3$ at the same temperature. The $Sr_3Fe_2O_7$ phase melts less than 100°C below the perovskite, and the effect of this phase is therefore expected to be less.[9]

During the initial loading of the creep tests the specimen deforms faster than for the following steps, Fig. 3, which might reflect that the primary creep is larger for the first increment than for the following. Another contribution to this effect can be that the ends of the cylinder were not completely parallel before measurement. This would make the loaded area smaller than the calculated area, and thereby the applied stress larger than the calculated stress. As the specimen creeps the loaded area will approach the calculated area, and the stress will be true after some time depending on the deviation from parallelism and the creep rate. This effect is stronger at lower temperatures since the creep rate is slower which is also in agreement with this argument.

The major part of the creep is determined by the perovskite phase. The n values calculated in Fig. 4 are close to 1 for all experiments, which indicates a diffusion controlled creep mechanism. It is not possible to conclude whether the fastest diffusion path of the slowest moving ion is through the lattice (Nabarro-Herring mechanism[13]) or through the grain boundaries (Coble mechanism[14]). In order to distinguish between the two mechanisms the grain size must be varied in order to determine the grain size exponent. It is possible that the mechanism is a combination between lattice and grain boundary diffusion. The activation energy for diffusion of oxygen in $SrFeO_{3-\delta}$ has been measured to be 54 kJ/mole.[15] It is therefore unlikely that diffusion of oxygen is rate limiting for creep. It is therefore concluded that diffusion of cations is controlling the creep rate.

A stress exponent close to unity is common for perovskite ceramics.[16] However, the reported activation energies are usually higher than what we have measured. For instance, 720 kJ/mole has been reported for $BaTiO_3$.[17] For $SrCo_{0.8}Fe_{0.2}O_3$, two different values are reported; 457 kJ/mole below 925°C and 268 kJ/mole above 925°C. The lower value is close to what we have measured for $SrFeO_{3-\delta}$. We believe that the low activation energy for $SrFeO_{3-\delta}$ is related to the defect chemistry of this material. The oxygen vacancy concentration is very dependent on temperature, and the δ value approaches 0.5 around 1400°C. The change in oxygen stoichiometry versus temperature is especially large in the temperature

range 600-900°C.[18] By increasing the oxygen non-stoichiometry (δ) the molar volume of the material increases. This leads to a temperature dependent molar volume, and especially in the temperature range where these creep measurements were done. An increased molar volume with increasing temperature enhances diffusion of cations which is controlling the creep rate, and we propose that the low activation energy is related to the chemical expansion due to the reduction of the valence state of Fe.

From the results obtained here it is possible to estimate the deformation rate for a membrane in a given pressure gradient and at a certain temperature. For a SF-1.05 material at 900°C under 10 bar pressure the membrane will deform ~6% per year, and at 100 bar pressure it will deform ~45% per year according to these results. Decreasing the temperature to 800°C would have a strong effect on reducing creep, and the estimated deformation per year is only ~0.4% at 10 bar and ~3% at 100 bar.

In previous sintering experiments swelling was observed at high temperature for both SF-0.95 and SF-1.05.[3] For the SF-0.95 material swelling started at ~1220°C during heating and terminated after ~15 min. The fast swelling was related to decomposition of $Sr_4Fe_6O_{13}$ involving a liquid phase and evolution of oxygen gas creating a gas pressure inside the pores. For SF-1.05 the swelling started at ~1250°C and continued slowly at isothermal conditions at 1320°C for ~4 h. Here, swelling was also related to the secondary phase and evolution of oxygen gas inside the pores. However, only solid phases were present in this material. The expansion observed during sintering is in accordance with an extrapolated creep rate at high temperature calculated from Fig. 4. A linear expansion of ~10% during 3 h was observed at 1320°C for SF-1.05. This would correspond to a pore pressure of oxygen of ~20 bar which is realistic taking into account the proposed phase equilibrium. For SF-0.95 the expansion was much faster due to the formation of a liquid phase and thereby fast viscous flow, making the mass transport much faster.

Conclusion

Compressive creep performance of Sr-deficient (SF-0.95) and Sr-excess (SF-1.05) $SrFeO_{3-\delta}$ was investigated in the temperature range 800-1000°C and stress range 2.5-25 MPa. The creep rate for SF-0.95 is about twice as fast as for SF-1.05 at the same temperature and stress. The high creep rate for SF-0.95 is probably due to the large amount of $Sr_4Fe_6O_{13}$ present in this composition. The secondary phase is expected to have a higher creep rate than the perovskite phase due to a lower melting point. The stress exponent for both compositions is close to unity suggesting a diffusion controlled mechanism. The activation energy for creep is 260±30 kJ/mole for both materials. Creep is assumed to be controlled by cation diffusion since the activation energy for diffusion of oxygen in $SrFeO_{3-\delta}$ is much lower than the measured activation energy.

References

1. V.V. Kharton, E.N. Naumovich, A.V. Nikolaev, V.V. Astashko, and A.A. Vecher, "Electrochemical properties of mixed $SrCo(Fe,Cu)O_{3-\delta}$ conductors," *Russ. J. Electrochem.*, **29**, 1201-09 (1993).
2. V.V. Kharton, E.N. Naumovich, and A.V. Nikolaev, "Materials for high-temperature oxygen membranes," *J. Membrane Science*, **111**, 149-57 (1996).
3. K. Kleveland, M.-A. Einarsrud, and T. Grande, "Sintering behavior, microstructure and phase composition of $Sr(Fe, Co)O_{3-\delta}$ ceramics", *J. Am. Ceram. Soc.*, Submitted.
4. G. Majkic, L. Wheeler and K. Salma, "Characterization of creep behavior of $SrCe_{0.8}Fe_{0.2}O_{3-x}$,", *Mat. Res., Symp., Proc.*, **575,** 349-54 (2000).
5. Y. Takeda, R. Kanno, T. Takada, and O. Yamamoto, "Phase relation and oxygen-non-stoichiometry of perovskite-like compound $SrCoO_x$ ($2.29<x<2.80$)", *Z. Anorg. Allg. Chem.*, **540/541**, 259-70 (1986).
6. W. T. Harrison, S.L Hegwood, and A.J. Jacobson, "A powder neutron diffraction determination of the structure of $Sr_6Co_5O_{15}$, formerly described as the low-temperature hexagonal form of $SrFeO_{3-x}$", *J. Chem. Soc., Chem. Commun.*, 1953-54 (1995).
7. R.E. Cook, K.C. Goretta, J. Wolfenstine, P. Nash, and J.L. Routbort, "High-temperature deformation and defect chemistry of $(La_{1-x}Sr_x)_{1-y}MnO_{3+\delta}$," *Acta Mater.*, **47**, 2969-80 (1999).

8. J.M. Birch, B. Wilshire, D.J.R. Owen, and D. Shantaram, "The influence of stress distribution on the deformation and fracture behavior of ceramic materials under compression creep conditions", *J. Mat. Sci*. **33**, 1817-25 (1976).
9. P. Batti, "Diagramme d'equilibrio del sistema SrO-Fe_2O_3", *Ann. Chim. (Rome)*, **52**, 941-61 (1962).
10. F.H. Norton, The creep of steel at high temperature, McGraw Hill, New York, 1929.
11. R.J.D Tilley, "An electron microscope study of perovskite-related oxides in the Sr-Ti-O system", *J. Solid State Chem.*, **21**, 293-301 (1977).
12. A. Bardal, *Personal communications*.
13. C. Herring, "Diffusional viscosity of polycrystalline solid", *J. Appl. Phys.*, **21**, 437-45 (1950).
14. R.L. Coble, "A model for boundary diffusion controlled creep in polycrystalline materials," *J. Appl. Phys.*, **34**, 1679-82 (1963).
15. A. Holt, R. Glenne, and T. Nordby, "Defects and transport in $SrFe_{1-x}Co_xO_{3-\delta}$", *Ionics*, **5**, 434-43 (1999).
16. J.L. Routbort, K.C. Goretta, R.E. Cook, and J. Wolfestine, "Deformation of perovskite electronic ceramics – a review", *Solid State Ionics*, **129**, 53-62 (2000).
17. E.T Park, "High-temperature creep of polycrystalline $BaTiO_3$", *J. Mater. Res.*, **14**, 523-28 (1999).
18. Y. Takeda, K. Kanno, T. Takeda, O. Yamamoto, M. Takano, N. Nakayama., and Y. Bando, "Phase relation in the oxygen nonstoichiometric system, $SrFeO_x$ ($2.5 \leq x \leq 3.0$)", *J. Solid State Chem.*, **63**, 237-49 (1986).

Paper IV

Journal of the American Ceramic Society - *Submitted*.

Non-elastic behavior of $LaCoO_3$-based ceramics

Kjersti Kleveland, Nina Orlovskaya, Tor Grande, Anne Marie Mardal Moe, and Mari-Ann Einarsrud*

Department of Chemistry, Norwegian University of Science and Technology, N-7491 Trondheim, Norway

Kristin Breder, Oak Ridge National Laboratory, Oak Ridge, TN, USA
Present address: Saint-Gobain Abrasives, Higgins Grinding Technology Center, Worcester, MA, USA

George Gogotsi, Institute for Problems of Strength, National Academy of Sciences of Ukraine, 2 Timiryazevskaya St., Kiev, Ukraine

*To whom correspondence should be addressed.

Abstract

The mechanical properties of phase pure $LaCoO_3$ and $La_{0.8}Ca_{0.2}CoO_3$ have been investigated in the temperature interval 25-800°C. Both compositions show a non-elastic stress-strain behavior during 4-point bending experiments, and during loading-unloading cycles hysteresis loops are observed. Residual strain is stored in the material after loading, and a mechanism related to ferroelastic domain switching in the rhombohedral perovskite is proposed. Fracture toughness of $La_{0.8}Ca_{0.2}CoO_3$ measured by SENB and SEVNB methods coincide and are equal to 2.2 $MPa \cdot m^{1/2}$ at RT and decreases to around 1 $MPa \cdot m^{1/2}$ at 300-800°C. A decrease in fracture toughness is consistent with a ferroelastic behavior as the rhombohedral distortion decreases with increasing temperature.

I. Introduction

Monolithic ceramic materials are usually brittle and deform elastically under stress. However, a particular type of ceramics, which shows non-elastic behavior, has been termed ferroelastic by analogy with the stress-strain relationship with the polarisation of ferroelectric materials in an electrical field or the magnetization of ferromagnetic materials in magnetic fields.[1] Such non-elastic behavior has been related to domain switching under loading. Ferroelastic behavior has been observed for several ceramic materials such as tetragonal zirconia, zirconates and titanates.[2-4] Spontaneous ferroelastic strain in rhombohedral perovskites, such as $LaAlO_3$, has previously been reported by Müller et al.[5] Rhombohedral perovskites should undergo a paraelastic to ferroelastic transition when transforming from cubic to rhombohedral structures during cooling.[1] Pure $LaCoO_3$ has a rhombohedral structure at room temperature and has a significant distortion from cubic structure also at 1000°C. Extrapolating the data for rhombohedral angle, $LaCoO_3$ remains rhombohedral up to temperatures close to the melting point.[6-8] At 50 mol% substitution of Sr for La, the crystal structure becomes cubic.[9,10] At moderate substitution levels of Ca or Sr ($x = 0.2$), the rhombohedral distortion is still significant at room temperature. The rhombohedral to cubic phase transition is observed near 950°C for the substituted materials.[11]

So far the mechanical properties of lanthanum transition metal oxide perovskites have not received much attention, in spite of the fact that the application of this type of materials in high temperature devices demands certain mechanical properties such as mechanical strength and high creep resistance. Only a few characteristics, such as bending strength and Young's modulus can be found in the literature for some selected perovskites.[12-15] The reported data on the bending strength are limited to $La_{0.9}Sr_{0.1}Ga_{0.8}Mg_{0.2}O_{3-\delta}$, $La_{0.875}Sr_{0.125}MnO_{3+\delta}$ and $La_{0.7}Sr_{0.3}Cr_{1-y}Co_yO_3$.[16-18] In our recent work,[19] selected mechanical properties of $LaCoO_3$, $La_{0.8}Sr_{0.2}CoO_3$ and $La_{0.8}Ca_{0.2}CoO_3$ materials with some amount of secondary phases were investigated. We have also observed a non-linear stress-strain relation for these materials at room temperature. The motivation for this work was therefore to further study the non-linear stress-strain behavior observed and possibly relate this behavior to ferroelasticity. Furthermore we wanted to determine the bending strength and fracture toughness of phase pure $LaCoO_3$ and $La_{0.8}Ca_{0.2}CoO_3$.

II. Experimental Procedure

Powders with the stoichiometry $LaCoO_3$ and $La_{0.8}Ca_{0.2}CoO_3$ were prepared through a wet chemical route using metal nitrates and ethylendiamine tetra acetic acid (EDTA) as a complexing agent. Stoichiometric amounts of metal nitrates were dissolved in deionized destilled water and added EDTA. The complexation took place at 80°C with a pH between 8 and 10. After drying and removal of organic residue, the powders were ball milled with Si_3N_4 balls and calcined for 15 h at 950°C for $LaCoO_3$ and 900°C for $La_{0.8}Ca_{0.2}CoO_3$. The cooling rate was 200 K/h. The powders were further ball milled and pressed into bars (6×10×55 mm^3) at a uniaxial pressure of 30 MPa followed by cold isostatic pressing at 300 MPa. $LaCoO_3$ were sintered at 1200°C for 24 h, and $La_{0.8}Ca_{0.2}CoO_3$ for 10 h or 65 h at the same temperature. The cooling rate was 25 K/h to 600°C followed by 100 K/h to room temperature.

The samples were characterized by powder x-ray diffraction (XRD) (Siemens D5005 diffractometer with Cu Kα-radiation and a secondary monochromator) and SEM (Zeiss DSM 940). Three types of ceramic surfaces were investigated: Polished surface (0.25 μm diamond), machined surface (ASTM C1161), and the same machined surface after annealing at 1100°C for 4 h. No secondary phases were observed in the powders or sintered samples. The bulk density of the ceramics was determined by Archimedes' method using isopropanol. Some characteristics of the samples are given in Table 1. The grain size for $LaCoO_3$ was somewhat larger than for $La_{0.8}Ca_{0.2}CoO_3$ and the porosity was significantly higher for $LaCoO_3$ than for the Ca-substituted samples.

Merknad [YG1]: Is this grain size or surface quality???

Table 1: Sintering time, grain size, density and porosity of the samples used for mechanical testing.

Sample	Sintering time at 1200°C	Grain size (μm)	Density (g/cm^3)	Porosity (%)
$LaCoO_3$	24 h	4-6	6.75	7.4
$La_{0.8}Ca_{0.2}CoO_3$	65 h*	3-5	6.62	1.6
$La_{0.8}Ca_{0.2}CoO_3$	10 h	1-2	6.59	2.0

* Used for high-temperature strength measurements, SEVNB method and for XRD measurements.

Stress-strain relationships and four-point bending strength (ASTM C1161) were measured for both compositions at room temperature. In addition, the bending strength of the Ca-substituted samples was measured at 600°C and 800°C. Testing at room temperature was performed in 4-point flexure 40/20 mm span in an Instron 1126 with Instron 880 control panel. The load cell was 5 kN. Displacement was measured by displacement gauge of the Tesa type, placed in contact with the specimen in the center of the span using the test fixture in Fig. 1. The displacement gauge was fixed such that it measured the displacement relative to the load points. Loading point and supports were free to roll, diameter of these were 4.9 mm. Cycling was performed by subsequently loading and unloading of the sample either up to the same maximum load or by increasing the maximum load for each cycle. The cycling was performed automatically using the control panel to avoid holding times at either zero or maximum load. All measurements were performed in displacement control, with displacement of crosshead controlled from the machine (no feed-back from the displacement gauge). The crosshead rate was normally 0.5 mm/min however, measurements were performed in the range 0.5 to 0.005 mm/min. All specimens were nominally 3×4×45 mm^3.

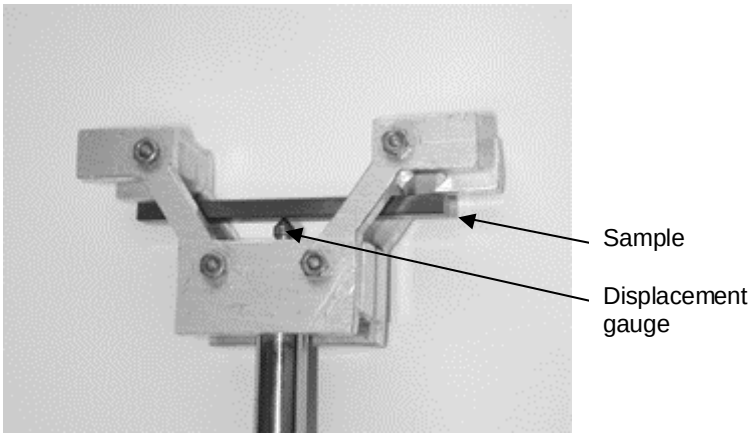

Figure 1: Sample holder for measurement of deflection during 4-point bending experiments.

Fracture toughness was determined by the Single Edge V-Notched Beam (SEVNB) method.[20-22] Rectangular bars (nominally 3×4×45 mm^3) were prenotched using a diamond blade followed by forming the V-notch by filling the preliminary notch with a diamond paste (2-7 μm grain size) and using a razor blade (100-300 μm in thickness). The notch length and radius were measured with an optical microscope and SEM. The fracture toughness measurements were performed using a 4-point bending fixture (20/40 mm geometry) using the bench "Ceramtest".[20] The crosshead speed was 0.5 mm/min. Normally two samples were recorded for each temperature.

III. Results and Discussion

Non-elastic behavior

Both the porous $LaCoO_3$ and the dense $La_{0.8}Ca_{0.2}CoO_3$ ceramics show a non-elastic stress-strain behavior during the 4-point bending experiments as can be seen in Fig. 2. Loading/unloading cycling to subsequently higher loads during 4-point bending of $La_{0.8}Ca_{0.2}CoO_3$ reveals reproducible hysteresis loops as shown in Fig. 3a. The stress-strain hysteresis curves did not depend on the loading rate within the range 0.5 to 0.005 mm/min; however, the width of the loop increases with increasing maximum load as shown in Fig. 3a. Fig. 3a shows that some residual strain is stored in the material after loading. Compared to the finite-element calculations performed by Steinkopff[23] the present results point to a ferroelastic behavior caused by domain switching of this perovskite. The rigidity of the setup was checked using a dense sintered SiC specimen and this sample showed completely elastic behavior during loading/unloading.

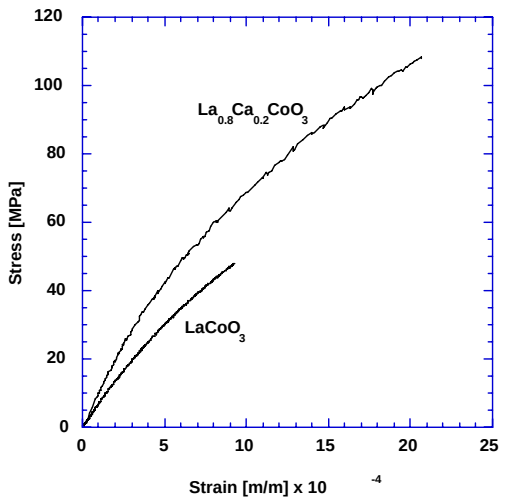

Figure 2: Stress strain relationship during 4-point bending of $LaCoO_3$ and $La_{0.8}Ca_{0.2}CoO_3$ at room temperature.

The characteristic for a ferroelastic material is an elastic hysteresis in stress-strain relation and that a permanent strain is present in the materials after unloading.[1,22] Fig. 3a shows only a part of a elastic hysteresis loop for a ferroelastic material. In order to study the complete elastic hysteresis loop caused by ferroelasticity, the material has to be subjected to pure compressive stresses followed by tensile stresses (or shear stress which allows easy reversion of the direction of loading). For the present investigation, a 4-point bending set up was used, hence the sample bar was both in tension and under compression on either side of the bar. The part of the hysteresis curves in Fig. 3a obtained during loading, will constitute a part of the complete elastic hysteresis loop for this material. However, due to the low flexure strength of these samples caused by large voids/pores we measured only the low stress part of the elastic hysteresis loop before fracture. A saturation point is expected at higher stresses. This was however, observed during loading/unloading at 600°C. At this temperature a smaller deviation from cubic structure is reported,[11] and hence the energy of domain switching is lower and the hysteresis loops are narrower.

The loading/unloading behavior was further studied by turning the sample bar upside down in the sample holder after stress-strain cycling, Fig. 3b. The surface, previously under compression, was now in tension and vice versa for the first loading/unloading cycle. As seen in Fig. 3b, the strains generated on the compressive side in the first cycle have to be overcome in the first cycle after the turning and a permanent strain is observed after the end of the first cycling. Consecutive cycles measured on the same side followed the same course as before turning the sample bar. The slope of the stress-strain curve representing the Young's modulus is smaller for the first cycle after turning compared to the following cycles, and the calculated Young's modulus for the first and second loop was 105 GPa and 115 GPa, respectively. It might be argued that the permanent strain after the first cycle might be due to microcracking, but a higher slope of the stress-strain curve for the second cycle is not consistent with such a mechanism. We therefore conclude that the permanent strain observed is due to ferroelasticity. Fett et al.[25] have previously observed a non-linear and non-symmetric stress distribution around the neutral axis in PZT ceramics during beam bending and that the tensile strains are larger than the compressive strains for the same stress level. Such behavior has also been modeled for ferroelastic materials using finite-element method.[23] The data in Fig. 3b also infer that the

stress-strain relationship is different under compression and in tension. A possible explanation for the permanent strain observed is that the domain reorientation in certain direction is facilitated under compression compared to tension. However, our observation calls for further investigations in order to completely understand the behavior.

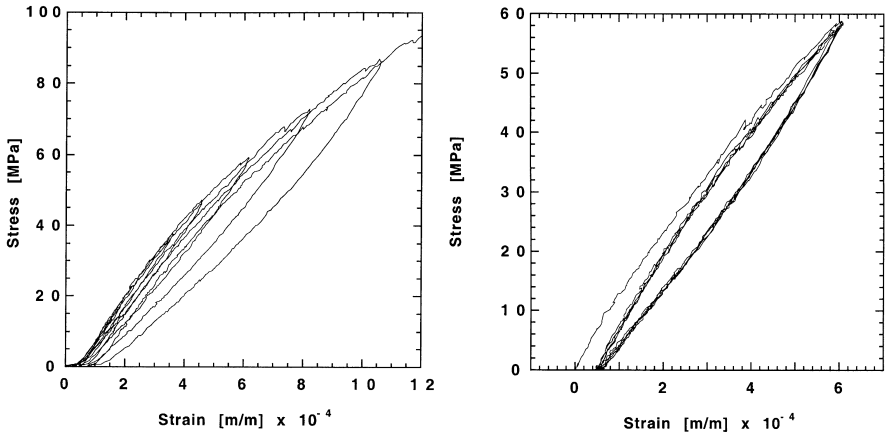

Figure 3: Cyclic 4-point bending test below the fracture stress of $La_{0.8}Ca_{0.2}CoO_3$ at room temperature. a) Six cycles up to consequtively higher loads. Sample not taken to fracture. b) A bar turned upside down after a previous test; hence the tensile surface was in compression and vice versa during the first cycle. Four cycles are shown.

XRD of ceramic surfaces with different mechanical and thermal history was carried out in order to gain additional evidence for ferroelastic behavior and domain switching. The (110) and (104) reflections of $LaCoO_3$ and $La_{0.8}Ca_{0.2}CoO_3$ from calcined powders, polished, machined and machined surface after annealing at 1100°C for 4 h are shown in Fig. 4. The intensity ratio I_{110}/I_{104} and full width at half maximum (FWHM) for all the diffractograms are summarized in Table 2. The lattice parameters and the peak intensities observed for $LaCoO_3$ powders are in good agreement with literature data.[9,10] The X-ray patterns of the powders correspond to a random orientation of domains and thereby reflect the true structure factors of the two peaks for both compositions. The intensity ratio I_{110}/I_{104} for the polished surfaces of the materials is nearly equal to the corresponding value obtained for the powders, only small texture due to preferred orientation of domains appears on the polished surfaces. The intensity ratio I_{110}/I_{104} of the machined surfaces is however significantly higher than that of the powders and polished surfaces (Table 2). The diffraction patterns clearly demonstrate that the (104) reflection decreased substantially after the mechanical treatment. The implication is that the stresses induced during machining must be in excess of the coercive stress necessary for the reorientation of the ferroelastic domains. The majority of the domains have therefore reoriented in such a way that their (001) axes are nearly parallel to the surface. As a result, the intensity of the (104) reflection decreases while the (110) intensity remains unchanged within the uncertainty. Similar effects were also observed for other reflections resulting in weakening of reflections with non-zero *l*-indexes. Significant broadening of peaks was observed for the surfaces after machining compared to polishing. The broadening is probably partly due to residual stresses and strains introduced by machining. More careful studies are necessary in order to understand the nature of the broadening of the XRD reflections.

Merknad [YG2]: See comment YG2.

The diffraction patterns of the machined surfaces after annealing at 1100°C are also shown in Fig. 4. The intensity ratio I_{110}/I_{104} of $La_{0.8}Ca_{0.2}CoO_3$ after the thermal treatment resulted in a transformation back to nearly random orientation of the domains. We therefore conclude that the ferroelastic to paraelastic transition of $La_{0.8}Ca_{0.2}CoO_3$ occurs below 1100°C which is consistent with the reported change from rhombohedral to cubic structure at approximately 950°C.[11] The intensity ratio I_{110}/I_{104} of $LaCoO_3$ did not change significantly due to the

thermal treatment at 1100°C as shown in Fig. 4a. From crystallographic data,[7,8] the rhombohedral to cubic transition of pure $LaCoO_3$ is expected to occur far above 1100°C which corresponds well with the present observation.

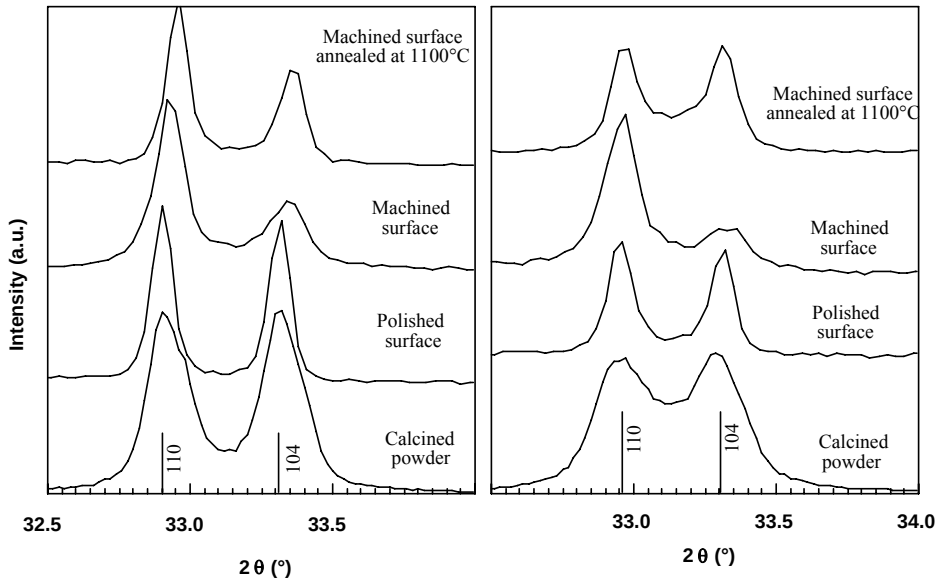

Figure 4: X-ray diffraction trace of a) $LaCoO_3$ and b) $La_{0.8}Ca_{0.2}CoO_3$ polycrystalline ceramics and powders. The two reflections shown correspond to the (110) (left) and (104) (right) reflections, respectively.

Merknad [YG3]: Mark exact peak positions (at least for the lowest curve). Also, see next comment.

Table 2: The ratio of the intensity of the (110) and (104) reflections and full width at half maximum of the (110) and (104) reflections of $LaCoO_3$ and $La_{0.8}Ca_{0.2}CoO_3$ measured by XRD.

Merknad [YG4]: (104) or (1-14)? The text and Table two show different reflections.

Sample	$LaCoO_3$			$La_{0.8}Ca_{0.2}CoO_3$		
	$I_{(110)/(104)}$	FWHM		$I_{(110)/(104)}$	FWHM	
		(110)	(104)		(110)	(104)
Calcined powder	1.01	0.1288	0.1315	1.03	0.2242	0.2154
Polished surface	1.12	0.0843	0.0869	1.21	0.1048	0.0954
Machined surface	1.88	0.1135	0.1691	4.39	0.1389	0.1961
Machined surface after annealing at 1100°C	1.83	0.0923	0.1150	0.93	0.1222	0.1333

The microstructure of $LaCoO_3$ based materials was recently investigated in TEM by Walmsley et al.[26] They found that the most prominent microstructural feature of $La_{0.8}Ca_{0.2}CoO_3$ material is the presence of twinning on {012} pseudo cube planes. On either side of twin boundaries the crystal has rhombohedral <001> axes lying in different directions. The four variants have rhombohedral axes lying parallel to the <111> directions of the high temperature cubic cell. The twin lamellas reflect the increasing rhombohedral distortion from cubic symmetry during cooling after sintering. Similar twin domains have been observed in other ferroelastic materials.[1]

Bending strength and fracture toughness

Four point bending strength of $La_{0.8}Ca_{0.2}CoO_3$ was measured to be 111±18 MPa at RT. The strength decreased with increasing temperature in accordance with our previous results.[19] The RT strength of $LaCoO_3$ was about 64±8 MPa. The fracture origin was large voids or pores for all the samples, however, the size of the voids was significantly larger for the $LaCoO_3$ samples and the porosity was also higher. The theoretical strength of $LaCoO_3$ and $La_{0.8}Ca_{0.2}CoO_3$ is expected to be relatively equal, however, $La_{0.8}Ca_{0.2}CoO_3$ to some extent stronger due to higher valance of Co. The low strength of $LaCoO_3$ is therefore reflecting the higher level of porosity and larger fracture origin size. The fracture mode was mostly transgranular for both compositions at room temperature, while mostly an intergranular mode was observed for the $La_{0.8}Ca_{0.2}CoO_3$ samples tested at elevated temperatures. The change in fracture mode with temperature indicates a weakening of the grain boundaries at elevated temperatures.

Fracture toughness of $La_{0.8}Ca_{0.2}CoO_3$ measured by the SEVNB method as a function of temperature is shown in Fig. 5. For comparison the fracture toughness of $LaCoO_3$ (SEVNB) and $La_{0.8}Ca_{0.2}CoO_3$ (SENB) measured at room temperature is included in Fig. 5. Fracture toughness of $La_{0.8}Ca_{0.2}CoO_3$ is about two times higher than the fracture toughness of pure $LaCoO_3$ (2.2 and 1.3 $MPa{\cdot}m^{1/2}$, consequently). Due to the relatively high fracture toughness of $La_{0.8}Ca_{0.2}CoO_3$ at room temperature, we propose that a toughening caused by domain reorientation is occurring as has also been reported for t´-ZrO_2.[27] The decrease in fracture toughness with increasing temperature is consistent with the decrease in rhombohedral angle for this material, however, the fracture toughness shows a faster decrease with temperature than the rhombohedral angle. The reason for the faster drop in fracture toughness needs further investigations. The fracture toughness of pure $LaCoO_3$ is significantly smaller than for $La_{0.8}Ca_{0.2}CoO_3$. The energy for domain switching is expected to be higher for $LaCoO_3$ due to a larger deviation from cubic symmetry which should increase the possibility for toughening.[7,11] The low fracture toughness for $LaCoO_3$ is therefore probably due to the high porosity in this sample.

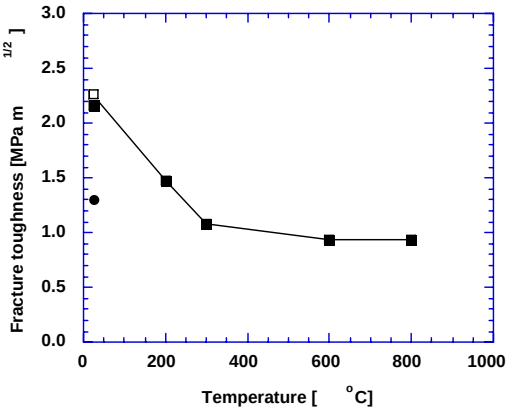

Figure 5: Fracture toughness of $La_{0.8}Ca_{0.2}CoO_3$ (ν) measured by the SEVNB as a function of temperature. The fracture toughness of $LaCoO_3$ (λ) (SEVNB) and $La_{0.8}Ca_{0.2}CoO_3$ (θ) (SENB) measured at room temperature are shown.

IV. Conclusions

Both $LaCoO_3$ and $La_{0.8}Ca_{0.2}CoO_3$ show a non-elastic stress-strain behavior during 4-point bending experiments, and hysteresis loops are formed during cycling. Residual strain is stored in the material after loading, and a mechanism related to ferroelastic domain switching in the rombohedral perovskite is proposed. XRD shows that the intensity ratio between the (110) and (104) reflections changes when the ceramic surface is machined. The implication is that the stresses induced during machining must be in excess of the coercive stress necessary for the reorientation of ferroelastic domains. The intensity ratio I_{110}/I_{104} of $La_{0.8}Ca_{0.2}CoO_3$ after the thermal treatment at 1100°C resulted in a transformation back to nearly random orientation of the domains because of crossing the ferroelastic to paraelastic transition. The bending strength for 98% dense $La_{0.8}Ca_{0.2}CoO_3$ is 111±18 MPa at RT and decreases with increasing temperature. Large pores/defects are decisive for the strength. Fracture toughness of $La_{0.8}Ca_{0.2}CoO_3$ measured by both the SENB and SEVNB methods at RT coincide and are equal to 2.2 $MPa \cdot m^{1/2}$. The fracture toughness measured by the

SEVNB method decreased to around 1 $MPa \cdot m^{1/2}$ at temperatures above 300°C. The decrease in fracture toughness is consistent with the proposed ferroelastic domain switching mechanism.

Acknowledgements

Financial support from the Research Council of Norway is appreciated.

References

1. E. K. H. Salje, *Phase transition in ferroelastic and co-elastic crystals*, Cambridge University Press, Cambridge, 1990.
2. A. V. Virkar and R. L. K. Matsumoto, "Ferroelastic domain switching as a toughening mechanism in tetragonal zirkonia", *J. Am. Ceram. Soc*., **69** [10] C 224-C 226 (1986).
3. K. Mehta and A. V. Virkar, "Fracture mechanism in ferroelectric-ferroelastic lesd zirkonate titanate (Zr:Ti=0.54:0.46) ceramics", *J. Am. Ceram. Soc*., **73** [3] 567-74 (1990).
4. F. Meschke, A. Kolleck, and G. A. Schneider, "R-curve behavior of $BaTiO_3$ due to stress-induced ferroelastic domain switching," *J. Eur. Ceram. Soc*., **17**, 1143-49 (1997).
5. K. A. Müller, W. Berlinger, and F. Waldner, "Characteristic structural phase transition in perovskite-type compounds", *Phys. Rev. Lett*., **21** [12] 814-817 (1968).
6. J.-P. Coutures, J. M. Badie, R. Berjoan, J. Coutures, R. Flamand, and A. Rouanet, "Stability and thermodynamic properties of rare earth perovskites", *High Temp. Sci*., **13**, 331-36 (1980).
7. B. Gilbu, H. Fjellvåg, and A. Kjekshus, "Properties of $LaCo_{1-t}Cr_tCoO_3$. Solid solubility, thermal expansion and structural transition", *Acta Chem. Scand*., **48**, 37-45 (1994).
8. G. Thornton, B.C. Tofield, and A.W. Hewat, "A Neutron diffraction study of $LaCoO_3$ in the temperature range $4<T<1248$ K", *J. Solid State Chem.*, **61**, 301-307 (1986).

9. A. Mineshige, M. Inaba, T. Yao, Z. Ogumi, K. Kikuchi, and M. Kawase, "Crystal structure and metal-insulator transition of $La_{1-x}Sr_xCoO_3$," *J. Solid State Chem*., **121**, 423-29 (1996).
10. R. Caciuffo, D. Rinaldi, G. Barucca, J. Mira, J. Rivas, M. A. Snaris-Rodriguez, P. G. Radaelli, D. Fiorani, and J. B. Goodenough, "Structural details and magnetic order of $La_{1-x}Sr_xCoO_3$ ($x \leq 0.3$) ", *Phys. Rev. B*, **59** [2] 1068-78 (1999).
11. M. Menon and T. Grande, to be published.
12. A. Selcuk, and A. Atkinson, "Elastic properties of ceramic oxides used in solid oxide fuel cells (SOFC)", *J. Eur. Ceram. Soc.*, **17**, 1523-32 (1997).
13. C.S. Montross, H. Yokokawa, M. Doliya, and L. Bekessy, "Mechanical properties of magnesia-doped lanthanum chromite versus temperature", *J. Am. Ceram. Soc.*, **78**, 1869-72 (1995).
14. M. Mori, H. Itoh, N. Mori, and T. Abe: "Mechanical and electrical properties of alkaline earth doped lanthanum chromites"; pp. 325-334 in *Proceedings of the 3rd International Symposium on Solid Oxide Fuel Cells*, Edited by S.C. Singhal and H. Iwahara, Electrochemical Society, Tokyo, Japan, 1997.
15. K. Li, X. Li, Ch. Lui, Zh. Zhu, J. Du, D. Hou, X. Nie, J. Zhu, and Y. Zhang, "Magnetically correlated internal friction and Young's modulus in La(Y)-Ca-Mn-O perovskites", *Phys. Rev. B.*, **56**, 13662-65 (1997).
16. J. Drennan, V. Zelizko, D. Hay, F.T. Ciacchi, S. Rajendran, and S.P.S. Badwal, "Characterization, conductivity and mechanical properties of oxygen-ion conductor $La_{0.9}Sr_{0.1}Ga_{0.8}Mg_{0.2}O_{3-x}$", *J. Mater. Chem.*, **7** [1] 79-83 (1997).
17. C.M. D'Souza and N.M. Sammes, "Mechanical properties of strontium-doped lanthanum manganite", *J. Am. Ceram. Soc.*, **83**, 47-52 (2000).
18. N.M. Sammes and R. Ratnaraj, "High temperature mechanical properties of $La_{0.7}Sr_{0.3}Cr_{1-y}Co_yO_3$ in reducing environments ", *J. Mater. Sci.*, **32**, 687-92 (1997).
19. N. Orlovskaya, K. Kleveland, T. Grande, and M. A. Einarsrud, "Mechanical properties of $LaCoO_3$ based ceramics", *J. Eur. Ceram. Soc.*, **20**, 51-56 (2000).
20. T. Nishida, Y. Hanaki, G. Pezzotti, "Effect of Notch-Root Radius on the Fracture Toughness of Fine-Grained Alumina," *J. Am. Ceram. Soc.*, **77** [6] 606-608 (1994).
21. H. Awaji, Y. Sakaida, "V-Notch technique for single-edge notched beam and Chevron notch methods," *J. Am. Ceram. Soc.*, **73** [11] 3522-23 (1990).

22. J. Kübler, "Fracture toughness using the SEVNB method: Preliminary results," *Cer. Eng. Sci. Proc.*, **18** [4] 155-162 (1997).
23. Th. Steinkopff, "Micromechanical modeling of ferroelasticity and ferroelectricity and finite-element results for nonlinear piezoelectric applications, *Ferroelectrics,* **222**, 125-129 (1999).
24. V.K. Wadhawan, "Ferroelasticity: Introductory survey and present status*", Phase Transitions,* **34**, 3-18 (1991).
25. T. Fett, D. Munz, and G. Thun, "Nonsymmetric deformation behavior of lead zirconate titanate determined in bending tests", J. Am. Cer. Soc. **81** [1] 269-72 (1998).
26. J.C. Walmsley, A. Bardal. K. Kleveland, M.-A. Einarsrud, and T. Grande, "Microstructure and the influence of spontaneous strain in $LaCoO_3$, $La_{0.8}Sr_{0.2}CoO_3$ and $La_{0.8}Ca_{0.2}CoO_3$", *J. Mater. Sci*., In print.
27. A. Foitzik, M. Stadtwald-Klenke, and M. Rühle, "Ferroelasticity of t´-ZrO_2*", Z. Metallkd.,* **84**, 397-404 (1993).

Appendix I

Journal of the European Ceramic Society 20 (2000) 51–56

Mechanical properties of $LaCoO_3$ based ceramics

Nina Orlovskaya, Kjersti Kleveland, Tor Grande, Mari-Ann Einarsrud*

Department of Inorganic Chemistry, Norwegian University of Science and Technology, 7034 Trondheim, Norway

Received 31 December 1998; received in revised form 8 March 1999; accepted 26 March 1999

Abstract

Mechanical characteristics of $LaCoO_3$ based ceramics have been measured over the temperature range from room temperature (RT) to 850°C. The bending strength is in the range of 53 MPa for 83% dense $LaCoO_3$, 76 MPa for 90% dense $La_{0.8}Sr_{0.2}CoO_3$, and 150 MPa for 99% dense $La_{0.8}Ca_{0.2}CoO_3$ ceramics at RT. The strength of $LaCoO_3$ and $La_{0.8}Sr_{0.2}CoO_3$ was relatively independent of temperature up to 850°C. The strength of the dense $La_{0.8}Ca_{0.2}CoO_3$ material decreased linearly to 850°C, where the strength at 850°C is only about 50% of the strength at RT. The fracture mode of this material is changed from fully transgranular at RT to mixed trans- and intergranular at 850°C. Hardness in the range of 7–9 GPa for 90% dense $La_{0.8}Sr_{0.2}CoO_3$ and 9–11 GPa for fully dense $La_{0.8}Ca_{0.2}CoO_3$ ceramics have been observed. The fracture toughness is calculated to be 0.73 ± 0.08 MPa $m^{1/2}$ for 90% dense $La_{0.8}Sr_{0.2}CoO_3$, and 0.98 ± 0.09 MPa $m^{1/2}$ for fully dense $La_{0.8}Ca_{0.2}CoO_3$ ceramics. Young's modulus for dense $La_{0.8}Ca_{0.2}CoO_3$ was measured to be 112 ± 3 GPa.

Keywords: $LaCoO_3$; Hardness; Mechanical properties; Strength; Toughness

1. Introduction

In recent years there has been considerable interest in perovskite oxides for application in solid oxide fuel cells (SOFC), exhaust gas sensors in automobiles, membranes for separation processes and as catalysts.[1] Important requirements for the materials for the above applications in addition to high electronic and/or ionic conductivity are stability in the temperature range and the environment of operation, as well as satisfactory mechanical properties. $LaCoO_3$ based materials are interesting for these applications due to their high electronic and ionic conductivity when La is substituted by divalent cations. $LaCoO_3$ has a perovskite-type structure with La on A-site and Co on B-site, and the oxygen stoichiometry varies with O_2 pressure and temperature. Substituting on the A-site of $LaCoO_3$ with either Sr or Ca increases the oxygen deficiency and hence increases particularly the ionic conductivity. No first order transition of pure $LaCoO_3$ has been reported. The rhombohedral distortion from cubic symmetry is linearly decreasing with increasing temperature.[2] A second order like transition related to a semiconductor to metallic "like" transition is reported at 450–650 K.[3] Sr-substituted $LaCoO_3$ becomes cubic at about 50 at% Sr.[4] The semiconductor to metallic transition temperature is decreasing with increasing Sr content.[4] A similar effect of Ca-substitution up to 20 at% has been reported by Sehlin et al.[5]

Other properties of $LaCoO_3$ based materials such as oxygen non-stoichiometry, catalytic behavior, stability and diffusion are also fairly well described.[6–9] Comparatively little research has been carried out on the mechanical properties of $LaCoO_3$ based ceramics. However, for the industrial applications of $LaCoO_3$ based materials, i.e. as oxygen separating membranes operating at 800–1000°C, knowledge of mechanical properties is necessary. The aim of the present study was therefore to prepare $LaCoO_3$, $La_{0.8}Sr_{0.2}CoO_3$ and $La_{0.8}Ca_{0.2}CoO_3$ ceramics and to measure the mechanical properties such as bending strength, hardness, fracture toughness and Young's modulus at RT and at temperatures to 850°C.

2. Experimental procedure

Powders with expected stoichiometry $LaCoO_3$, $La_{0.8}Sr_{0.2}CoO_3$ and $La_{0.8}Ca_{0.2}CoO_3$ were prepared by a

* Corresponding author. Tel.: +47-73-594002; fax: +47-73-590860.
E-mail address: mari-ann.einarsrud@chembio.ntnu.no (M.-A. Einarsrud).

0955-2219/99/$ - see front matter
PII: S0955-2219(99)00084-9

Table 1
Chemical composition, density, porosity, average grain size and secondary phases present in the densified ceramics

Sample code	Sample composition	Density (g/cm^3)	Porosity[a] (%)	Grain size (μm)	Secondary phases
$LaCoO_3$	$La_{1.077}CoO_3$	6.077 ± 0.02	16.6	2–3	La_2O_3
$La_{0.8}Ca_{0.2}CoO_3$	$La_{0.922}Ca_{0.221}CoO_3$	6.695 ± 0.03	0.15	1–2	CaO–CoO
$La_{0.8}Sr_{.2}CoO_3$	$La_{0.878}Sr_{0.199}CoO_3$	6.274 ± 0.005	9.5	2–3	$La_{2-x}Sr_xCoO_4$

[a] Calculated from the theoretical densities of the pure compounds without secondary phases.

wet chemical route using ethylenediamine tetra acetate acid (EDTA) as a complexing agent. The cations were provided from nitrate solutions and the gel formation took place at 80°C in the solution with adjusted pH (10 for La and Co and 7 when Ca and Sr were present). The concentration of the nitrate solutions used during synthesis and the stoichiometry of the synthesized powders were measured by an Atom Scan 16 ICP-AES Spectrometer (Thermo Jarrell Ash Corp.). After drying and removal of organic residue at 600°C, the powders were ball milled with Si_3N_4 balls and calcined at 850°C ($La_{0.8}Ca_{0.2}CoO_3$) or 900°C ($LaCoO_3$, $La_{0.8}Sr_{0.2}CoO_3$) for 24 h in flowing air. After calcination, the powders were further dry ball milled for 3 h and pressed into bars ($7\times10\times55$ mm^3) at uniaxial pressure of 30 MPa followed by cold isostatic pressing at 300 MPa. The bars were sintered at 1200°C for 3 h in a powder bed of $LaCoO_3$. The heating and cooling rate was set to 300 K/h and a dwell time of 2 h at 500°C during heating was included in the sintering program. The real heating rate might have been lower than the set value due to the insulating effect of the powder bed.

The bulk density of the ceramics was measured by the liquid immersion method using isopropanol. Powder X-ray diffraction (XRD) of the powders and ground ceramics was performed on a Siemens D5005 diffractometer with Cu K_α-radiation and a secondary monochromator. Microstructure of the samples was studied by SEM (Zeiss DSM 940). Grain size was measured from SEM micrographs of polished and thermally etched surfaces. After polishing to 1 μm diamonds, Vickers hardness was measured at loads up to 500 g (Digital Micro Hardness tester MX T70, Matsuzawa). Fracture toughness of $La_{0.8}Sr_{0.2}CoO_3$ and $La_{0.8}Ca_{0.2}CoO_3$ was calculated after indentation tests at 300 g force, when cracks appeared at the impression corners.[10] Four-point bending strength of the machined (Mil STD 1942B) specimens was determined at RT, 650 and 850°C using an inner span of 20 mm and an outer span of 40 mm and a heating rate of 15–25 K/min. Specimen dimensions were approximately $4\times5.5\times43$ mm^3 and normally 4 to 5 bars were tested for each composition and temperature. Young's modulus was determined at room temperature by measuring the deflection of samples during 4-point bending tests according to the ASTM 855-90 standard. All the measurements were performed in air.

3. Results and discussion

3.1. Characterization of $LaCoO_3$ based ceramics

The chemical analysis of the calcined powders included in Table 1 showed a deviation in the stoichiometry from the expected value due to an error introduced during the standardization of the nitrate solutions. For simplicity we will hereafter refer to the samples as $LaCoO_3$, $La_{0.8}Sr_{0.2}CoO_3$ and $La_{0.8}Ca_{0.2}CoO_3$ despite the known non-stoichiometry. The grain size of all the three powders was in the same range (0.2–0.5 μm) after calcination and all the three powders appeared single phase by XRD. From XRD patterns, the Sr-substituted sintered ceramics contained some $La_{2-x}Sr_xCoO_4$ as secondary phase, the Ca-substituted ceramics contained small amounts of CaO–CoO(ss) secondary phase while La_2O_3 was observed in $LaCoO_3$. The density of the

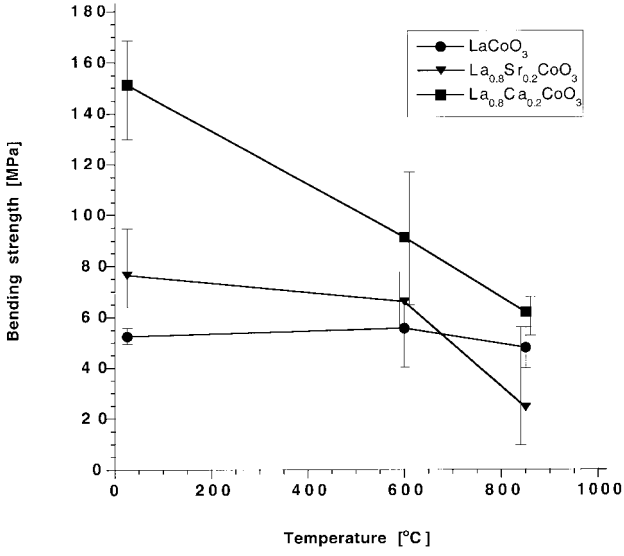

Fig. 1. Bending strength of $LaCoO_3$, $La_{0.8}Sr_{0.2}CoO_3$ and $La_{0.8}Ca_{0.2}CoO_3$ ceramics as a function of temperature. The error bars shows the maximum and minimum in strength obtained for each composition and temperature.

ceramics after sintering at 1200°C for 3 h as well as the average grain size of materials are included in Table 1.

3.2. Strength

The bending strength of the three different materials as a function of temperature is shown in Fig. 1. Dense $La_{0.8}Ca_{0.2}CoO_3$ has a bending strength of 150 MPa whereas the more porous $La_{0.8}Sr_{0.2}CoO_3$ and $LaCoO_3$ have lower values of 76 and 53 MPa, respectively. Balachandran et al.[11] reported a flexural strength of 120.4 ± 6.8 MPa for a sample with 7% porosity and stoichiometry close to $La_{0.25}Sr_{0.8}Fe_{0.6}Co_{0.4}O_x$, which is comparable to our strength data. For $LaCoO_3$ and $La_{0.8}Sr_{0.2}CoO_3$ which are both quite porous, the strength shows only a small decrease with increasing temperature up to 850°C. However, a linear decrease in bending strength to about 50% was observed for $La_{0.8}Ca_{0.2}CoO_3$ when increasing the temperature to 850°C. The fracture surface of $La_{0.8}Ca_{0.2}CoO_3$ ceramics shows a transgranular fracture mode at RT [Fig. 2(a)], while at high temperature the character of the fracture changes and both inter- and transgranular fracture exist [Fig. 2(b) and (c)]. In the two porous samples ($LaCoO_3$ and $La_{0.8}Sr_{0.2}CoO_3$), both inter- and transgranular fracture modes were observed independent of temperature. The observed decrease in strength for $La_{0.8}Ca_{0.2}CoO_3$ with increasing temperature is probably due to a reaction between the perovskite and secondary CaO–CoO(ss) (Table 2) during the reheating of the samples during testing. $La_{0.8}Ca_{0.2}CoO_3$ and CaO are not co-existing phases below 1026°C.[12,13] The formation of a secondary phase was observed on some parts of the fracture surface after high temperature testing and this phase is most probably $Ca_3Co_2O_6$ which is a stable phase in the CaO–CoO system in air.[13] Interfacial segregation to the grain boundaries might be another reason for the observed decrease in strength and change in fracture mode for $La_{0.8}Ca_{0.2}CoO_3$.[14] Fracture origin in most of the samples were large pores (voids) (20 to 200 μm) located near the surface of the specimens or large grains of secondary phases, i.e. CaO for Ca-substituted material

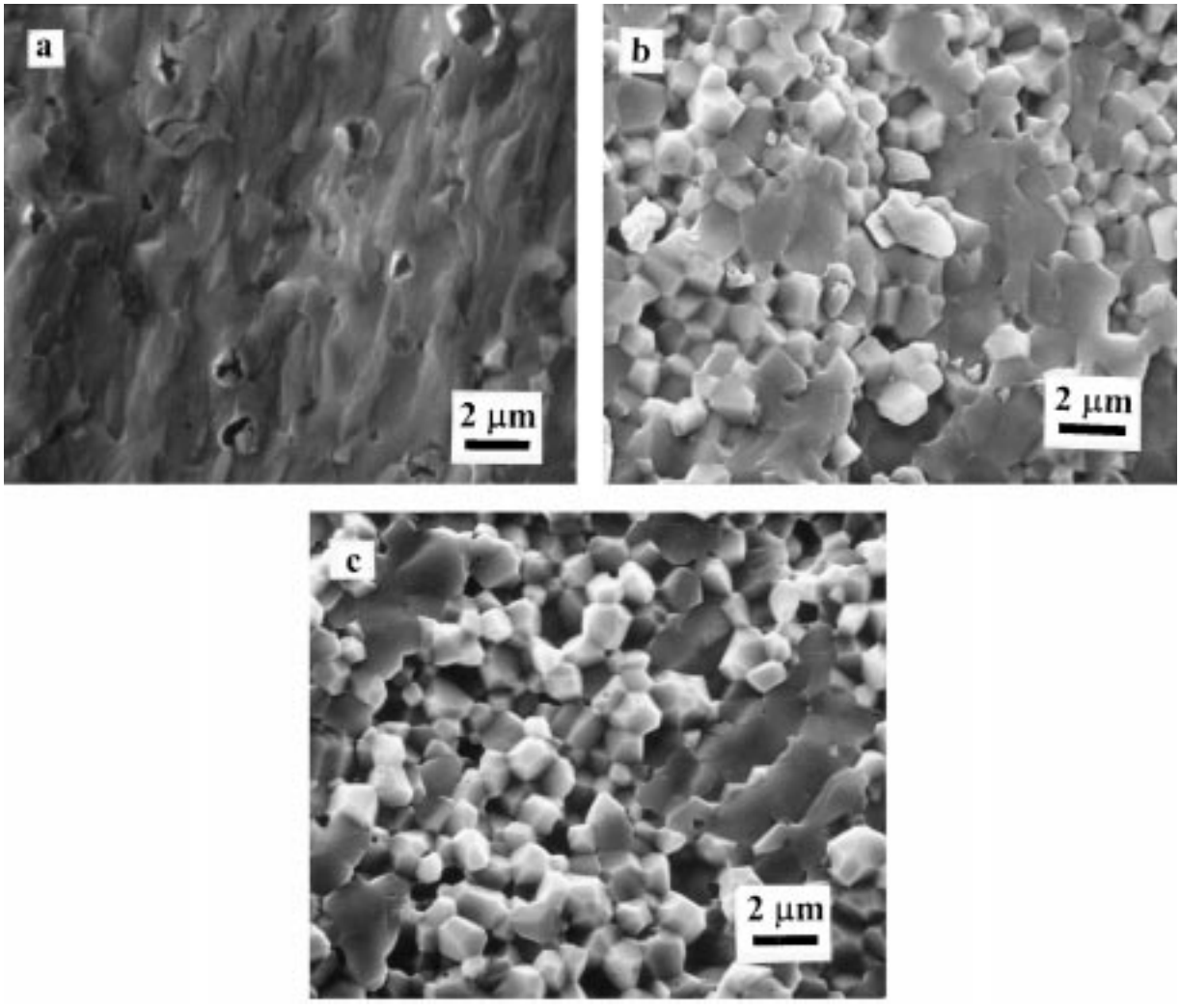

Fig. 2. Fracture surfaces of $La_{0.8}Ca_{0.2}CoO_3$ ceramics at (a) RT; (b) 600°C and (c) 850°C.

(Fig. 3). The large pores were originating from the green body preparation. A decrease in strength is also observed for phase pure La based chromites heated above 500°C by Mori et al.[15] and Montross et al.[16] The knowledge of the noticeable decrease in strength at temperatures interesting for applications is important, i.e. for the design of membranes for oxygen separation.

3.3. Hardness and fracture toughness

The hardness as function of applied load for $La_{0.8}Sr_{0.2}CoO_3$ and $La_{0.8}Ca_{0.2}CoO_3$ ceramics is shown in Fig. 4. Some softening effect can be seen for the hardness values at low loads for $La_{0.8}Sr_{0.2}CoO_3$. However, due to high scattering of hardness data at low load, it is difficult to obtain the exact number. It should be noticed that the hardness value is dependent on the porosity of the materials,[17] and is equal to 7–9 GPa for $La_{0.8}Sr_{0.2}CoO_3$ with 10% porosity and 9–11 GPa for dense $La_{0.8}Ca_{0.2}CoO_3$ material. The first cracks after indentation appeared at 300 g loading which is an indirect indication of the very brittle nature of $LaCoO_3$ based ceramics. The fracture toughness for $La_{0.8}Sr_{0.2}CoO_3$ and $La_{0.8}Ca_{0.2}CoO_3$ was calculated from indentation measurement.[10] A value of 0.73 ± 0.08 MPa $m^{1/2}$ was obtained for $La_{0.8}Sr_{0.2}CoO_3$ and 0.98 ± 0.09 MPa $m^{1/2}$ for $La_{0.8}Ca_{0.2}CoO_3$ which is in good agreement with the fracture toughness of $BaTiO_3$ of 1.0 MPa $m^{1/2}$.[18] The typical Vickers impression of $La_{0.8}Sr_{0.2}CoO_3$ ceramics is shown in Fig. 5. As can be seen, the ratio $c/a > 2.0$, where c is the crack length and a is the indentation half diagonal, suggesting that the type of cracks after indentation is a median or a half-penny type.

3.4. Young's modulus

The Young's moduli of the tested specimens are shown in Table 2 which also includes calculated Young's moduli of 100% dense samples assuming the same relative E-modulus to porosity behavior of these samples as $CaTiO_3$ ceramics previously reported in the literature.[19] This relative Young's modulus to porosity behavior fits well with a theoretical model published by Boccaccini and Fan,[20] where a porous material can be treated as a special case of a two-phase composite with the Young's modulus of one phase (pore) is equal to zero. The Young's moduli of 100% dense samples calculated using the model presented by Selcuk and

Table 2
The measured E-modulus of the tested specimens at room temperature and the E-modulus calculated for 100% dense materials using the theory of Boccacini and Fan[16] and Seluk and Atkinson[17]

Composition	Measured Young's modulus (GPa)	Estimated Young's modulus 100% density[16] (Gpa)	Estimated Young's modulus 100% density[17] (GPa)
$LaCoO_3$	47.8 ± 7.8	78 ± 3	83 ± 3
$La_{0.8}Ca_{0.2}CoO_3$	111.5 ± 2.8	112 ± 3	112 ± 3
$La_{0.8}Sr_{0.2}CoO_3$	64.4 ± 9.4	87 ± 13	86 ± 13

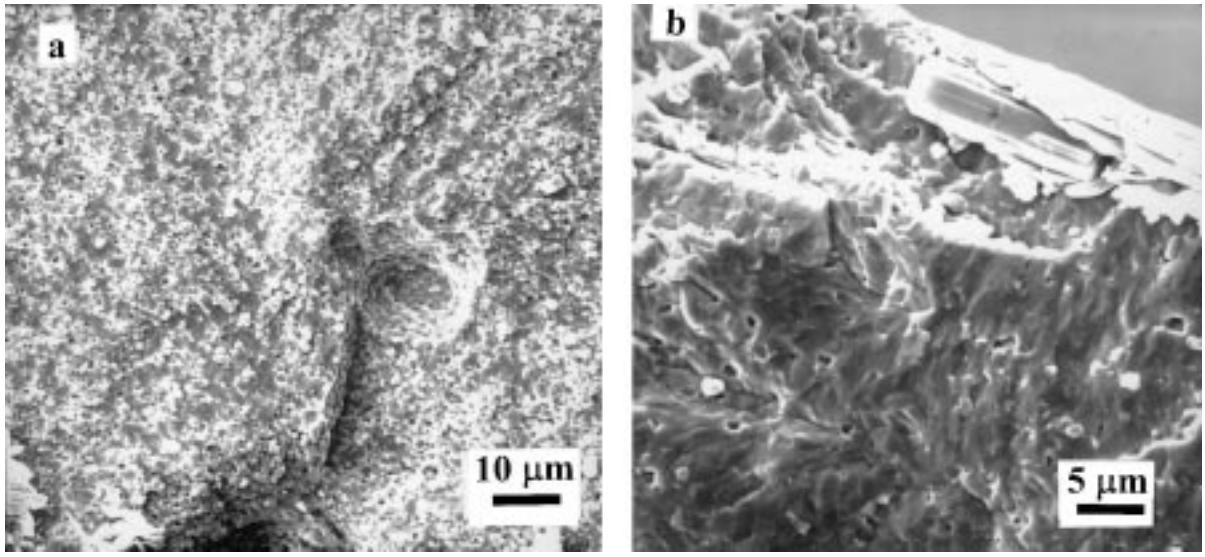

Fig. 3. Fracture origins of $La_{0.8}Ca_{0.2}CoO_3$ ceramics: (a) void and (b) CaO crystal.

Atkinson[21] assuming a Poisson's ratio of 0.3 is also given in Table 2. There is an excellent fit between the two methods for calculating Young's moduli for dense samples. To our knowledge these are the first published Young's modulus data for $LaCoO_3$-based ceramics. However, Balachandran et al.[12] have reported a Young's modulus of 124 ± 3 GPa for a sample with

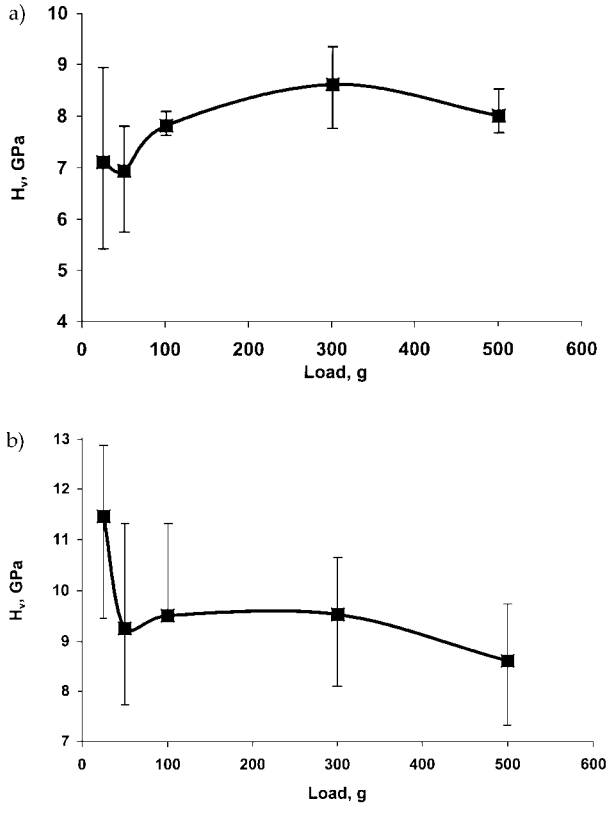

Fig. 4. Hardness of (a) $La_{0.8}Sr_{0.2}CoO_3$ and (b) $La_{0.8}Ca_{0.2}CoO_3$ ceramics as a function of load.

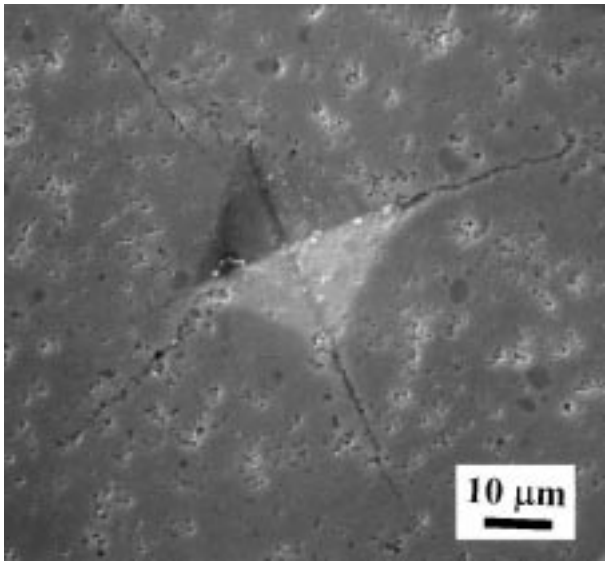

Fig. 5. Vickers impression on $La_{0.8}Sr_{0.2}CoO_3$ ceramics.

stoichiometry close to $La_{0.2}Sr_{0.8}Fe_{0.6}Co_{0.4}O_x$. Cheng et al.[22] have recently published the modulus of elasticity of $BaTiO_3$ as a function of temperature and structure. Our data for the $LaCoO_3$-based materials are in the same range as the E-modulus for $BaTiO_3$. However, it seems that the calculated values for the porous materials are somewhat underestimated. This underestimation might be due to a non-linear stress–strain behavior observed for these materials (Orlovskaya, Einarsrud, Gogotsi, Gogotsi, Grande and Moe, unpublished results) and hence the approximations used in the estimations are not completely valid. The Ca-substituted sample shows a higher Young's modulus value than the other two samples. Sr-doping of $LaCoO_3$ has been shown to reduce the rhombohedral distortion with increasing amount of Sr doping up to $La_{0.45}Sr_{0.55}CoO_3$ for which the structure becomes cubic.[4] For $BaTiO_3$ there is an increase in Young's modulus with increase in symmetry of the crystal system interrupted by a decrease close to the phase transition temperature.[22] The explanation for the increased Young's modulus for especially the Ca-substituted sample might therefore be a reduced distortion of the crystal symmetry compared to $LaCoO_3$. Also, an increase in Young's modulus is expected with increasing oxidation state of Co. Other factors like grain size[20] might also influence the Young's moduli, however, in our study the grain size of the samples was quite similar.

4. Conclusions

The bending strength is in the range of 53 MPa for 83% dense $LaCoO_3$, 76 MPa for 90% dense $La_{0.8}Sr_{0.2}CoO_3$, and 151 MPa for fully dense $La_{0.8}Ca_{0.2}CoO_3$ ceramics. For $LaCoO_3$ and $La_{0.8}Sr_{0.2}CoO_3$, the strength shows only a small decrease with increasing temperature up to 850°C. The strength of the dense $La_{0.8}Ca_{0.2}CoO_3$ ceramics linearly decreased to only approximately 50% of the strength at RT. For $La_{0.8}Ca_{0.2}CoO_3$ ceramics the fracture mode changes from fully transgranular for fracture at RT to mixed trans- and intergranular fracture after high temperature testing. Vickers microhardness is in the range of 7–9 GPa for 90% dense $La_{0.8}Sr_{0.2}CoO_3$, and 9–11 GPa for fully dense $La_{0.8}Ca_{0.2}CoO_3$ ceramics. The fracture toughness is calculated to be 0.73 ± 0.08 MPa $m^{1/2}$ for 90% dense $La_{0.8}Sr_{0.2}CoO_3$, and 0.98 ± 0.09 MPa $m^{1/2}$ for fully dense $La_{0.8}Ca_{0.2}CoO_3$ ceramics. Young's modulus for dense $La_{0.8}Ca_{0.2}CoO_3$ was measured to be 112 ± 3 GPa.

Acknowledgements

Financial support from The Research Council of Norway is highly appreciated. The microscopic investigation

at McMaster University was supported by NATO Expert Visit grant HTECH.EV 971392. We are indebted to Professor D. Wilkinson, McMaster University, Canada and Professor G. Gogotsi, The Institute of Strength Problems, Ukraine, for help with performing the bending strength measurements at elevated temperatures.

References

1. Alcock, C. B., Doshi, K. D. and Shen, Y., Perovskite electrodes for sensors. *Solid State Ionics*, 1992, **51**, 281–289.
2. Raccah, P. M. and Goodenough, J. B., First order localized-electron collective-electron transition in $LaCoO_3$. *Phys. Rev.*, 1967, **155**, 932.
3. Stølen, S., Grønvold, F. and Brinks, H., Energetics of the spin transition in $LaCoO_3$. *Phys. Rev. B*, 1997, **55**, 14103–14106.
4. Mineshige, A., Inaba, M., Yao, T. and Ogumi, Z., Crystal structure and metal–insulator transition of $La_{1-x}Sr_xCoO_3$. *J. Solid State Chem.*, 1996, **121**, 423–429.
5. Sehlin, S. R., Anderson, H. U. and Sparlin, D. M., Semiempirical model for the electrical properties of $La_{1-x}Ca_xCoO_3$. *Phys. Rev. B*, 1995, **52**, 11681–11689.
6. Mizusaki, J., Mima, Y., Yamauchi, S., Fueki, K. and Tagawa, H., Nonstoichiometry of the perovskite-type oxides $La_{1-x}Sr_xCoO_{3-\delta}$. *J. Solid State Chem.*, 1989, **80**, 102–111.
7. Islam, M. S., Cherry, M. and Winch, L. J., Defect chemistry of $LaBO_3$ (B = Al, Mn or Co) perovskite-type oxides. *J. Chem. Soc. Faraday Trans.*, 1996, **92**, 479–482.
8. Mizusaki, J., Nonstoichiometry, diffusion and electrical properties of perovskite-type oxide electrode materials. *Solid State Ionics*, 1992, **52**, 79–91.
9. Ohno, Y., Nagata, S. and Sato, N., Properties of oxides for high temperature solid electrolyte fuel cell. *Solid State Ionics*, 1983, **9/10**, 1001–1008.
10. Antis, G. R., Chantikul, P., Lawn, B. R. and Marshall, D. B., A critical evaluation of indentation techniques for measuring fracture toughness: I. Direct crack measurements. *J. Am. Ceram. Soc.*, 1981, **64**, 533–538.
11. Balachandran, U., Dusek, J. T., Sweeney, S. M., Poeppel, R. B., Mieville, R. L., Maiya, P. S., Kleefisch, M. S., Pei, S., Kobylinski, T. P., Udovich, C. A. and Bose, A. C., Methane to syngas via ceramic membranes. *Am. Ceram. Soc. Bull.*, 1995, **74**, 71–75.
12. Kleveland, K., Einarsrud, M.-A. and Grande, T., Sintering of $LaCoO_3$ based ceramics. *J. Eur. Ceram. Soc.*, in press.
13. Levin, E. M., Robbins, C. R. and McMurdie, H. F., Phase Diagrams for Ceramists. *Am. Ceram. Soc.*, 1964.
14. Desu, S. and Payne, D., Interfacial segregation in perovskites: I. theory; II. experimental evidence. *J. Am. Ceram. Soc.*, 1990, **73**(11), 3391–3406.
15. Mori, M., Itoh, H., Mori, N. and Abe, T., Mechanical, electrical properties of alkaline earth metal doped lanthanum chromites. In *Proceedings of the 3rd International Symposium on Solid Oxide Fuel Cells*, ed. S. C. Sinhal and H. Iwahara. Electrochem. Soc, Tokyo, Japan, 1993, pp. 325–334.
16. Montross, C. S., Yokokawa, H., Dokiya, M. and Bekessy, L., Mechanical properties of magnesia-doped lanthanum chromite versus temperature. *J. Am. Ceram. Soc.*, 1995, **78**, 1869–1872.
17. McColm, I. J., *Ceramic Hardness*. Plenum Press, New York, 1990.
18. Blamey, J. M. and Parry, T. V., The effect of processing variables on the mechanical and electrical properties of barium titanate positive-temperature-coefficient-of-resistance ceramics. *J. Mater. Sci.*, 1993, **28**, 4317–4324.
19. Jauch, U., Zur Thermoschockbest-ndigkeit mehrphasiger Werkstoffe. *Ber. KfK Karlsruhe*, 1989, 4469.
20. Boccacchini, A. R. and Fan, Z., A new approach for the Young's modulus–porosity correlation of ceramic materials. *Ceramics Int.*, 1997, **23**, 239–245.
21. Selcuk, A. and Atkinson, A., Elastic properties of ceramic oxides used in solid oxide fuel cells (SOFC). *J. Eur. Ceram. Soc.*, 1997, **17**, 1523–1532.
22. Cheng, B. L., Gabbay, M., Duffy, W. Jr. and Fantozzi, G., Mechanical loss and Young's modulus associated with phase transitions in barium titanate based ceramics. *J. Mater. Sci.*, 1996, **31**, 4951–4955.

Appendix II

Journal of Materials Science - *Accepted*

Microstructure and the influence of spontaneous strain in $LaCoO_3$, $La_{0.8}Sr_{0.2}CoO_3$, and $La_{0.8}Ca_{0.2}CoO_3$

J.C.WALMSLEY and A.BARDAL

SINTEF Materials Technology, N-7465 Trondheim, Norway.

K.KLEVELAND, M.-A.EINARSRUD, and T.GRANDE

Department of Chemistry, Norwegian University of Science and Technology, N-7491 Trondheim, Norway.

Abstract

Transmission Electron Microscopy has been conducted on rhombohedral perovskite oxides with composition $LaCoO_3$, $La_{0.8}Sr_{0.2}CoO_3$, and $La_{0.8}Ca_{0.2}CoO_3$. Thin foils prepared within the first weeks of sintering showed macroscopic strain and a very high defect density, which included fault-related superlattice structures. Samples prepared several months after sintering, showed no significant macroscopic strain and the main defect was found to be domains due to reflection twinning in the pseudo-cube plane. The behaviour is likely to be related to accomodation of spontaneous strain arising upon cooling of the material from the sintering temperature. The presence of twin domains illustrates the lowering of lattice symmetry as compared to the ideal cubic perovskite structure, and is relevant for explaining recent observations of ferroelastic behaviour of these materials.

1. Introduction

Lanthanum cobaltites are ABO_3 perovskites in which a proportion of the A-site La cations may commonly be substituted by divalent atoms like Sr or Ca. Lanthanum cobaltites are of considerable industrial interest. They have high electrical and ionic (O^{2-}) conductivities and are considered for use as cathode materials in solid oxide fuel cells, oxygen permeable membranes and are active catalysts for oxidation of CO. Physical properties of these materials have been studied extensively [1-6]. Less attention has been paid to characterisation of the microstructure and studies have focussed on epitaxial films with a relatively high degree of substitution [7,8].

At room temperature the lanthanum cobaltites considered here belong to the rhombohedral space group $R\bar{3}c$. A tilting of the cobalt-oxygen octahedra yields a slight distortion of the ideal cubic perovskite structure along one body diagonal. Some structural data on these compounds can be found in the literature [1,4]. An effect of Sr or Ca substitution is to reduce the rhombohedral distortion. At room temperature (RT) the rhombohedral angle for $La_{1-x}Sr_xCoO_3$ falls as x increases from zero, and the structure becomes cubic for $x = 0.5$. Mineshige et al. [4] report lattice parameters of $a = 5.38$Å and $\alpha = 60.8°$ at RT for $LaCoO_3$, changing to 5.40 Å and $\alpha = 60.55°$ for a Sr substitution level of 20 %. Detailed structural data on the Ca-substituted system is not available in the literature. $LaCoO_3$ is rhombohedral up to at least 1000°C [9,10], whereas studies by Orlovskaya et al. [11] indicate that the transition to cubic symmetry is above 1100°C. The transition temperatures for $La_{0.8}Ca_{0.2}CoO_3$ and $La_{0.8}Sr_{0.2}CoO_3$ are about 950°C and 900°C, respectively [10].

The initial objective of our study was to characterise the microstructure of sintered non-substituted, Sr-substituted and Ca-substituted material in the Transmission Electron Microscope (TEM), with a focus on possible segregation and cation ordering effects. However, we made rather unexpected observations of highly defective microstructures, which are presented here and discussed in the context of the basic crystallography of the material and spontaneous strain arising from thermal stress introduced during cooling from the sintering temperature. The observations are relevant to recent observations of ferroelastic behaviour of similar materials [11].

2. Materials and methods

The powders were prepared by a wet chemical route using ethylenediamine tetra acetate acid (EDTA) as a complexing agent, and calcined at 900-1000°C for 8-72 h as described by Kleveland et al. [12]. The powders were ball milled before and after calcination. Material was sintered as cylindrical pellets, ~8 mm in diameter and 5 mm deep, at 1200°C for 24 h. After sintering the cooling rate was ~1000°C / h. One of the pellets was later annealed at 900°C for 120 h with a subsequent cooling rate of 10 °C/h. Three compositions were prepared, $LaCoO_3$, $La_{0.8}Sr_{0.2}CoO_3$, and $La_{0.8}Ca_{0.2}CoO_3$. After sintering, the densities of the materials were 98.6 % ($LaCoO_3$) and 98.8 % (substituted materials).

Because of the observations that have been made, the TEM sample preparation procedure and sequence is described precisely. The pellets were attached to a cylindrical steel mount and slices ~0.5 mm thick were cut using a diamond-impregnated cutting wheel. The first slice cut was put to one side and a second slice was cut which was expected to be more representative of the bulk material. One of the undoped pellets was damaged during initial cutting and some cracks were introduced. 3 mm diameter discs were cut from each slice using an ultrasonic disc cutter. Each slice was approximately 300 μm thick. Up to four complete discs were obtained from each slice, depending of the presence of pre-existing cracks. The discs were mechanically ground to 100-200 μm thickness using wet silicon carbide paper of #1200 grade. Discs were "dimpled" on one side using a Gatan model 656 Dimple Grinder and 4-8 μm diamond paste to a central thickness of ~35 μm. Mechanically thinned discs were ion-beam-thinned using a Gatan duo-mill operating at 3.5-4 kV and a thinning angle of ~11.5°. X-ray diffraction (XRD) was performed with a Siemens D5005 diffractometer using CuKα radiation and a secondary monochromator, in the 2θ range of 20-65° with a step time of 9.0 seconds. TEM was performed with a Philips CM30 microscope. Examination was conducted at a beam voltage of 300 kV.

3. Results

Powder XRD was done shortly after sintering and after crushing the sintered pellets. The diffractograms were consistent with single-phase $LaCoO_3$ and reported powder diffraction data, i.e. space group $R\bar{3}c$ and lattice parameters as shown in Table I. Levels of secondary phase were sufficiently low that no additional diffraction peaks were detected. SEM observations of etched surfaces also suggested low levels of secondary phases, Fig. 1, although secondary phases could have been etched away. Average grain sizes were measured as 4.8 μm for the non-substituted material, 4.0 μm for the Sr-substituted material and 2.9 μm for the Ca-substituted material.

Table 1: Summary of preparation and TEM observations

Material and measured lattice parameters (RT)	**Prepared < 1 month of sintering.**	**Prepared > 5 months after sintering.**
$LaCoO_3$ $a = 5.379$ Å, $\alpha = 60.79°$	Residual stress and cracking of sample.	No residuals stress. No superlattice. Low defect density.
$La_{0.8}Ca_{0.2}CoO_3$ $a = 5.377$ Å, $\alpha = 60.68°$	Deformation superlattice and high defect density.	
$La_{0.8}Sr_{0.2}CoO_3$ $a = 5.403$ Å, $\alpha = 60.55°$	Superlattice and defect structure stable w.r.t time.	Reflection twinning on $\{100\}_c$.
$LaCoO_3$ Annealed 900°C / 120 h	Similar to above	Similar to above
$LaCoO_3$ Cracks introduced <1 month after sintering	Not observed	No residual stress. Limited deformation superstructure in some grains.

TEM samples prepared < 1 month after sintering revealed significant residual stresses in the materials. These samples exhibited unexpected, highly defective micro-structures and diffraction patterns revealed superlattice reflections. TEM samples prepared 5 months later from the same materials showed no evidence of residual stress, and exhibited microstructures one might well have anticipated before starting the investigations. For clarity, we will first describe the "well-behaved" microstructures of the unstrained

material, prepared in the second preparation campaign. We then describe the "ill-behaved" microstructures found in samples prepared shortly after sintering.

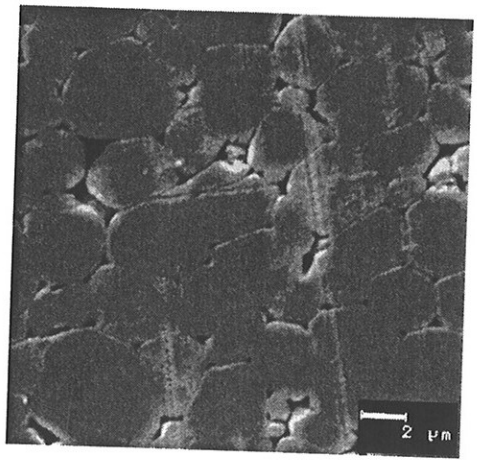

Fig. 1: SEM image of etched $LaCoO_3$ surface showing typical grain sizes

3.1. Samples with "well-behaved" microstructures-prepared 5 months after sintering

Thin foils were prepared from the original pellets approximately 5 months after the pellets were sintered. These foils were from 3 mm diameter discs that had been punched, but not ground, during the first campaign of sample preparation or from slices cut from immediately next to them. During thinning, the samples showed no evidence of distortion or relaxation of residual strain. The defect density of the material was comparatively low. With one exception (described below), there was no evidence of a superlattice in the diffraction patterns from TEM foils prepared from any of the three material compositions. Figure 2 shows a low magnification image of the typical microstructure, taken from one of the non-substituted material samples.

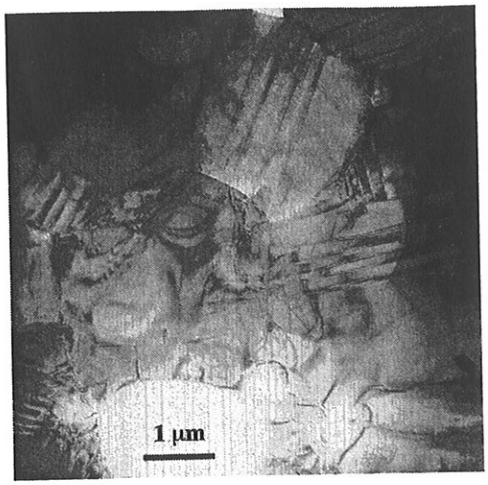

Fig. 2: Bright-field TEM image showing twin domains in most grains. The foil was prepared 5 months after sintering and exhbited "well-behaved" microstructures.

The $R\bar{3}c$ $LaCoO_3$ structure is commonly described on the basis of rhombohedral axes, defining a primitive rhombohedral cell with a rhombohedral angle α close to 60°, or equivalently on a hexagonal basis. In addition, while interpreting TEM observations, it is convenient to describe the structure as primitive pseudo-cubic. The angle between the pseudo-cube <101> directions (exactly 60° in the cubic case) then corresponds to the α angle in the rhombohedral description. In this way defects and diffraction patterns can easily be visualised in relation to both the phase transformation and the ideal, perovskite structure. Here we adapt to two indexing conventions, the pseudo-cubic (index c) and the hexagonal description of the rhombohedral cell using the Miller 3-index notation.

Twin domains were commonly observed in all three materials and they are the most obvious features evident in Fig. 2. The twin habit planes are parallel to the pseudo-cube $\{010\}_c$ planes. The twin domain boundaries are also nearly parallel to $\{100\}_c$, but exhibit some curvature. This is illustrated clearly in Fig. 3(a), where a grain is viewed along a direction near $[001]_c$ and two intersecting twin orientations are viewed edge-on. The orientation is shown in the corresponding diffraction pattern, Fig. 3(b). Some twins have a needle shaped morphology, with variable needle sharpness. The density of twin boundaries is often higher around grain edges where the intersection pattern of twin orientations can be quite complicated. Most of the twins visible in Fig. 3 lie on (100) and (010), twinning may also occur on (001), close to the plane of the foil.

The crystallography of the twins is confirmed by closer examination of diffraction patterns obtained with the selected area aperture positioned to include material on either side of one or more boundaries, Fig 3(c). While the $(0\underline{1}2)$ / $(010)_c$ systematic row is common to both sides of the boundary, it can be seen that positions of the $(\underline{1}1\underline{2})$ / $(100)_c$ reflections are separated by a small displacement along $[0\underline{1}2]$. This is consistent with performing a reflection operation in the (012) twin plane. The relationship between the alignment of planes on either side of the twin plane and the diffraction pattern is illustrated schematically in Fig. 3(d). The splitting of the $(\underline{1}1\underline{2})$ reflections arising from the crystals below and above the twin boundary reflects the lowering of symmetry during the cubic to rhombohedral phase transition. The measured angle between the $(\underline{1}1\underline{2})$ and $(\underline{1}1\underline{2})_t$ g-vectors (1.4°), and the measured difference between the length of the $(\underline{1}0\underline{4})$ and $(\underline{1}20)$ g-vectors ($2(g1-g2)/(g1+g2) = 1.2$ %) are both consistent with the XRD observations ($\alpha = 60.79°$, d_{104}=2.688 Å, d_{120}= 2.719 Å).

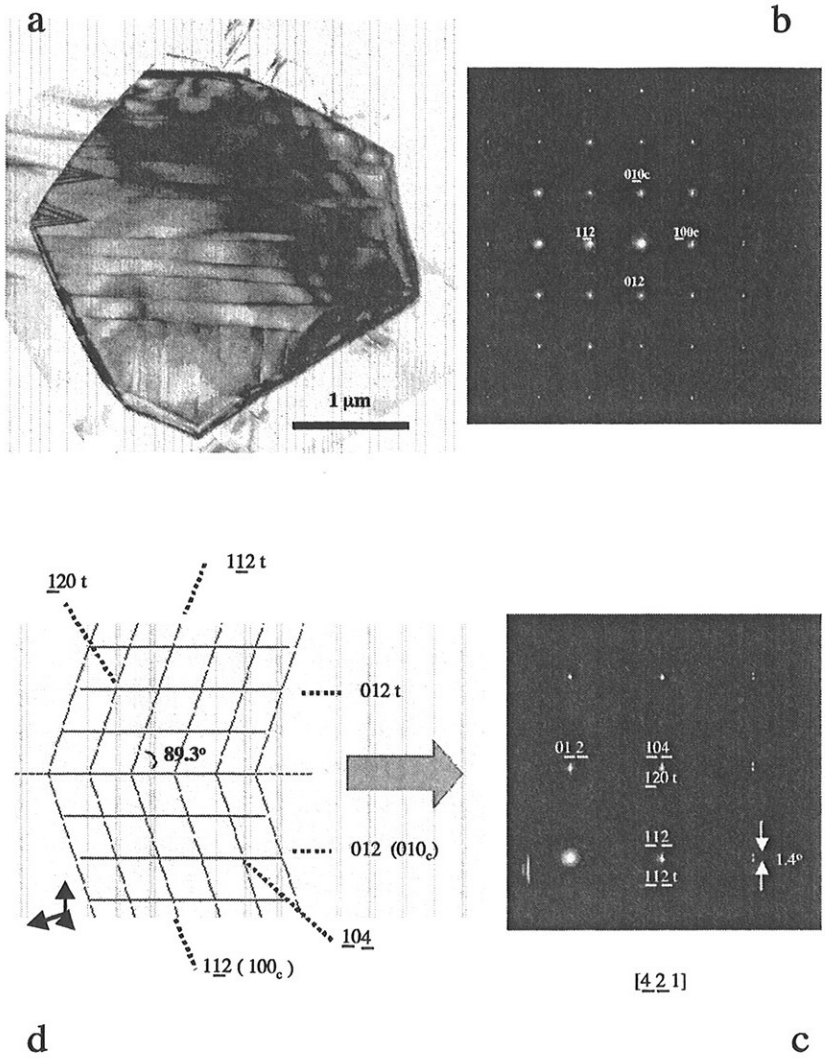

Fig. 3: Details of reflection twin domains. (a) Bright-field image showing two sets of twin orientations. (b) Selected-Area Diffraction (SAD) pattern from centre of a, with horizontal twin boundaries. (c) Larger magnification of SAD pattern showing coincidence of (0 1 2) and splitting of (1 1 2) reflections (d) Schematic drawing of crystal orientation at reflection twin boundary, with indication of some major crystal planes (dotted). The angular distortion from 90° is exaggerated in the drawing.

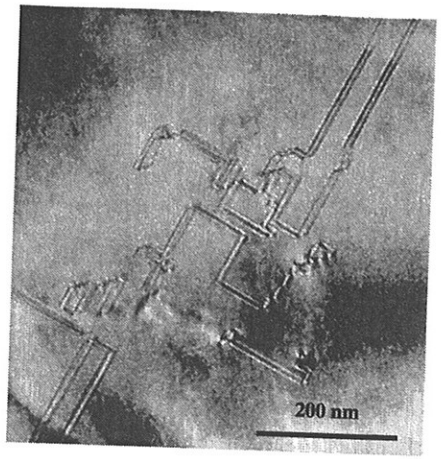

a

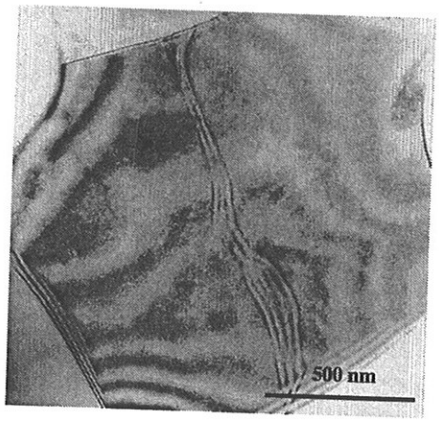

b

Fig. 4: Characteristic, but less frequently encountered planar defects, with contrast characteristic of (a) stacking-fault and (b) anti-phase boundary.

Other planar faults were observed in a small proportion of the grains examined in all three of the materials. These either had distinct {100} habit planes or irregular habit planes. Both types of morphology are illustrated in Fig. 4, having the morphological characteristics of stacking-faults and anti-phase boundaries respectively. Most of the stacking faults formed closed circuits and they often displayed a stepped morphology. Figure 4(a) shows a grain that was found to contain several closed stacking fault circuits, viewed close to a $[001]_c$ zone axis direction. It can be seen that the faults lie on $(100)_c$ and $(010)_c$, that the corners at changes of orientation are sharp and that a fine scale step structure is present at some positions. At least one section of stacking fault is not closed and must, therefore, be bounded by partial dislocations. While the stacking faults were not analysed thoroughly, contrast in images obtained under several diffraction conditions were consistent with

earlier work where a displacement vector of 1/4 $[011]_c$ was found in $La_{0.5}Sr_{0.5}CoO_3$ (cubic) grown from the vapour phase [8]. The boundary crossing the grain in Fig. 4(b) is probably an anti-phase boundary, for which the most obvious displacement vector to be proposed is 1/2 $[111]_c$, but again no detailed analysis of the contrast was carried out. The density of perfect lattice dislocations in the materials was very low and only a few isolated examples of dislocations were observed.

3.2. Samples with "ill-behaved" microstructures-prepared few weeks after sintering

All the TEM foils prepared within about one month of sintering showed qualitatively similar thinning behaviour and microstructure. After perforation, the thin region for each material condition showed evidence of considerable residual strain. The thin central part of the sample deformed, was no longer parallel to the original plane of the sample and tended to crack. TEM analysis was made difficult by the fact that materials were found to be quite friable, small cracks were present and electron transparent grains were easily lost from the foil. The defect density of each material was found to be extremely high, Fig. 5. Diffraction patterns from all three compositions showed a superlattice structure. In the pattern of Fig. 5 the weaker superlattice reflections correspond to a tripling of the $(200)_c$ and $(020)_c$ pseudo-cube spacing of the rhombohedral structure. The pattern corresponds to the presence of two sets of domains, within the area defined by the selected area aperture, superlattice reflections being present along the two directions separately. The bright-field/dark-field image pair of Fig. 6 shows planar defects lying within twin domains in a single grain. The high planar-defect density produced streaking of reciprocal points and deliberate alignment of the foil to chosen diffraction conditions was difficult.

found in
boundary
, for which
, but again
of perfect
w isolated

weeks after

ng showed
ure. After
evidence of
deformed,
ed to crack.
found to be
grains were
found to be
mpositions
the weaker
and $(020)_c$
corresponds
ned by the
ong the two
ig. 6 shows
high planar-
l deliberate
t.

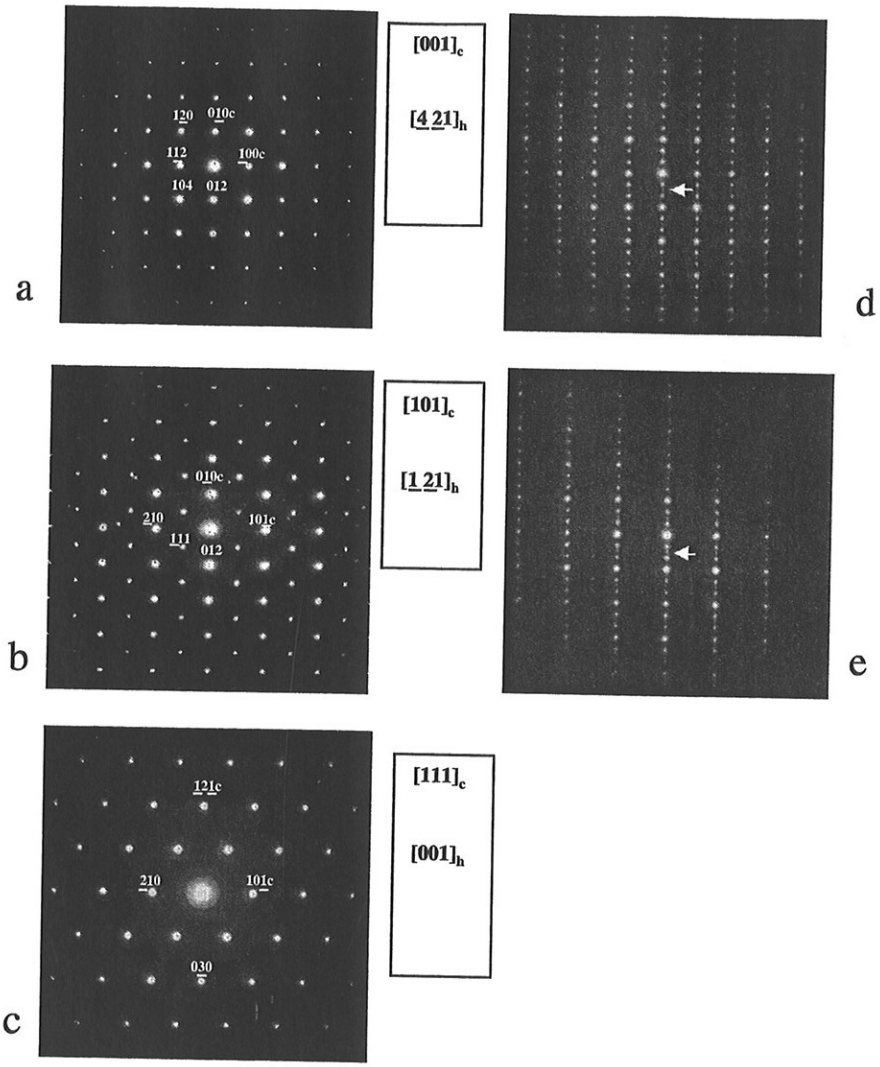

Fig. 7: SAD patterns from material with "well-behaved" microstructures (a-c) and "ill-behaved" microstructures (d-e). (d-e) show superpositions of patterns corresponding to a tripling of the cell along $[010]_c$ or [0 1 2] (strong superstructure reflections) and a doubling along $[010]_c$ or [0 1 2] (weak, arrowed reflections).

Figure 7 shows diffraction patterns obtained from major zone axes in non-substituted $LaCoO_3$, in both the "well-behaved" and "ill-behaved" states. In the "well-behaved" state (Figs. 7(a-c)) all $<100>_c$ and all $<110>_c$ zone axes are symmetrically equivalent, while $[111]_c$ is the 3-fold axis and other $<111>_c$ zones axes are not equivalent to it. Diffraction patterns are indexed both in pseudo cubic and hexagonal notations. In Fig. 7(b), we notice $\{\underline{1}11\}$ reflections that violate extinction rules for $R\bar{3}c$. In the depicted zone axis

the reflections can easily have arisen by double diffraction, e.g. {$\underline{1}$23} + {0$\underline{1}$2}. We have, however, also observed the {$\underline{1}$11} reflections under systematic-row conditions, under which they cannot be explained by double diffraction. The {$\underline{1}$23} reflections are a consequence of the rhombohedral distortion, and cannot be indexed (using integers) on the primitive cubic basis. The reflections disappear as the rhombohedral distortion approaches zero. The diffraction patterns from the ill-behaved material (Figs. 7(d-e)) show a superstructure along (0$\underline{1}$2) /$(010)_c$. The dominant superstructure periodicity is a tripling of the $(010)_c$ spacing. Weak reflections having a different periodicity, i.e. a doubling of the (010) spacing, are also superimposed in the pattern. The superposition of a strong tripling superstructure and a weak doubling superstructure is a common situation encountered in the "ill-behaved" materials. The angle between the (100) and (010) g-vectors in Fig. 7(d) is very close to 90° (equal within a measurement accuracy of ± 0.1°), showing that the rhombohedral distortion is much reduced in the ill-behaved materials with superstructures (the corresponding angle in Fig. 7(a) is 89.3°). The presence in Fig. 7(e) of a systematic row of weak reflections along [012] (including {$\underline{1}$23}), suggests that there is still a slight rhombohedral distortion in the structure with the superlattice reflections.

In one of the Sr-doped material foils, it proved possible to remove the high general defect density and the superlattice reflections by focussing the electron beam onto a single grain for several minutes. In the image of Fig. 8(a), the contrast of most of the grain shows a uniform density of defects with approximately planar alignment and such a high density that individual faults are difficult to distinguish individually. Figure 8(b) shows the [011] diffraction pattern recorded from the central part of the grain. Figure 8(c) shows the same grain after exposure to an intense electron beam. The orientation of the foil is the same as that of Fig. 8(a). Here, the complicated defect contrast of Fig. 8a has been replaced by mostly defect free clean single-domain contrast. The contrast that is present is mostly due to bend contours arising from bending of the foil due to low levels of strain. Several irregular planar faults with curved interfaces are visible. These were not analysed in detail but probably correspond to antiphase boundaries between regions where defect-free islands nucleated independently during annealing. The superlattice reflections have disappeared from the diffraction pattern, Fig. 8(d), leaving a regular [001] diffraction pattern. The grain of Fig. 8 did not have continuous contact with the rest of the sample and would probably have been heated significantly by the electron beam. Other grains, in better thermal contact with the bulk of the sample, retained the defect structure under a focused beam and probably did not reach such a high temperature.

This suggests that the change in the microstructure is due to localised heating of the sample rather than radiation damage.

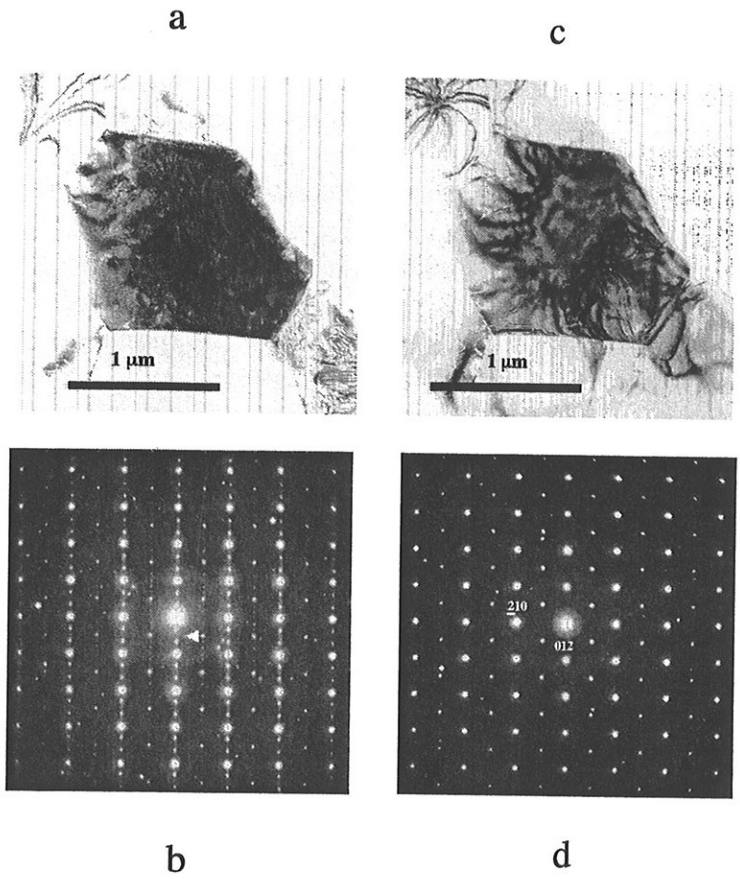

Fig. 8: Material before (a,b) and after (c,d) beam heating experiment. (a) The bright-field image shows high density of defects before heating. (b) The corresponding SAD shows superstructure reflections (arrowed). (c) The bright-field image taken after beam heating shows that the high defect density has disappeared. No twin domains are present, but there is weak contrast from curved anti-phase like boundaries. (d) In the corresponding SAD pattern, superstructure reflections have disappeared

There was one exception from the rule that "ill-behaved" microstructures were always found in samples from the first preparation campaign, and "well-behaved" microstructures in samples from the second campaign. Superlattice reflections were observed in diffraction patterns obtained from a single thin foil prepared from the very edge of the outer surface of an unannealed pellet of $LaCoO_3$, Fig. 9. The pellet was cracked by rough handling during the first sample preparation campaign, i.e. less than 1 month

after sintering. The foil was prepared from a small, irregular, fragment (~2.5 mm x 2 mm) of material that remained after the sample slice was cut. The thin part of the foil was very close to the original crack and plastic deformation, due to stress relief, could easily have occurred in this part of the sample around the same time that thin foils showing a superlattice were prepared. An important feature evident in Fig. 9 is that, while the superlattice defect structure is present in most of the grain, some parts of the same grain are defect-free single crystal. Some twin domains can also be seen. The spherical feature at the centre of the field is either an inclusion of impurity or a region of misoriented cobaltite. The inclusion appears to have acted as a focus for strain in the material and the pattern of the deformation structure is centred upon it.

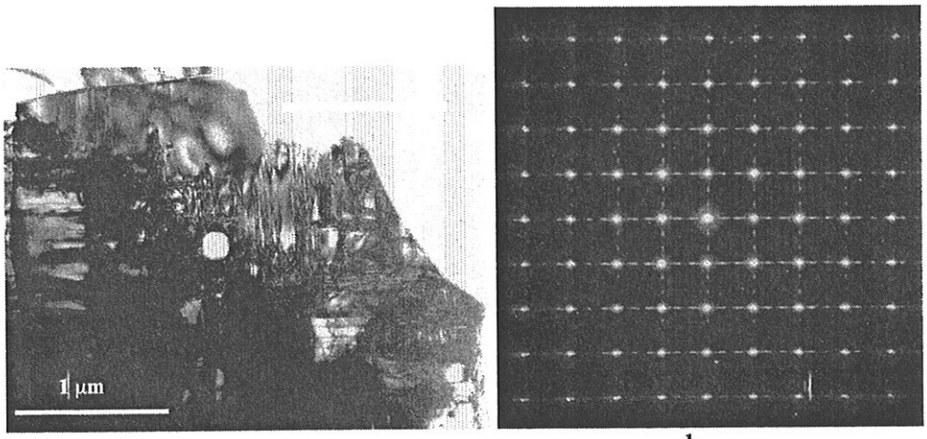

Fig. 9: Grain in pre-cracked material prepared after > 5 months. (a) Bright-field image showing defect-free regions within grain, as well as regions with high defect density. (b) Corresponding SAD pattern from two superimposed sets of domains showing tripling superstructure along both $<200>_c$ directions.

As a result of the observation of a high defect density in the material, one of the pellets of $LaCoO_3$ was annealed, Table I, and then prepared for TEM with a fairly large perforation. One foil of $LaCoO_3$ was further ion-thinned to enlarge the original perforation, to expose material where the sample showed less significant levels of macroscopic strain. In these foils, superlattice reflections were still present in diffraction patterns. The thin foils that originally showed the superlattice and deformation microstructure were re-examined at this stage (i.e. after five months) and were found to be

essentially unchanged. The high defect density was still present and superlattice reflections were still present in diffraction patterns recorded from these grains.

We investigated the possibility that compositional inhomogeneity in the material may be responsible for the contrasting observations made between samples prepared shortly after sintering, and five months later. The samples prepared after five months were taken from different postions in the pellets, close to the surface and far from the surface, including equivalent positions to the samples that showed residual stresses after the first sample preparation campaign. A total of 7 TEM samples were prepared during the second preparation campaign, and a total of 4 samples during the first campaign. None of the foils prepared from the latter campaign showed residual stress during thinning and no deformation superlattice reflections were present in diffraction patterns. The microstructure in all foils from the second preparation campaign was similar, i.e the defect content was low and the microstructure was dominated by {001} twinning.

4. Discussion

It appears that the microstructure of these materials is dominated by the influence of spontaneous strain introduced possibly by the cubic to rhombohedral phase transition, and certainly by thermal stresses arising upon cooling through the rhombohedral phase region (rhombohedral distortion and anisotropy increase with deceasing temperature).

Within weeks of sintering, long-scale residual strain is released when the material is thinned. This produced cracked TEM foils with significant macroscopic deformation. A high defect density is observed in the material and a deformation superlattice is observed. Once the deformation microstructure is formed, it is stable with respect to time at room temperature. Beam heating experiments showed that the metastable defect structure can be annealed and that this involves nanometre scale reordering of the structure but no reorientation of the basic crystal structure. Because the superstructures were observed in the non-substituted material, they cannot be attributed to ordering of different cations on the A sites. The commonly observed superstructure consisted in a tripling of the $\{100\}_c$ periodicity. A different superstructure, with a doubling of the $\{100\}_c$ periodicity, could also be observed. And in some diffraction patterns, a superposition of these situations could be observed. Close inspection of the diffraction patterns (e.g. Figs. 5, 7(a)) showed that the rotation of the axes due to the rhombohedral

distortion of the lattice is reduced by the presence of the tripling (or doubling) superlattice. Care must be taken in making such measurements from highly faulted crystals because the intersection of the Ewald sphere with streaked reciprocal lattice points can change the position of reflections in the diffraction pattern. However, examination of several $<100>_c$ diffraction patterns seems consistent with the conclusions drawn from examination of Figs. 5 and 7.

Samples prepared 5 months or more after the pellets were fabricated did not generally show the behaviour described above. The thinned region of the sample remained flat, suggesting no residual strain remained in the material. No superlattice reflections were generally observed in diffraction patterns. For undeformed material, the main defects observed in the grains are {100} twin domains. These twins reflect the reduction of symmetry during the cubic to rhombohedral phase transition during cooling, and provide a response in the material to spontaneous strain. Such strain can be produced by the change of shape of the unit cell in the phase transition [14]. It can also be produced by thermal stresses upon cooling through the rhombohedral phase region, owing to the anisotropic coefficient of thermal expansion of the rhombohedral phase. The geometry of the small number of stacking faults that we observed is consistent with the pseudo cube plane being the habit plane for defects in the rhombohedral perovskite structure. The density of perfect lattice dislocations is very low. Comparison of samples from symmetrically equivalent positions from either end of the original $LaCoO_3$ pellet, at different times, suggests that the variations observed in microstructure do not depend on variations in composition through the pellet.

The residual strain, high defect density and superlattice observations reported were unexpected. Wang and Zhang [7,8] reported a superlattice in cubic $La_{0.5}Sr_{0.5}CoO_3$ which produced a doubling of the periodicity in the {200} planes. However, this was attributed to ordering of La and Sr cations in tetragonal domains with sizes of 30-200 nm. The superlattice observed here appears to be due to periodically spaced faults rather than being related to composition modulations. The most widely observed superlattice structure appears to be associated with periodic faults that combine to produce a defect structure that gives a tetragonal distortion of the rhombohedral structure of the material. The overall periodicity is three times that of the "ideal" perovskite cell and may be produced by repeating three distinct short displacement vectors in the faults. High resolution TEM imaging would be needed to provide more detail about the displacement vector associated with the faulting that produces the superlattice structures.

For some phase transformations, structural relaxation can be slow. Salje [14] discusses the example of the C/2m-C1 phase transition in Na-feldspar, where the Al, Si ordering component of the phase transition may not be observable on a laboratory time-scale below a temperature of 700 K. For the materials considered here, it seems important to consider the microscopic details of the cubic-to-rhombohedral phase transformation and the accommodation of the variation in rhombohedral angle below the transition temperature. A full discussion of these issues is beyond the scope of this paper. It is worth emphasizing, however, that the observed microstructures are very similar for all compositions, even though the structural transition occurs at different temperatures for the different compositions. Our observations furthermore suggest that the kinetics of thermal-strain accomodation proceed on a laboratory timescale, i.e. within months.

Up to the present time, no heating stage experiments have been performed. It would be useful to measure the temperature at which the defect structure was annealed from the specimens and observe the transformation in a more controlled manner than that achieved in the beam heating experiment described above. The high level of residual strain and associated deformation in thinned foils suggests that the bulk microstructure in the metastable transitional state is not accessible directly by the TEM. The thin foils are clearly modified by deformation during thinning. It would be desirable to use a non-destructive method for characterising the microstructure that is sensitive to defects present in the bulk material. The standard XRD measurements obtained from our materials were consistent with the expected single-phase rhombohedral perovskite structure. More detailed diffractometry, x-ray precession, or synchrotron XRD experiments may be sensitive to the presence of structural defects or domain structures in the rhombohedal matrix. The cooling rate for our samples was quite rapid on the scale over which subsequent changes appear to have taken place. Examination of similar material with differing post-sintering cooling rated might be considered.

It is interesting to relate our microstructural observations to recent observations of ferroelastic behaviour in Ca-substituted $LaCoO_3$, as witnessed by mechanical hysteresis and characteristic change in XRD patterns after surface machining [11]. The generally suggested micromechanism of ferroelastic behaviour is that of domain switching upon applied stress that exceeds the material's coercive stress [13]. The rhombohedral distortion can be regarded as a compressive strain along one of the $<111>_c$ axes. There are four different variants of this distortion, one for each of the cubic <111> directions. The obvious domain-switching

mechanism is between the different variants of rhombohedral distortion. Such a mechanism would involve a re-bending of Co-O-Co bonds and a rotation of octahedra and would result in a stretching of the originally compressed <111> direction and a compression of one of the previously stretched <11$\underline{1}$> directions. The domains observed by TEM (e.g. Fig. 3) can be considered as orientation variants corresponding to compression along different $<111>_c$ axes. It appears that the domain switching proposed as an underlying mechanism for the observed mechanical hysteresis [11], is not simply that of switching domains like the ones seen in Fig. 3 into the orientation of their neighbours. XRD after surface machining exhibits a significant line broadening, which doesn't disappear upon annealing, and which is indicative of a decrease in domain size. It is yet unclear whether or how the introduction of a fine domain structure upon mechanical loading is related to our observed heavily deformed microstructures.

Understanding the differences in behaviour and defect content of different TEM foils may also be relevant to industrial applications. Applications of these materials, as described in the introduction, for permeable membranes or as cathode materials, require stable physical and mechanical properties. For example, the development of cracks in a thin permeable membrane during use would be unacceptable. Particular attention should be given to applications where the materials are thermally cycled, either within the rhombohedral phase region or through the rhombohedral-to-cubic transition temperature. An understanding of the microstructural mechanisms of accomodation of spontaneous strain under such conditions will be important.

5. Conclusions

TEM observations from $LaCoO_3$, $La_{0.8}Sr_{0.2}CoO_3$, and $La_{0.8}Ca_{0.2}CoO_3$ revealed microstructures that were strongly influenced by the time of thin foil preparation. Thin foils prepared within the first weeks of sintering showed macroscopic strain and a very high defect density, which included fault-related superlattice structures. Samples prepared several months after sintering, showed no significant macroscopic strain and the main defect was found to be domain boundaries due to reflection twinning in the pseudo-cube plane. The observations revealed no obvious composition-related microstructural differences.

The pattern of behaviour is likely to be related to accomodation of spontaneous strain arising upon cooling of the material from the sintering temperature. The observations suggest that part of the local ordering associated with accomodation of strain takes place on a laboratory timescale of months. The presence of twin domains illustrate clearly the lowering of lattice symmetry as compared to the ideal cubic perovskite structure, and is relevant for explaining recent observations of ferroelastic behaviour of these materials.

Acknowledgement

The work described in this paper was funded by the Norwegian Research Council.

References

1. R.CACIUFFO, D.RINALDI, G.BARACCA, J.MIRA, J.RIVAS, M.A.SENARIS-RODRIGUEZ, P.G. RADAELLI, P.G.FIORANI, and J.B.GOODENOUGH, *Phys. Rev. B*, **59** (1999) 1068.
2. J.A.M.VAN ROOSMALEN and E.H.P.CORDFUNKE, *J. Sol. State Chem.*, (1991) 212.
3. J.MIZUSAKI, Y.MIMA, Y.SHIGERU, F.KAZUO, and T.HIROAKI, *J. Sol. State Chem.* **80** (1989) 102.
4. A.MINESHIGE, M.INABU, T.YAO, O.ZEMPACHI, K.KIKUCHI, and K.MASAYA, *J. Sol. State Chem.* **121** (1996) 423.
5. Y.TERAOKA, K.NOBUNAGA, N.MIURA, and N.YAMAZOE, *Solid State Ionics* **48** (1991) 207.
6. H.TAGUCHI, M.SHIMADA, and M.KIOZUMI, *J. Sol. State Chem.*
7. **44** (1982) 254.
8. Z.L.WANG and J.ZHANG, *Phys.Rev. B* **54** (1996) 1153.
9. Z.L.WANG and J.ZHANG, *Phil. Mag. A* **72** (1995) 1513.
10. B.GILBU, H.FJELLVÅG, and A.KJEKSHUS, *Acta Chem. Scand.* **48** (1994) 37.
11. T.GRANDE et al. (1999), to be published.
12. N.ORLOVSKAYA, M.-A.EINARSRUD, T.GRANDE, J.C.WALMSLEY, Y.GOGOTSI, and G.GOGOTSI, submitted to *Phys. Rev. B*.
13. K.KLEVELAND, M.-A.EINARSRUD, and T.GRANDE, *J. Eur. Ceram. Soc.* (1999), in print.
14. E.H.K.SALJE, "Phase transitions in ferroelastic and co-elastic crystals"(Cambridge Univ. Press. Cambridge, 1990).